

Aus dem
Alfred-Wegener-Institut für Polar- und Meeresforschung
Bremerhaven

Modeling Physical and Biological Processes in Antarctic Sea Ice

Dissertation
zur Erlangung des Grades eines
Doktors der Naturwissenschaften
– *Dr. rer. nat.* –

dem Fachbereich Biologie/Chemie der
Universität Bremen
vorgelegt von

André Luiz Belém

February 2002

1. Gutachter: Prof. Dr. Dieter Wolf-Gladrow
2. Gutachter: Prof. Dr. Ulrich V. Bathmann

Tag des Promotionskolloquiums: 28.02.2002

Acknowledgments

The research and the mathematical model developed in this dissertation were conducted at the Alfred-Wegener-Institute for Polar and Marine Research in Bremerhaven, Germany, with financial support from the Brazilian Scientific Council - CNPq (Conselho Nacional de Desenvolvimento Científico e Tecnológico) under the research grant 290078/1997-0, and supervised by Prof. Dr. Dieter Wolf-Gladrow, professor in theoretical marine ecology at the University of Bremen. I am most grateful to Dieter for his attention especially at the end of this work, which gave me the necessary motivation to finish my thesis. I also want to thank Prof. Dr. Ulrich Bathmann for the review of the final version of my dissertation.

I also wish to thank Dr. Gerhard Dieckmann and Dr. Hartmut Hellmer for the necessary support at the AWI. Gerhard gave me not only access to his sea ice dataset, but also offered me his office, books, computers, *passwords*, and most importantly - his friendship.

A special thanks goes to Dr. Ralph Timmermann, who provided the sea ice velocity fields and the oceanic heat flux climatological data from the BRIOS-2 model used in the coupled biological-physical sea ice model. To Dr. Christoph Völker, thanks for the helpful discussions over numerical analysis and linear dynamic systems that I used to develop the biological model. Thanks to Dr. Inga Hense and Thomas Mock for the constructive discussions and comments over the main aspects of the primary production in the Southern Ocean and sea ice. I also thank Dr. Hajo Eicken and Dr. Richard Zeebe for the interesting ideas on sea ice thermodynamics. Their sea ice model was a great help in the beginning of this work. For the review of the English manuscript I wish to thank Robin Brinkmeyer.

I would also like to thank my friends for believing me and in my work. *Vielen Dank* to Andreas, Andre Wischmeyer, Beni, Bjorn, Carmen, Coco, David Thomas, Erika, Ingrid, Irini, Mauricio, Dani, Nadia, Nicole, Rainer, Sabine, Sandra, Ulf, Uta Passow, Chris Cogan and Uta Schneider. Thanks also to my family in Brazil, especially my mother, who gave me courage during the storming moments. Many, many, many thanks to Linda Rosa da Silva Mendes and Raquel Carneiro, from the Brazilian Scientific Council, who guided me and my wife through the complicated ways of the governmental bureaucracy.

And the most important person in my life, Adriene... You are the lighthouse in the storm, showing me the safest way to tread. I love you.

Abstract

The Southern Ocean (ca. 20% of the world ocean surface) and its ice covered area play a significant role in global climate regulation, representing *a priori* a potential sink area for atmospheric CO₂. During the winter, the sea ice cover acts as a barrier and its presence has an enormous effect on the exchange of heat, moisture and momentum between ocean and atmosphere. From a biological point of view, sea ice with its network of brine channels is a rich habitat for microbial communities and a variety of small organisms, and therefore of vital importance for the whole Antarctic ecosystem.

In this work, a coupled biological-physical sea ice model was developed to investigate the influence of transient changes in environmental conditions (e.g. light, temperature and nutrient dynamics) on the sea ice biological communities. To simulate this complex environment, the biological model uses self-adapting physiological schemes and variable cellular N:C and Si:C quotas, including co-limitation, to decouple biomass accumulation and inorganic nutrient availability. Forcing terms (ice temperature, brine salinity, light and nutrients) are controlled by the thermodynamic sea ice model, with emphasis on the light and heat conduction through the sea ice and desalination processes (flux of brine). The model indicates that thermodynamic processes controlling ice formation and growth play a key role in the establishment and vertical distribution of biological sea ice communities. The coupled biological-physical model is described in a Lagrangian manner, where the time-dependent position of simulated ice floes extracted from ice velocity fields are used to compute forcing parameters (e.g. air temperature, oceanic heat flux, solar radiation).

A good agreement between model results and field observations was found, indicating that the model well represents the physical and biological processes in sea ice. The model was also used to estimate the total productivity of sea ice in the Weddell Sea, resulting in an annual carbon production of ≈ 11 Tg C with a strong seasonal variability. The most productive months are between December and February, when light and temperature conditions in the sea ice are considerably enhanced as compared to the other months. Between May and September, the sea ice productivity ranges from 0.16 to 0.6 Tg C month⁻¹ contributing 17% to the total annual production. This production has an important role in the sea ice ecosystem, particularly for the overwintering organisms associated with the pack-ice, such as the Antarctic krill *Euphasia superba*. The exercise of modeling physical and biological processes in sea ice presented in this work provides an improvement of our understanding of the Antarctic sea ice ecosystem.

Zusammenfassung

Der Südliche Ozean mit ca. 20% der Gesamtfläche des Weltozeans und das ihn bedeckende Meereis spielen eine wichtige Rolle bei der Regulierung des globalen Klimas und stellen a priori eine mögliche Senke für das atmosphärische CO₂ dar. Während der Wintermonate agiert das Meereis als eine Barriere zwischen Atmosphäre und Ozean, mit einem erheblichen Einfluss auf den Austausch von Wärme, Feuchte und Impuls. Aus Sicht der Biologie ist das Meereis ein reicher Lebensraum für mikrobielle Gemeinschaften und eine Vielzahl kleiner Organismen, die in den Salzkanälen leben und von großer Bedeutung für das gesamte antarktische Ökosystem sind.

Als Teil dieser Arbeit wurde ein gekoppeltes biologisch-physikalisches Meereismodell entwickelt, um den Einfluss sich verändernder Umweltparameter, wie Licht, Temperatur und Nährstoffe, auf die biologischen Meereisgemeinschaften zu untersuchen. Zur Simulation dieses komplexen Systems beinhaltet das biologische Modell ein selbst-adaptierendes physiologisches Schema mit variablen Nährstoffverhältnissen, N:C und Si:C, und einer gleichzeitigen Limitierung, um die Akkumulation von Biomasse und die Verfügbarkeit von anorganischen Nährstoffen zu trennen. Die Antriebsterme (Temperatur des Eises, Salzgehalt der Lauge, Licht und Nährstoffe) werden durch das thermodynamische Meereismodell bestimmt, unter besonderer Berücksichtigung der Licht- und Wärmeleitung durch das Eis und dessen Entsalzen. Das Modell zeigt, dass die thermodynamischen Prozesse, die Eisbildung und Wachstum kontrollieren, eine Schlüsselrolle bei der Entstehung und der vertikalen Verteilung biologischer Meereisgemeinschaften haben. Das gekoppelte biologisch-physikalische Meereismodell wird im Lagrangian Raum betrachtet, indem die zeitabhängige Position simulierter Eisschollen benutzt wird, um die Antriebsterme (z.B. Lufttemperatur, ozeanischer Wärmestrom und solare Einstrahlung) zu bestimmen.

Die erzielten Modellergebnisse ergaben eine gute Übereinstimmung mit den Feldbeobachtungen. Dies bedeutet, dass die physikalischen und biologischen Prozesse im Meereis durch das Modell gut wiedergegeben werden. Das Modell wurde ebenfalls dazu genutzt, für das Weddellmeer die gesamte Produktivität des Meereises abzuschätzen. Letztere beträgt ≈ 11 Tg C pro Jahr mit einer starken saisonalen Variabilität. Die produktivsten Monate sind zwischen Dezember und Februar, wenn Licht- und Temperaturverhältnisse im Meereis im Vergleich zu den anderen Monaten optimaler sind. Von Mai bis September variiert die Meereisproduktivität zwischen 0.16 und 0.6 Tg C pro Monat und trägt somit 17% zur gesamten Jahresproduktion bei. Diese Produktion ist von erheblicher Bedeutung für das Ökosystem des Meereises, speziell für die im Packeis überwinterten Organismen (z.B. der antarktische Krill *Euphasia superba*).

Die Modellierung physikalischer und biologischer Prozesse im Meereis, wie in dieser Arbeit dargestellt, half, unser Verständnis bezüglich des antarktischen Meereis-Ökosystems zu verbessern.

Contents

Acknowledgments	i
Abstract	iii
Zusammenfassung	v
Contents	vii
List of Figures	ix
List of Tables	xiii
1 Introduction	1
1.1 Physical and Biological Significance of the Sea Ice	2
1.1.1 Geographical Provinces in the Antarctic Pack Ice	3
1.1.2 Development of Biological Communities in the Sea Ice	6
1.1.3 Sea Ice Formation and Growth	8
1.2 Primary Production Estimates of Antarctic Sea Ice	10
1.2.1 Modeling Antarctic Sea Ice Biology	12
1.3 Motivation and Objectives	13
2 The Biological Sea Ice Model	17
2.1 Basic Concepts	18
2.2 Model Description	19
2.2.1 Primary Production	22
2.2.2 Regulation of Chlorophyll-to-Carbon Ratio	24
2.2.3 Nutrient Dynamics	27
2.2.4 Grazing	29
2.2.5 Nitrogen Recycling	31
2.3 Model Validation	32
2.4 Time Scales near the Model Stationary State	39
3 Modeling the Spectral Solar Radiation within Sea Ice	43
3.1 The Incoming Solar Radiation	43
3.1.1 The Direct Component of Solar Radiation	45
3.1.2 The Diffuse Component of Solar Radiation	47
3.2 The Bio-optical Sea Ice Model	49
3.2.1 Brine Pockets	52
3.2.2 Air Bubbles	53
3.3 Light Attenuation within the Sea Ice	54

3.4	Seasonal Variations in the Photosynthetically Available Radiation over the Sea Ice	56
4	The Thermodynamic Sea Ice Model	61
4.1	Modeling Sea Ice Thermodynamics	62
4.1.1	Heat Fluxes at the Atmosphere-Ice Interface	63
4.1.2	Heat Conduction in Snow and Sea Ice Layers	65
4.1.3	Freezing and Melting at the Ice-Ocean Interface	68
4.2	Fluxes of Brine, Salt, Nutrients and Biological Material	69
4.2.1	Nutrient Dynamics in Sea Ice	71
4.2.2	Incorporation and Accumulation of Biological Communities in Sea Ice	72
4.2.3	Vertical Reallocation of Biological Material	74
4.3	Model Time Step	77
5	Coupling Physical and Biological Processes in Sea Ice	79
5.1	Simulating Sea Ice Lagrangian Drifters	81
5.2	Individual Analysis of Simulated Ice Cores	84
5.2.1	Productivity and Nutrient Dynamics	92
6	Estimates of the Sea Ice Primary Production for the Weddell Sea	99
6.1	The Distribution Sea Ice Properties at Regional Scales	99
6.1.1	Sea Ice Algal Standing Crop in the Weddell Sea	100
6.2	Estimates of the Sea Ice Biological Production	105
7	Conclusions and Outlook	109
A	Model Forcing Fields and Parameterization	113

List of Figures

1.1	Sea ice sectors in the Southern Ocean	4
1.2	Seasonal variations of the Antarctic sea ice extent	5
1.3	Seasonal Antarctic sea ice extent	6
1.4	Schematic biological cycle in the pack-ice	7
1.5	Vertical heterogeneity in the ice internal structure	9
1.6	Comparison between physical and biological scales in sea ice	14
2.1	Schematic representation of the sea ice biological model	19
2.2	Temperature-dependent maximum photosynthetic rate for sea ice microalgae	24
2.3	Changes in the Chl- <i>a</i> :C ratio due to irradiance shifts	26
2.4	Nitrogen controlling of metabolic processes (γ and A_{lim})	28
2.5	C-specific ingestion rates for sea ice heterotrophic protists	31
2.6	Model results compared with experimental data: Microalgal carbon, Chl- <i>a</i> and nutrient dynamics	35
2.7	Model results compared with experimental data: Microalgal N:C and Si:C quotas, Chl- <i>a</i> :C and Chl- <i>a</i> :N	36
2.8	Model results with grazing: Microalgal and heterotrophic protists carbon biomass, Chl- <i>a</i> and nutrient dynamics	37
2.9	Model results with grazing: Microalgal N:C and Si:C quotas, Chl- <i>a</i> :C and Chl- <i>a</i> :N ratios, protozoa N:C quota	38
2.10	Time constant under cellular nitrogen limitation	41
2.11	Time constant under cellular silicon limitation	42
3.1	Schematic representation of light transmission through the atmosphere and sea ice	44
3.2	Solar spectrum and atmospherical attenuation coefficients between 300 and 700 nm	47
3.3	Spectral albedo of sea ice	49
3.4	Absorption coefficients for pure ice, brine, and chlorophyll- <i>a</i>	53
3.5	Simulated vertical distribution of light in sea ice with a chl- <i>a</i> peak at the bottom-most layers	54
3.6	Simulated vertical distribution of light in sea ice with chl- <i>a</i> concentrated at the topmost layers	55
3.7	Monthly means of the maximum photosynthetically available radiation (PAR) at the snow/ice interface from May to October	57
3.8	Monthly means of the maximum photosynthetically available radiation (PAR) at the snow/ice interface from November to April	58
4.1	Schematic representation of heat fluxes in sea ice and model grid	63
4.2	Relationships between sea ice temperature, bulk salinity, brine salinity and brine volume	67

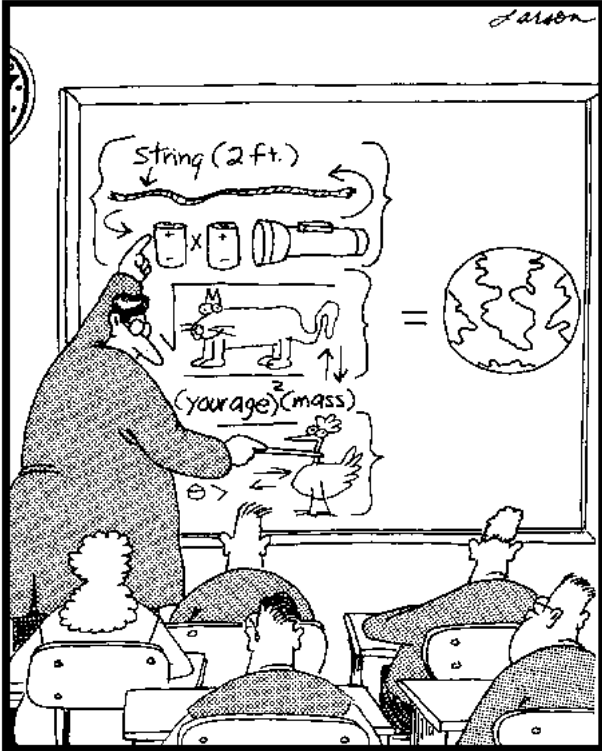
4.3	Changes in bulk salinity due to brine drainage and nutrient in brine as a function of brine volume and bulk nutrient concentration	71
4.4	Accumulation of chlorophyll- <i>a</i> in newly forming sea ice	73
4.5	Air temperature during a simulated run to show accumulation of biological material	76
4.6	Simulated time-dependent accumulation and redistribution of chlorophyll- <i>a</i> in sea ice	77
4.7	Schematic representation of model timestep and coupling	78
5.1	Variability in the air temperature observed for a drifting ice buoy (Lagrangian) compared with its initial position (Eulerian)	80
5.2	Simulated drift of WWGS92 ice floes	82
5.3	Time series of incoming solar radiation and air temperature for core #1 . . .	85
5.4	Observed and simulated sea ice profiles for core #1	85
5.5	Simulated time evolution of sea ice vertical temperature and salinity profiles for core #1	86
5.6	Simulated daily net production and integrated chlorophyll- <i>a</i> for core #1 . .	87
5.7	Observed and simulated sea ice profiles for core #3	87
5.8	Time series of air temperature and simulated vertical profile of ice temperatures for core #3	88
5.9	Observed and simulated sea ice profiles for core #4	89
5.10	Observed and simulated sea ice profiles for Core #6	90
5.11	Time series of air temperature and simulated vertical profile of ice temperatures for core #6	91
5.12	Simulated time evolution of sea ice vertical chlorophyll- <i>a</i> profile for core #6	92
5.13	Simulated daily net production and integrated chlorophyll- <i>a</i> for core #6 . .	92
5.14	Time series of incoming solar radiation and air temperature for core #8 . . .	93
5.15	Observed and simulated sea ice profiles for core #8	93
5.16	Simulated daily net production and integrated chlorophyll- <i>a</i> for core #8 . .	94
5.17	Distribution of Chlorophyll- <i>a</i> to carbon ratio for simulated ice cores	94
5.18	Simulated dissolved nutrients as a function of ice bulk salinity for simulated ice cores	95
5.19	Daily net primary production for simulated ice cores	96
5.20	Relationship between the biomass-specific primary production and solar light for simulated ice cores	96
6.1	Vertical integrated chl- <i>a</i> biomass versus ice thickness and day of year determined from ice cores in the Weddell Sea	101
6.2	Monthly mean integrated chl- <i>a</i> derived from ice cores and model results in the Weddell Sea	102
6.3	Seasonal frequency distribution of the vertical integrated chl- <i>a</i> biomass from simulated ice cores in the Weddell Sea	102
6.4	Monthly means of the Chl- <i>a</i> :C ratio for first-year ice in the Weddell Sea . .	103
6.5	Status of dissolved nutrient as a function of ice bulk salinity	104
6.6	Monthly means of net sea ice primary production from simulated ice floes .	105
7.1	The seasonal cycle of the Antarctic pack-ice	111

A.1	Seasonal variability of the absolute difference between observed and NCEP derived air temperatures	114
A.2	Aerosol climatologies used in the spectral solar model	115
A.3	Ozone climatology used in the spectral solar model	116

List of Tables

2.1	Prognostic variables in the biological sea ice model	20
2.2	Diagnostic variables in the biological sea ice model	21
2.3	Light-saturated C-specific photosynthetic rate of Antarctic phytoplankton and sea ice algae	25
2.4	Model parameters and initial conditions for model integration	33
4.1	Coefficients used for determining sea ice brine volume, bulk density and thermal conductivity	67
5.1	Simulated origin and final position of ice floes collected during the WWGS92	81
5.2	Summary of observed and simulated vertical profiles of WWGS92 ice cores	83
6.1	Sea ice extent and associated primary production in the Weddell Sea	106
A.1	Forcing variables used in the model	113
A.2	Links to the home pages of the datasets used in this work	117

The Far Side, by Gary Larson. Copyright ©2000 FarWorks, Inc.



Creationism Explained

Keep it simple; as simple as possible, but no simpler ...
– Albert Einstein (1879-1955) –

Chapter 1

Introduction

The sea was remarked to have assumed its oceanic light blue colour, from which we inferred that the ferruginous animalculae, which give a dirty brownish tint to the waters of the southern ocean, prefer the temperature which obtains in the vicinity of the pack; for here, as in the arctic regions, our approach to any great body of ice was invariably indicated by the change in colour of the sea (p. 214).

Ross, J. C. [1847]. *A Voyage of Discovery and Research in the Southern and Antarctic Regions during the Years 1839-43*. in 2 vols. John Murray, London.

Apart from being a constant danger for ships, sea ice has been an object of investigation of almost every expedition in the early stages of Antarctic exploration. However, its scientific importance was underestimated until the discoveries of the British Antarctic Expedition of 1839-43 on board the *HMS Erebus* and *Terror*. The expedition was headed by Sir James Clark Ross, a man with ability and aptitude for science, elected to the Linnean Society in 1823, and whose experience was acquired during fifteen summers and eight winters in the Arctic. The scientific work carried out during the 4 years long journey brought more knowledge about the Antarctic sea ice ecosystem than any other in the early stages of polar exploration. Discolored ice, frequently seen in the Antarctic pack-ice, was mistaken as contamination from volcanic ash. It was Joseph Hooker, the young naturalist on board the ship *Erebus*, who had the first insights on the importance of sea ice for the Antarctic ecosystem. Hooker's examination of melted ice samples revealed that the coloration was produced by diatoms and samples were sent to the German protozoologist C.G. Ehrenberg, who identified seven new genera and 71 new species. The recognition of the true ecological significance of sea ice microalgae was summarized by Hooker in 1847 on his book *Flora Antarctica*, which defines the basis for the Antarctic sea ice biology.

1.1 Physical and Biological Significance of the Sea Ice

The Southern Ocean represents 20% of the World Ocean surface and its ice covered area is a significant part of the enormous ocean heat-change engine, which enables our planet Earth to have temperatures suitable for life. The incoming solar radiation at equatorial latitudes is absorbed by the ocean and the energy is transported north and south towards the polar regions, where it is lost again to the atmosphere [Wadhams 2000]. The sea ice governs the rate of heat loss, depending on its extent, thickness and concentration, serving as a regulatory function vital to the climate of our planet.

The sea ice motion leads to water mass modification both in the region where ice is formed (fresh water is removed) and in the region where ice melts (fresh water is released to ocean). It also acts as a barrier affecting exchanges of gases, heat and momentum between the ocean and atmosphere. Although the oceanic area of the Southern Ocean could *a priori* represent a potential sink for atmospheric CO₂ and therefore contribute to a reduction of the *Greenhouse effect*, the influence of the sea ice cover in the global carbon cycle is still not completely understood [Tréguer 1994]. From a biological point of view, sea ice is a rich habitat for microbial communities and a variety of life forms being of vital importance for the whole Antarctic ecosystem [Spindler and Dieckmann 1994].

All these factors are the product of a habitat which itself experiences a strong seasonal cycle of growth and decay, constrained to around 2.5×10^6 km² in the summer (ca. 5% of the Southern Ocean area) while its area grows in the winter up to 20×10^6 km². The direct consequence of this dynamic feature is that many organisms, which depend on the sea ice in one way or another, are constantly confronted with the expansion and retreat of the ice cover. For those microorganisms living within the sea ice, the seasonal cycle means new surfaces for colonization during the ice growth and a rapid destruction of the habitat during the ice retreat. The sea ice seasonal dynamics are therefore subject to inter-annual oscillations which undoubtedly affect the associated biological communities. The main interest in understanding the role of biological and physical processes in the sea ice resides in the uncertainty about the impact of global climate changes in the Antarctic ecosystem.

1.1.1 Geographical Provinces in the Antarctic Pack Ice

The first estimate of the seasonal circumpolar limits of Antarctic sea ice was given by Mackintosh and Herdman [1940], based upon reports from whaling ships and oceanographic missions in the Southern Ocean. However, the inter-annual variability of the Antarctic sea ice cover was already a clear fact. Captain James Weddell, on board the brig *Jane*, sailed from the South Shetland Islands in 1823 to the furthest south position of $74^{\circ}15' \text{ S}$ (at longitude 34° W). The discovery of open water at this position was fortunate because of an unusually ice-free season, and the repetition of his route was not possible for nearly 90 years. Unfortunately, ship observations could give only a partial view of the Antarctic sea ice distribution, and later in the 1970s, with the advent of polar orbiting satellites, the complete seasonal and inter-annual Antarctic sea ice extent could be assessed.

The distribution of sea ice in the Southern Ocean is influenced by atmospheric and oceanic circulations, as well as by the surface air temperature. Based on the seasonal variations of sea ice extent around the Antarctic continent, Zwally *et al.* [1983] proposed a division of the Southern Ocean into five provinces: the Weddell Sea Sector, the Indian Sector, the Western Pacific Sector, the Ross Sea Sector and the Amundsen & Bellingshausen Seas Sector (Fig. 1.1).

The maximum sea ice extent occurs in September and October with small variations in the zonal position of the ice edge. Moving clockwise, the ice edge reaches 55° S in the Weddell Sea sector at about 15° E , but lies at about 60° S around most of the rest of East Antarctica (Indian Sector), reaching even further south to 65° in the Western Pacific Sector. In the Ross Sea Sector, the edge moves north again to 62° S , and shifts southward to 66° off the Amundsen & Bellingshausen Seas Sector before moving north in the Antarctic Peninsula completing its circumpolar extent.

The zonal position of the ice edge during its maximum extent has a significant zonal variation of around 11° . Zwally *et al.* [1983] showed that the winter advance of the ice limit is closely related to the -1.8° C isotherm in the surface air temperature (i.e. corresponding to the freezing point of seawater) and the southern boundary of the Antarctic Circumpolar Current (ACC). These factors suggest that the ice limit is mainly determined by thermodynamic processes, with small scale variations in the maximum extent related to deflections of the ACC. Another source of variability is the Antarctic Circumpolar Wave [White and Peterson 1996],

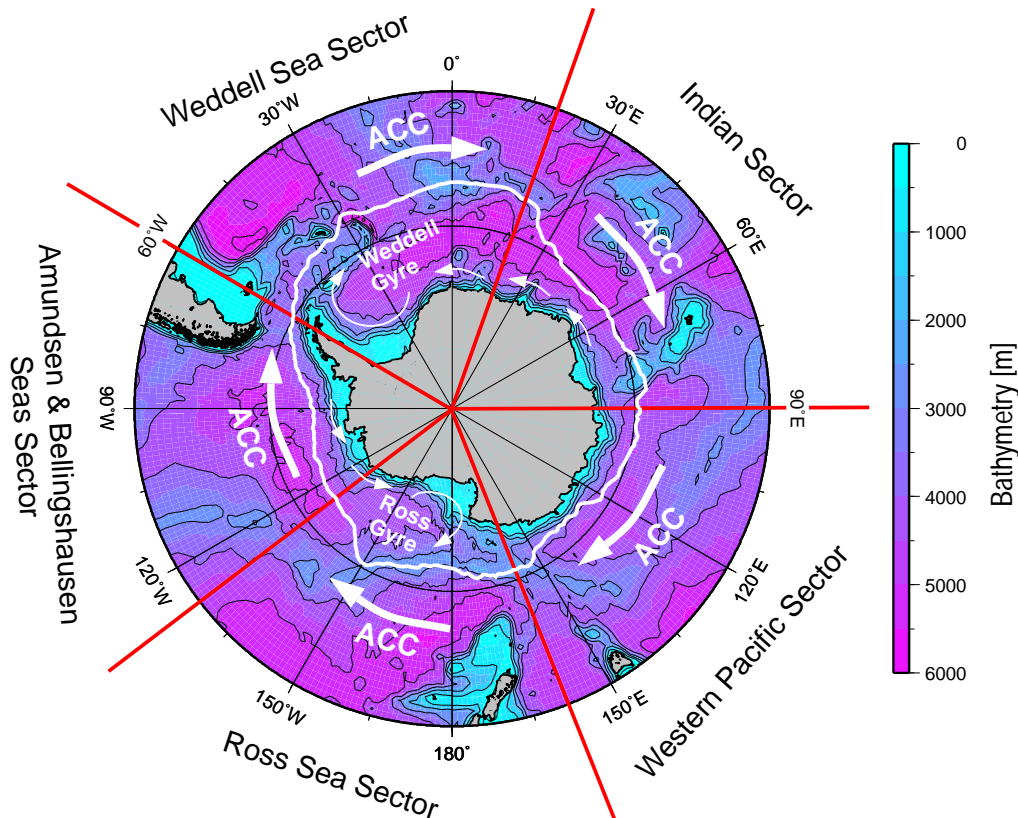


Figure 1.1: Sea ice sectors in the Southern Ocean following Zwally *et al.* [1983], where the white line shows the maximum sea ice extent based on 7-years of satellite observations between 1992 and 1998. The arrows represents the eastward flow of the Antarctic Circumpolar Current (ACC), the Weddell Gyre, the Ross Gyre and the westward flow of the Antarctic Coastal Current, as indicated.

a fluctuation with a period of 4 years in the surface pressure, temperature and winds that has been suspected to influence sea ice formation and distribution [Beckmann and Timmermann 2001]. The main driving forces of the Antarctic sea ice motion are the surface ocean circulation and the atmospheric winds. Apart from the strong eastward flowing ACC, delimiting the northern limits of sea ice, the ice drift patterns near the coast are governed by the westward flowing Antarctic Coastal Current driven mainly by east winds south of 66°S . In the Ross Sea and Weddell Sea, cyclonic gyres caused partially by barotropic and baroclinic effects, accompany the zonal barrier formed by the Antarctic continent, where the transport of ice is clockwise diverted out to the ice edge. Observations of ice drift buoys and model results in the Weddell Sea and the Ross Sea suggest that the gyres are not closed at their eastern ends, causing a positive net transport of ice northward and a change of drift direction from westward to eastward at the northern limits of the ice edge.

The months with a minimum sea ice extent are January and February, with multi-year ice

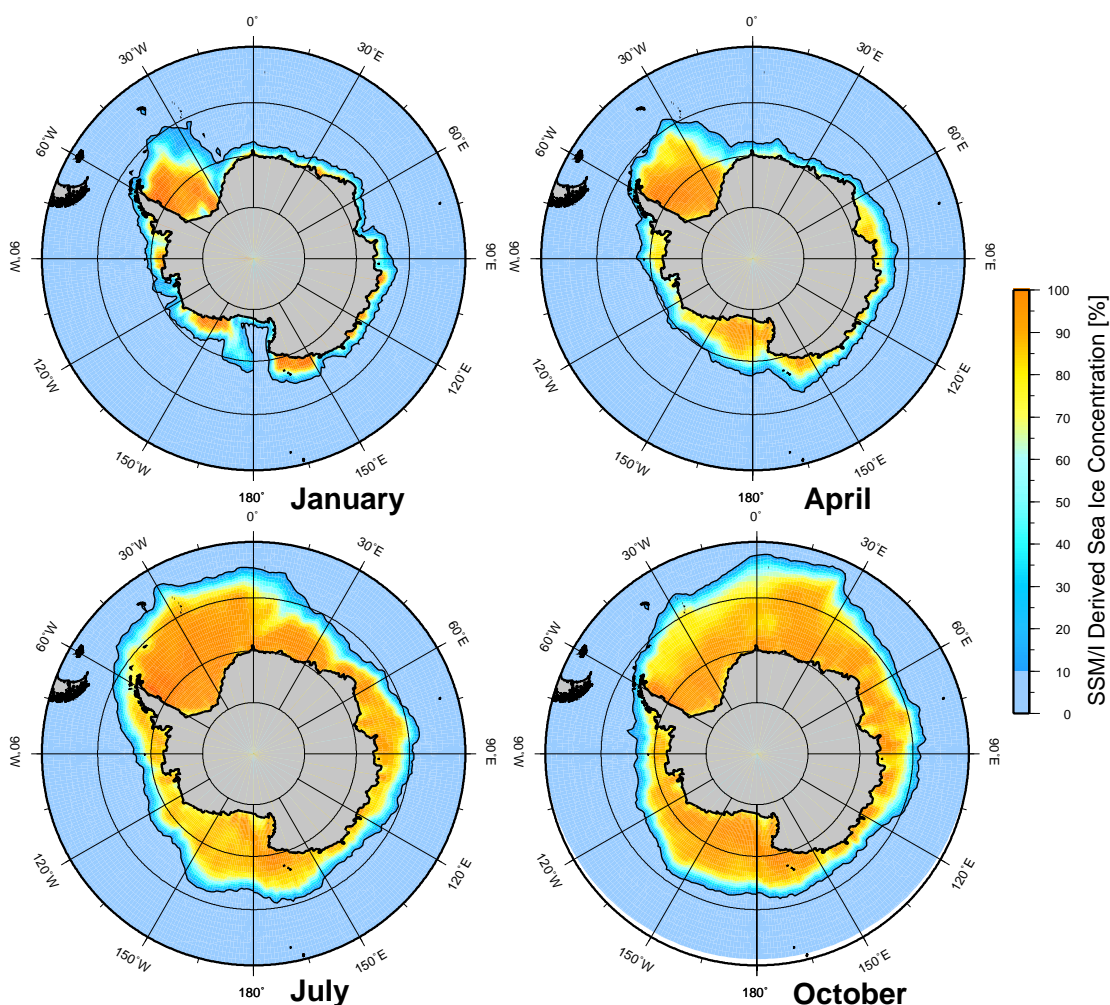


Figure 1.2: Seasonal variations of the Antarctic sea ice extent based on satellite observations between 1992 and 1998 from the DMSP-SSM/I Program (see Appendix A).

fields remaining in the Western Weddell Sea and some coastal areas in the Bellingshausen Sea and East Antarctica. By March, the short Antarctic summer is over and the ice advance begins covering first the central parts of the Weddell and Ross seas. In April, the circumpolar ice edge is already formed, and advances northward in the following months. Between July and August, the growing pack-ice area slows down reaching its maximum extent on later September-early October. Figure 1.2 shows the monthly means of Antarctic sea ice concentrations in four different seasons: summer (January), Autumn (April), Winter (July) and Spring (October). The ice edge retreats faster between October and January.

The complete annual cycle of Antarctic sea ice has a very high amplitude (Fig. 1.3) as compared with the Arctic showing small inter-annual oscillations. During a 7-year period of satellite observations, the minimum sea ice cover occurring in February-March ranged from

1.8 to 2.5×10^6 km², while the maximum extent in September-October showed values from 15.8 to 16.5×10^6 km². That leads to an areal growth rate of 65.000 km² per day during the advance of the sea ice between March and September, and a loss of around 92.000 km² per day during the ice retreat between October and February.

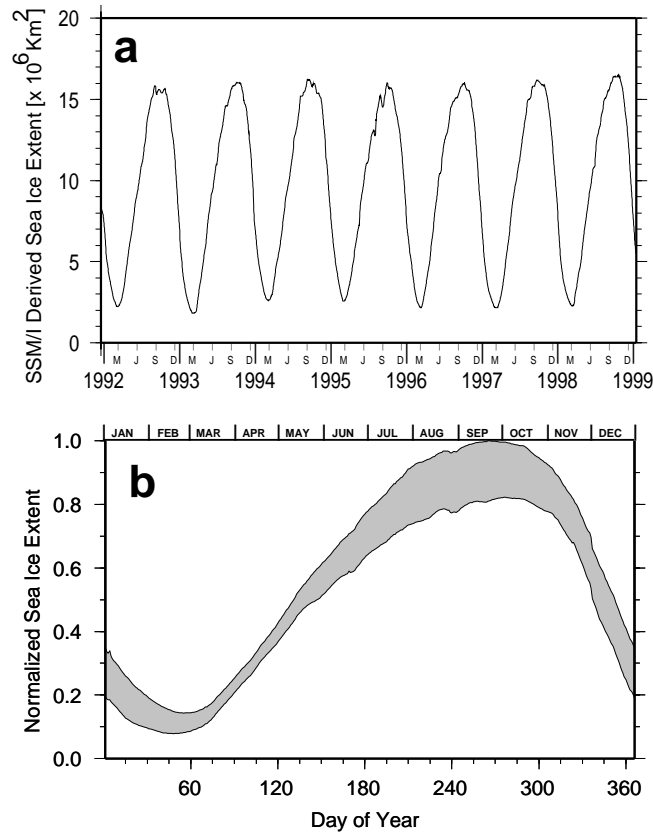


Figure 1.3: The inter-annual variation of the total sea ice extent (a) with months represented by letters (M=March, J=June, S=September, D=December) and the normalized seasonal extent of Antarctic sea ice (b). The shaded area represents the contribution of multi-year ice for the total sea ice area. Data from the DMSP-SSM/I Program (see Appendix A).

1.1.2 Development of Biological Communities in the Sea Ice

The sea ice seasonal cycle has two main implications for the associated biological communities: first, a fast growth in the habitat area available for colonization followed by a drastic ice retreat during the transition to summer; and second, the role of ice drift during the growth season in the transport of biomass through the seasonal ice zone. The link between biological communities and sea ice formation itself begins during direct interactions of ice crystals formed in seawater with individual organisms (viruses, bacteria, protists and metazoans), generating a net transport of the biota from the water column into sea ice with a variable size

classes distribution [Garrison *et al.* 1989, Weissenberger and Grossmann 1998]. During the ice growth season (autumn and winter), sea ice changes its properties responding to transient variations in the air temperatures and solar radiation. Modifications in the temperature and salinity profiles due to thermodynamic and desalination processes play an important role in the formation of specific microbial communities in the brine channels (as bottom, interior and surface communities). At the end of this seasonal cycle, the onset of sea ice melting is accompanied by high pelagic primary production due to increasing light intensities and water column stratification [Nelson *et al.* 1987, Mathot *et al.* 1991, Arrigo and McClain 1994, Mengesha *et al.* 1998]. Observations of biogenic material released from melting sea ice showed a rapid sedimentation pattern and high grazing pressure on aggregates [Riebesell *et al.* 1991]. This process demonstrate the importance of sea ice microalgae for the pelagic Antarctic food web and export of carbon to the deep ocean. The “seeding” effect may also contribute as an inoculum for pelagic production [Mathot *et al.* 1991, Riebesell *et al.* 1991].

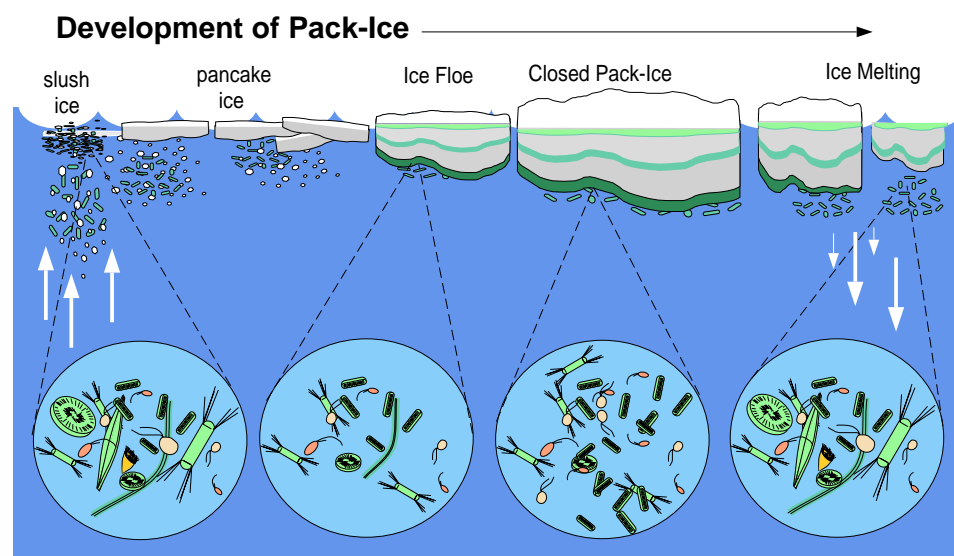


Figure 1.4: Schematic representation of the pack-ice development where sea ice formation and growth are coupled to the colonization of the ice by microbial communities (after Ackley and Sullivan [1994]). The description of ice types (slush, pancake and floe) is given in the next subsection.

Differences between the various sea ice communities during the ice formation are marked by distinct physical processes at each phase of the pack-ice development. Ackley and Sullivan [1994] proposed a scheme describing the physical control on the development and characterization of Antarctic sea ice microbial communities (Fig. 1.4), where sea ice microalgae are comprised of a smaller subset of the phytoplankton spending a major fraction of

their life cycles in association with ice. Differences in species composition between phytoplankton and microalgae in newly formed ice are not significant [Lizotte and Sullivan 1991], but for older ice floes with subsequent *in situ* microalgal growth, the dominance of a few ice species are clear [Gleitz *et al.* 1998]. In a recent review on the contribution of sea ice algae to Antarctic marine primary production, Lizotte [2001] found that only three species appear to be dominant in sea ice communities: the small pennate diatoms *Fragilariopsis cylindrus* and *Fragilariopsis curta* and the prymnesiophyte *Phaeocystis antarctica*. There are no obvious differences in the regional distribution of these species, but in most studies in the Weddell Sea the relative abundance of *F. cylindrus* in ice floes as compared to other species increases with the age of the floe. Although many species are accumulated during sea ice formation, low diversity for older sea ice suggest that only a few species are capable to survive and grow in such extreme environment [Gleitz *et al.* 1998].

The importance of the sea ice microalgae for the Antarctic ecosystem can be recognized through the diversity of the ice associated fauna. Foraminifera [Dieckmann *et al.* 1991b], copepods [Schnack-Schiel *et al.* 1998] and krill species have also been found associated with particular ice types. Daly [1998] found that in the Bellingshausen Sea, the Antarctic krill *Euphasia superba* depends on the sea ice microalgae as a winter food source and beneath the seasonal sea ice zone, krill abundances are relative low at depths in the water column but high (up to $1\text{-}28 \times 10^3$ animals m^{-3}) just at the ice-water interface. These observations suggest that regional and seasonal variations in sea ice extent can impact the overwintering strategy of Antarctic krill.

1.1.3 Sea Ice Formation and Growth

Marked regional differences in the distribution of sea ice biological communities are mainly associated with the spatial variability of physical processes that controls ice formation [Ackley and Sullivan 1994]. Early studies in the Antarctic pack-ice [Gow *et al.* 1982] demonstrated that most of the ice cores collected through all seasons consist, in part, of small randomly oriented crystals of frazil origin. It was not until 1986 during the Winter Weddell Sea Project on board the RV *Polarstern* that this mechanism of ice formation was elucidated. The *pancake cycle* was identified by Lange *et al.* [1989] as the source of most of the first-year sea ice inside the pack. The suspension of frazil crystals in the water are moved in cyclic or-

bits due to the action of wave field, commonly found in the advancing ice edge region. At the surface, ice crystals freeze together due to the compression caused by waves, forming small cakes of slush ice which grow larger by accretion of more frazil ice. The collisions between slush cakes pumps more frazil ice in the border of the cakes growing in a *pancake*-like form of ice floe. The pancakes at the ice edge are a few centimeters in diameter, gradually growing with increasing distance from the wave-active ice edge. They may reach 3-5 m diameter and thickness around 50 cm in just few days.

Far from the ice edge, the ice pancakes begin to freeze together in small groups of floes, although observations in the autumn and winter showed that the Antarctic wave field at the edge is strong enough to prevent an overall freezing up to 250 km from the ice front [Wadhams 2000]. Rafting of pancakes together with subsequent freezing forms the base of a continuous sheet of first-year ice, reducing the area of contact between the atmosphere and the ocean, which in turn reduces ice growth rate. At this point, the regime of ice growth changes from frazil to *congelation ice*, where a fabric of long crystals in columnar structure characterizes the vertical ice texture. These changes in the ice growth regime produce alterations in the ice texture that can be observed with the naked eye (Fig. 1.5).

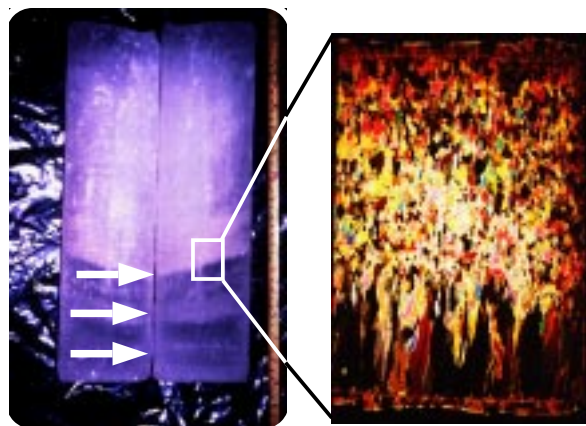


Figure 1.5: A sea ice core from the Weddell Sea showing vertical heterogeneity in the ice structure. The white arrows (left) indicate the zone of alteration in the ice texture. The zoom box (right) shows the size of ice crystals at the boundary between frazil and congelation ice.

Oscillations in air temperature and oceanic heat flux also produce significant heterogeneity in the ice texture, leading to changes in the temperature and salinity ice profiles (since the diffusion of heat depends on the vertical distribution of brine) [Cole and Shapiro 1998]. Particulate matter and inorganic nutrients within the brine are also strongly affected by these

changes [Smith *et al.* 1990, Lizotte and Sullivan 1991, Dieckmann *et al.* 1991a], mainly due to vertical gradients in brine flux. Significant advances in modeling the vertical gradients in the brine volume, temperature and salinity have been made by many authors [Cox and Weeks 1988, Eicken 1992, Fichfet and Morales Maqueda 1999], but its influence on the distribution of biological communities (surface, internal or bottom communities) have still not been completely investigated. The importance of the pancake cycle for the incorporation of biological material in the sea ice was studied by many authors Garrison *et al.* [1983], Weissenberger and Grossmann [1998], but the ultimately effects of thermodynamic ice growth in the biological production are not completely understood.

1.2 Primary Production Estimates of Antarctic Sea Ice

The ecological role of Antarctic sea ice communities has been a subject of intensive investigation only in the last 40 years, even though the existence of a complex sea ice biota was already described by Hooker in 1847. Many studies on the seasonal dynamics of sea ice habitats have been focused in coastal regions, due to their proximity to land-based facilities and therefore, the scientific knowledge about sea ice ecology is almost restricted to *fast-ice*, the dominant sea ice regime in such regions. Fast ice is formed mainly by thermodynamic growth (congelation ice) and in some Antarctic areas by incorporation and posterior freezing of platelet ice (see Jeffries *et al.* [1993] for a description of physical processes and Günther and Dieckmann [1999] for biology). Bottom communities are characteristic of fast-ice [Matsuda *et al.* 1990, Arrigo *et al.* 1993, Günther and Dieckmann 1999] and when comparing this ecosystem to the more extensive pack-ice regime, it becomes clear that important information related to off-shore conditions are lacking (e.g. light, nutrient dynamics and sea ice formation). Some attempts to characterize the pack-ice have been made by many authors [Garrison *et al.* 1987, Lizotte and Sullivan 1991, Sullivan *et al.* 1992, Garrison and Close 1993, Arrigo *et al.* 1997, Fritsen *et al.* 1998], but beyond a general view of microalgal habitats, little attention has been paid to the interactions between physical and biological processes and their effect in the associated primary production.

A significant degree of complexity has been found in the ecological structure of sea ice communities showing a clear association between a large number of species (bacteria, mi-

croalgae, protists, small metazoans and some crustaceans) during the initial stages of the Antarctic pack-ice formation [Garrison 1991]. However, many field studies showed that although this ecological complexity the sea ice microbial food-web are basically supported by microalgal primary production in a diatom-dominated community (see Lizotte [2001] for a review). A recent work of Gleitz *et al.* [1998] demonstrated that for more than 100 different diatoms species already found in sea ice habitats, only less than 20 contribute significantly to the total producers biomass. This singular characteristic is related to the physiological capacity of these diatoms to maintain relatively high production rates under extreme conditions of low light and temperature.

Primary production measurements in sea ice are much less common than phytoplankton studies in the Southern Ocean. Whereas estimates of the total Antarctic phytoplankton production were initiated in 1967 [El-Sayed 1967], measurements of production in sea ice have been restricted to near shore sites, making extrapolation to the pack-ice difficult [Spindler and Dieckmann 1994]. In the later 1980s, when the marginal ice zone and the pack-ice began to receive more scientific attention, estimates of primary production in sea ice became more prevalent [Kottmeier and Sullivan 1990, Garrison and Buck 1991, Lizotte and Sullivan 1991, Garrison and Close 1993]. However, the methods used to measure biological production within sea ice were basically derived from the same procedure as used in the water column: radiocarbon incorporation (C^{14}) on melted ice samples for short periods of incubation. The osmotic changes experienced by the ice biota during the melting of the ice sample and variations in the *in situ* temperature due to sample manipulation contribute to methodological uncertainty.

Recently, technical advances were made in measuring sea ice primary production. Mock and Gradinger [1999] proposed a new *in situ* incubation technique which was successfully applied in the Arctic sea ice. Almost at the same time, McMinn and Ashworth [1998] started using oxygen micro-electrodes to determine the net production by an Antarctic sea ice algal community. Unfortunately, those techniques are still not a standard procedure in the sea ice investigation programs and it will take a long time to obtain a more detailed view of the total estimates of the sea ice primary production.

An alternative method to overcome the problem of field measurements is the use of mathematical models. With the increasing number of experimental studies on sea ice communi-

ties in the last decade and based on field observations of multidisciplinary sea ice programs, its possible to produce reliable biological-physical models to estimate the sea ice primary production.

1.2.1 Modeling Antarctic Sea Ice Biology

In the early 1930s, Evelyn Hutchinson began the first attempts to introduce mathematical models in ecology [Mills 1989], although the design of such models were based on a still older concept - *logistic equations with self-limitation*, introduced by the Belgian mathematician Pierre F. Verhulst in 1838. It is almost impossible to imagine a modern discussion on population dynamics without the use of models. However, the mathematical description of any biological process is a complex task. It needs basic skills in mathematics (which is a common problem for biologists) and the necessary biological knowledge about the process to be modeled (which is a common problem for mathematicians). The first biological modeling study on the Antarctic marine ecosystem dates back to the work of Lancelot *et al.* [1991b], who simulated microalgal growth in the marginal ice zone. Their work was extended to a more complex model [Lancelot *et al.* 1991a] which included functional cellular pools (macromolecules, small metabolites and reserve products) describing physiological aspects of the microbial population in sea ice. Arrigo *et al.* [1991], using a more bio-optical approach, presented a model for the sea ice microbial communities of fast-ice in McMurdo Sound, Antarctica, extending their results later to the pack-ice. The modern estimates of the total carbon production in Antarctic sea ice are based on these modeling studies [Arrigo and Sullivan 1994, Arrigo *et al.* 1997; 1998]. Fritsen *et al.* [1998] suggested another approach to simulate primary production in sea ice attempting to include better descriptions of thermodynamic processes involved in the ice growth and their effects on the biological production. However, simplified relationships between light, temperature and algal growth employed in these models were not sufficient to represent the high degree of variability in the sea ice biological biomass, physical properties and ice texture found in field samples. Most of the models are restricted to specific communities (surface, interior and bottom communities independently) making difficult their interpretation regarding the effects of physical variability in the sea ice environment.

Nevertheless, several attempts to estimate the contribution of sea ice algae to total pri-

mary production in the Southern Ocean have been made, ranging from 36 to 70 Tg C year⁻¹ (from Arrigo *et al.* [1997] and Legendre *et al.* [1992], respectively). Assuming the total annual carbon production for the Southern Ocean to be around 1,300 Tg C year⁻¹ [JGOFS 1998], the sea ice contributes roughly 3-5%. However, Arrigo *et al.* [1997] found that this sea ice primary production represents a much larger fraction (10-28%) of the total production in the ice covered fraction of the Southern Ocean, which ranges from 140 to 385 Tg C year⁻¹ [Smith Jr. and Nelson 1991, Legendre *et al.* 1992]. Despite this relatively low contribution, the distribution and timing of sea ice microalgal production have a significant ecological importance as compared with the phytoplankton. Ice covered regions have, in general, low or no production in the water column since the solar light is almost completely attenuated by the sea ice.

1.3 Motivation and Objectives

Poor confidence in the total primary production estimates result from sparse observational data which have been collected primarily in the marginal ice zone or close to coastal regions. Our inability to simulate different biological processes in the range of sea ice regimes in question results from model simplifications, mainly in the physical processes that control ice growth and decay. Knowledge of factors governing sea ice primary production is still not complete and many questions remain to be answered:

- How does variability in thermodynamic ice growth affect the incorporation and vertical distribution of biological material within sea ice ?
- How strong are the effects of environmental factors (e.g. light, temperature, nutrient fluxes) on the growth rates of the sea ice biota during the complete sea ice seasonal cycle ?
- Does ice transport (drift) affect the distribution of biomass associated to sea ice ?

The motivation of this work was to construct a reliable coupled biological-physical sea ice model including all important aspects of ice growth and decay, as well as intrinsic physiological aspects of the sea ice community. An attempt is made to maintain a closer alliance

between observations (which provide a biased and undersampled view of reality) and a concise mathematical description of the model (which is always a gross simplification of reality). Coupling biological and physical processes in a model creates the dilemma of linking small scale processes typically observed in biology with larger scale patterns of ice physics (Fig. 1.6).

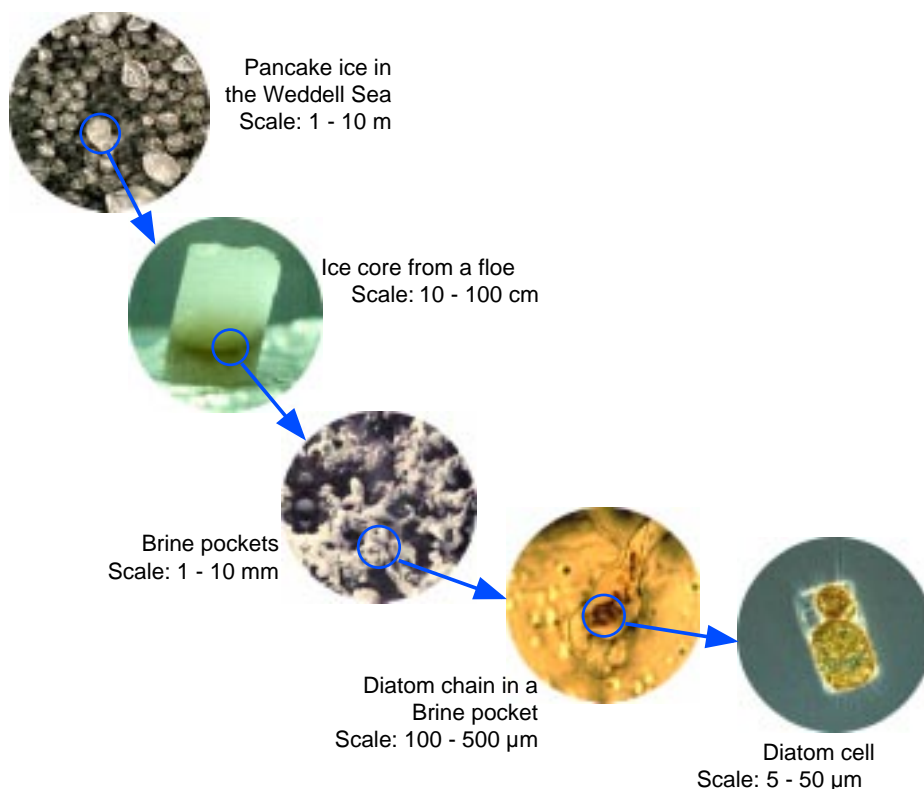


Figure 1.6: Comparison between physical and biological scales in sea ice.

In the next chapter a physiological self-adaptive model for the sea ice microbial community is presented, where microalgal growth is simulated based on uptake of dissolved inorganic nitrogen and silicate partially decoupled of carbon biomass production allowing variable N:C and Si:C ratios. The light-dependent photosynthetic carbon assimilation is linked with cellular N and Si quotas (Droop model) and the synthesis of Chlorophyll-*a*, provided by a mathematical approach representing photoacclimation processes. Grazing is simulated by incorporating protozoa carbon and nitrogen ingestion functions, with special emphasis on the remineralization of excess nitrogen in the food supply. The mathematical behavior and ecological consequences of simulated biological processes, as well as the importance of all physical forcing parameters, are discussed in detail.

Chapter 3 contains the description of the solar spectral model and the bio-optical sea ice model used to simulate the incoming solar radiation available to photosynthesis and thermodynamic processes in the sea ice. How the vertical gradient of chlorophyll-*a* concentration in sea ice affects the light attenuation within sea ice is also discussed.

The one-dimensional thermodynamic sea ice model is described in the Chapter 4. The model contains an analytical scheme to simulate brine flux and desalination processes, which governs the incorporation and accumulation of biological material during ice growth.

In the Chapter 5, the coupled physical and biological model is applied on field observations in the Weddell Sea, simulating the sea ice dynamics (drift and thermodynamics) and its implications to the characterization of biological communities within sea ice.

Based on model results and field observations, an estimate of the seasonal distribution of sea ice chlorophyll-*a* biomass and the associated primary production in the Weddell Sea are made in the Chapter 6.

A general discussion and conclusions are presented in the Chapter 7, including an outlook for future studies.

Chapter 2

The Biological Sea Ice Model

Until a few years ago, most of our knowledge on sea ice biological processes had only an empirical background relying solely on observational data. With the advent of new investigational techniques and extrapolation from experimental results to the real world, it is now possible to produce complete *mechanistic models* to study the sea ice ecosystem. The term *mechanistic* means that the model is based on different components (or biological processes) working together in a dynamic system. Such an approach differs considerably from the existent biological sea ice models [e.g. Arrigo *et al.* 1991, Fritsen *et al.* 1998], which are based almost totally on empirical relationships between light, temperature and photosynthesis. Basically, the main difference between empirical and mechanistic models resides in the use of self-adapting variables by the latter to predict future states of biological variables. This mathematical approach is based upon underlying physiological processes of model components (microalgae and grazers) and offers a better understanding of the effects of environmental variables in the biological processes in question. Empirical models are based directly on input parameters, which lack self-adapting variables as in a mechanistic model. Considering the small number of assumptions involved in an empirical model, the probability that they are incorrect is smaller than the probability of error in the large set of parameters normally used in mechanistic approaches. However, little can be learned from empirical models because all model variables are already based on predefined parameters. Particularly in the case of sea ice, where microbial communities are subject to strong seasonal and daily variations in light, temperature and nutrient, only a mechanistic model can well represent the physiological responses of microorganisms to the environmental changes.

In this Chapter, a sea ice biological model with self-adapting physiological mechanisms is described. The term *self-adapting* means a modification in structure, function or efficiency that improves the chance of survival during changes in environmental conditions. This is the

first attempt to model such biological process in sea ice, contributing to the understanding of physical-biological interactions in the sea ice biota.

2.1 Basic Concepts

To model biological processes in the sea ice ecosystem, it is necessary to determine which groups of microorganisms are representative in terms of biomass and their ecological meaning. Garrison [1991] showed that although the large number of species that inhabit sea ice (bacteria, microalgae, protists, small metazoans and some crustaceans), the ecological community is in general supported by a (diatom dominated) microalgal primary production. Gleitz *et al.* [1998] demonstrated that for more than 100 different diatoms species already found in sea ice habitats, only less than 20 contribute significantly to the total biomass and in a recent review, Lizotte [2001] suggested that two diatoms are the most dominant microalgae in sea ice: *Fragilariopsis cylindrus* and *F. curta*. This singular characteristic may be related to the physiological capacity of these diatoms to maintain relatively high growth rates under extreme conditions of low light and temperature [Gleitz *et al.* 1996] when compared with other water column species.

This apparent dominance of few species is also found between the heterotrophic protists in sea ice. Garrison and Buck [1989] working with pack-ice microbial communities in the Weddell Sea found that ciliates contributed to 70% of the total heterotrophic biomass, followed by heterotrophic flagellates and other small protists. Grazers play a key role in the cycling of material (e.g. excretion of nitrogen) and in controlling microalgal growth [Garrison 1991]. Grazers are incorporated into the ice during its formation and the development of large brine channels in the bottom-most layers also allows small metazoans from the water column to obtain access to sea ice organisms [Pasternak 1995, Schnack-Schiel *et al.* 1998], but with a small contribution to the total consumers C-biomass in sea ice.

Following the assumptions above, the sea ice biological model is based upon a two-component system containing sea ice microalgae (diatoms), defined in the model by the letter P , and heterotrophic protists, defined by the letter Z . Sea ice microalgae grow over two essential co-limiting nutrients, dissolved inorganic nitrogen ($[N]$) and silicate ($[Si]$), and its biomass is represented in terms of its carbon content (P^C), chlorophyll- a (P^{Chl}), particulate

organic nitrogen (P^N) and biogenic silica (P^{Si}). Heterotrophic protists feed on microalgae accumulating carbon and nitrogen biomass (Z^C and Z^N , respectively). Remineralization of Silica is neglected in the model, as are other nutrients and trace elements, like phosphate, iron, aluminium and vitamins, due to the lack of experimental data on the uptake of these elements by sea ice communities. Figure 2.1 shows a schematic representation of mass fluxes in the model.

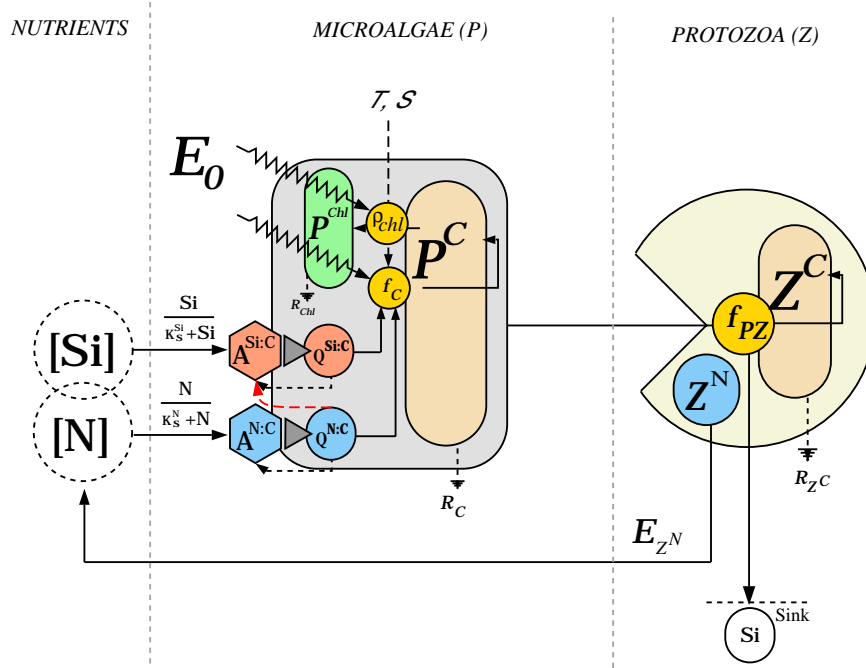


Figure 2.1: Schematic representation of the sea ice biological model showing main fluxes of matter and rate processes. Symbols are listed in the tables 2.1 and 2.2.

2.2 Model Description

Sea ice microalgal growth is described by light-dependent carbon assimilation (photosynthesis) partially decoupled of nutrient uptake functions, allowing variable N:C and Si:C cellular quotas [Droop 1973]. Symbols and definitions are summarized in the tables 2.1 and 2.2. The net rate of carbon biomass accumulation is described by

$$\frac{dP^C}{dt} = (f_C - R_C) P^C - f_{PZ} Z^C \quad (2.1)$$

where the first term on the right hand side represents the balanced C-specific photosynthetic rate (production - respiration) and the second term is the carbon loss due to grazing.

Part of the assimilated carbon is transferred to chlorophyll-*a* synthesis assuming that microalgae can photo-acclimate dynamically. The rate of chlorophyll-*a* production is given by

$$\frac{dP^{Chl}}{dt} = \rho_{Chl} f_C P^C - R_{Chl} P^{Chl} - f_{PZ} Q^{Chl:C} Z^C \quad (2.2)$$

where the first term on the right hand side is the Chl-*a*:C synthesis ratio, the second term is the chl-*a* degradation rate and last term is the loss of chlorophyll-*a* due to grazing.

Table 2.1: Prognostic variables in the biological sea ice model.

Symbol	Definition	Units
[N]	Dissolved nitrogen concentration	$\mu\text{M [N]}$
[Si]	Silicate concentration	$\mu\text{M [Si]}$
P^C	Microalgal carbon biomass	$\mu\text{M C}$
P^{chl}	Microalgal chlorophyll- <i>a</i> biomass	$\mu\text{g Chl l}^{-1}$
P^N	Microalgal organic nitrogen biomass	$\mu\text{M N}$
P^{Si}	Microalgal biogenic silica	$\mu\text{M Si}$
Z^C	Protozoan carbon biomass	$\mu\text{M C}$
Z^N	Protozoan organic nitrogen biomass	$\mu\text{M N}$

During microalgal growth, the balance between dissolved inorganic nutrients and cellular pools of N and Si results from accumulation and incorporation functions, which are controlled by basic cellular requirements. Grazing acts as a loss term for both particulate organic nitrogen and biogenic silica, although excess of nitrogen in the protozoa N-biomass is exported to the dissolved [N] pool. The equations describing nutrient balance are

$$\frac{d[\text{N}]}{dt} = -\frac{A^{N:C}}{Q^{N:C}} P^N + E_{Z^N} Z^C \quad (2.3)$$

$$\frac{d[\text{Si}]}{dt} = -\frac{A^{Si:C}}{Q^{Si:C}} P^{Si} \quad (2.4)$$

$$\frac{dP^N}{dt} = \frac{A^{N:C}}{Q^{N:C}} P^N - f_{PZ} Q^{N:C} Z^C \quad (2.5)$$

$$\frac{dP^{Si}}{dt} = \frac{A^{Si:C}}{Q^{Si:C}} P^{Si} - f_{PZ} Q^{Si:C} Z^C \quad (2.6)$$

where the first term on the right hand side of all equations are the carbon-specific uptake rates of nutrients ($A^{N:C}$ and $A^{Si:C}$) normalized to the N:C and Si:C cellular ratios ($Q^{N:C}$ and

$Q^{Si:C}$). The second term on the right hand side of Eqs. (2.5) and (2.6) are nutrient-specific loss terms due to grazing and the second term in Eq. (2.3) represents the input of recycled N (excretion) by protozoa.

Net accumulation of carbon and nitrogen in the protozoa is simulated by the balance between the carbon-specific ingestion f_{PZ} and respiration R_{Z^C} rates, and by the N:C cellular ratio $Q^{N:C}$, defined as

$$\frac{dZ^C}{dt} = f_{PZ} Z^C - R_{Z^C} Z^C \quad (2.7)$$

$$\frac{dZ^N}{dt} = f_{PZ} Q^{N:C} Z^C - E_{Z^N} Z^C \quad (2.8)$$

where E_{Z^N} is the nitrogen excretion rate.

The biological concept behind this approach is based on the nutritional status of the microorganisms represented by their elemental ratios. Equations (2.1) to (2.8) form a complete model to describe the dynamic flux of elements (C, Chl, N and Si) in a sea ice biological system. A series of intermediate variables that *diagnose* the physiological states of microalgae and heterotrophic protists (table 2.2) is responsible for the mechanistic character of the model.

Table 2.2: Diagnostic variables in the biological sea ice model.

Symbol	Definition	Units
$A^{N:C}$	C-specific nitrogen uptake rate	g N (g C) ⁻¹ h ⁻¹
$Q^{N:C}$	Microalgal N:C cellular quota	g N (g C) ⁻¹
$A^{Si:C}$	C-specific silicate uptake rate	g Si (g C) ⁻¹ h ⁻¹
$Q^{Si:C}$	Microalgal Si:C cellular quota	g Si (g C) ⁻¹
$Q^{Chl:C}$	Microalgal Chl:C cellular quota	g Chl- <i>a</i> (g C) ⁻¹
ρ_{Chl}	Chl- <i>a</i> :C synthesis ratio	g Chl- <i>a</i> (g C) ⁻¹
R_{Chl}	Chl- <i>a</i> degradation rate	h ⁻¹
f_C	C-specific photosynthetic rate	h ⁻¹
R_C	Microalgae respiration rate	h ⁻¹
f_{C_m}	Light-saturated photosynthetic rate	h ⁻¹
f_{PZ}	C-specific heterotroph ingestion rate	h ⁻¹
R_{Z^C}	Protozoa C-respiration rate	h ⁻¹
E_{Z^N}	Protozoa C-specific N excretion rate	g N (g C) ⁻¹ h ⁻¹

The biological responses to transient changes in environmental conditions are based on specific ranges defined by the minimum and maximum cellular N:C and Si:C quotas. Such

physiological states control accumulation and production/ingestion processes generating a feedback to the nutritional status of the microorganisms. This *self-adapting* mechanism describes how physiological states control the time-dependent processes of growth and biomass accumulation: the carbon-specific light-saturated photosynthetic rate (f_{C_m}) depending on temperature and cellular N:C and Si:C ratios; the relationship between the Chl-*a*:C ratio ($Q^{Chl:C}$) and the carbon-specific light-limited photosynthetic rate (f_C); the chlorophyll-*a* biosynthesis (ρ_{Chl}) with a photoacclimation scheme; nutrient uptake functions ($A^{N:C}$ and $A^{Si:C}$) regulated by the nutritional status of cells ($Q^{N:C}$ and $Q^{Si:C}$); nitrogen excess excretion (E_{ZN}) as a function of minimum cellular requirements of heterotrophic protists.

All these mechanisms can be grouped in five main biological processes, which will be described in detail in the next subsections (Primary Production, Regulation of Chlorophyll-to-Carbon Ratio, Nutrient Dynamics, Grazing and Nitrogen Recycling)

2.2.1 Primary Production

The rate of primary production given by Eq. (2.1) is represented by the instantaneous carbon-specific photosynthetic rate (f_C) calculated through the relationship between incident light E_0 and the light-saturated photosynthetic rate f_{C_m} , which depends on temperature and cellular nutritional status. This description was first introduced by Platt and Jassby [1976] and modified by Geider *et al.* [1996] to represent the effect of a variable Chl-*a*:C ratio on the efficiency of the photosynthetic carbon assimilation neglecting photo-inhibition

$$f_C = f_{C_m} \left[1 - \exp \left(- \frac{\alpha^{Chl} E_0 Q^{Chl:C}}{f_{C_m}} \right) \right] \quad (2.9)$$

where f_{C_m} is the C-specific light saturated photosynthetic rate (h^{-1}), E_0 is the incident irradiance in PAR¹ ($\mu\text{mol photons m}^{-2} \text{s}^{-1}$), α^{Chl} is the chlorophyll-specific photosynthetic efficiency ($\mu\text{g C} (\mu\text{g Chl})^{-1} \text{m}^2 (\mu\text{mol photons})^{-1}$) and $Q^{Chl:C}$ is the instantaneous Chl-*a*:C ratio ($\text{g Chl-}a (\text{g C})^{-1}$). Most of the experimental data on primary production of natural populations are based on methods of radiocarbon incorporation (C^{14}) giving estimates of the maximum chlorophyll-specific primary production P_m^B (in unit of $\mu\text{g C} (\mu\text{g Chl})^{-1} \text{h}^{-1}$). P_m^B is converted into carbon-specific photosynthetic rate by multiplying P_m^B and the chlorophyll-

¹Photosynthetically Available Radiance - see Morel [1978] for details.

to-carbon ratio $Q^{Chl:C}$.

The light-saturated photosynthesis, as well as all physiological rates, depend on the temperature and the nutritional status of the cells. Geider *et al.* [1997] demonstrated that these factors have a major impact on the maximum light-saturated photosynthetic rate under optimal conditions ($f_{C_{max}}$), which is related to f_{C_m} by

$$f_{C_m} = f_{C_{max}} T_{lim} A_{lim} \quad (2.10)$$

where A_{lim} the cellular nutrient limitation (explained in detail on section 2.2.3) and T_{lim} is the temperature limitation factor.

Arrhenius in 1889 proposed a description for the temperature-dependent physiological rate k under temperature T given by an exponential function $k(T) = k_0 \exp(-T_A/T)$, where T_A is known as the Arrhenius temperature and k_0 is related to the physiological rate at a reference temperature. Arrhenius based his studies in the classical model of van't Hoff, known as the temperature quotient Q_{10} . It gives the change in the rate k for every 10°C gradient in the temperature described by

$$k(T) = k_0 Q_{10}^{(T-T_0)/10} \quad (2.11)$$

[Eppley 1972] also used a similar formulation to determine the temperature dependent growth rate for circa 130 marine phytoplankton species. Although Eppley's work includes only mesophilic species, it was used by many authors to model algal growth in sea ice [e.g. Arrigo *et al.* 1991, Arrigo and Sullivan 1992; 1994, Fritsen *et al.* 1998]. However some experimental data from Antarctic phytoplankton and sea ice microalgae show growth rates that are above the Eppley's curve [Neori and Holm Hansen 1982, Tilzer *et al.* 1986, Fiala and Oriol 1990]. Assuming that the instantaneous growth rate is directly related to the rate of carbon assimilation ($\mu = \frac{1}{PC} \frac{dPC}{dt}$), a comparison between Eppley's curve and f_{C_m} is possible (Fig. 2.2).

The experimental data (shown in the Fig. 2.2) also includes nutrient limitation effects (A_{lim}) which is difficult to assert directly from the data. Neori and Holm Hansen [1982] found that during the austral summer, the rate of photosynthesis in Antarctic phytoplankton can be limited by temperature effects on metabolic reactions constrained in a specific range

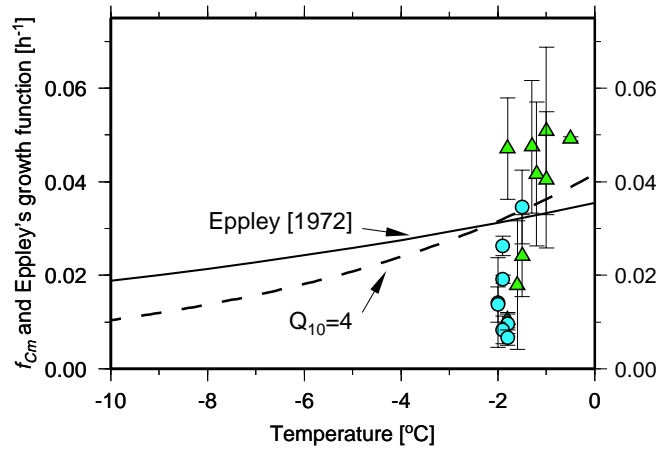


Figure 2.2: Temperature-dependent maximum photosynthetic rate f_{C_m} for phytoplankton (triangles) and sea ice microalgae (circles) from primary production experiments in the Arctic and Antarctic (see table 2.3). The solid line is the Eppley's temperature dependent growth rate and the dashed line represents $f_{C_m} = f_{C_{max}} T_{lim}$ using Eq. (2.11) for a $Q_{10}=4$ (following Tilzer *et al.* [1986]) and $f_{C_{max}}=0.042 \text{ h}^{-1}$. The reference temperature T_0 is 0°C .

of temperature, despite of high nutrient concentrations and saturating light levels. Based on experimental data, the optimal temperature range for sea ice microalgae and polar marine phytoplankton may be delimited between -8 and 5°C [Tilzer *et al.* 1986, Fiala and Oriol 1990] with a $Q_{10}=4$ over the maximum light-saturated photosynthetic rate.

Temperature affects several physiological processes in autotrophic cells: the caption of photons by the light-harvesting complex is less effected by temperature than carbon dioxide binding by Rubisco, which causes an electron leak at low temperatures [Allan and Ort 2001]. Considering the regulation of photosynthesis vs. temperature in different taxa (see discussion in Dijkman [2001] and Allan and Ort [2001]), temperature tolerance ranges of autotrophic cells have major evolutionary implications. As observations of f_{C_m} under extreme low temperatures ($\leq -2^\circ\text{C}$) together with measurements of carbon incorporation are still lacking for sea ice, an extrapolation of the data above assuming a $Q_{10}=4$ for f_{C_m} under freezing temperatures is used as a conservative approximation.

2.2.2 Regulation of Chlorophyll-to-Carbon Ratio

The rate of carbon fixation depends of the size and efficiency of the light-harvesting complex (i.e. it is proportional to the product of Chl-*a* concentration and irradiance) and shows a large variability in natural populations [Geider and Platt 1986]. It is then obvious that the photosynthetic rate cannot be parameterized with a time invariable chlorophyll-to-carbon

Table 2.3: Light-saturated C-specific photosynthetic rate of Antarctic phytoplankton and sea ice algae obtained from primary production experiments. f_{C_m} is obtained multiplying the light-saturated Chl-specific primary production P_m^B for the chlorophyll-to-carbon ratio $Q^{Chl:C}$.

Temp. °C	mean f_{C_m} h^{-1}	Type	Local	Source
-1.8	0.047	water	Arctic	Irwin [1990]
-1.5	0.035	sea ice	Arctic	“
-1.8	0.011	water	Arctic	Johnsen and Hegseth [1991]
-1.9	0.019	sea ice	Antarctic	Priscu <i>et al.</i> [1991]
-1.0	0.051	water	Antarctic	Tilzer <i>et al.</i> [1986]
-1.3	0.047	water	Antarctic	“
-1.2	0.042	water	Antarctic	“
-0.5	0.049	water	Antarctic	“
0.0	0.046	water	Antarctic	“
-1.6	0.018	water	Antarctic	Tilzer <i>et al.</i> [1985]
-1.0	0.040	water	Antarctic	Dower <i>et al.</i> [1996]
-1.8	0.009	sea ice	Arctic	Suzuki <i>et al.</i> [1997]
-1.9	0.008	sea ice	Antarctic	Cota and Sullivan [1990]
-2.0	0.014	sea ice	Antarctic	Palmisano <i>et al.</i> [1986]
2.0	0.038	sea ice	Antarctic	“
-1.8	0.006	sea ice	Antarctic	Palmisano <i>et al.</i> [1985]
-2.0	0.014	sea ice	Antarctic	Robinson <i>et al.</i> [1995]
-1.5	0.024	water	Antarctic	Thomas <i>et al.</i> [1992]
0.0	0.026	water	Antarctic	“
4.0	0.037	water	Antarctic	“
-1.9	0.026	sea ice	Antarctic	Lizotte and Sullivan [1991]

ratio. In the sea ice, microalgae can be exposed to relatively long dark periods (under heavy snow loading and during the winter) or high levels of irradiance (specially true for surface assemblages in the summer) and a mechanism of photoacclimation is responsible to regulate the efficiency of the light harvesting complex to transient changes in the light conditions [Thomas *et al.* 1992].

In the model, the chlorophyll-*a* synthesis is treated as the product of photosynthesis and is proportional to the carbon fixation rate redirected to chlorophyll-*a* biosynthesis. This Chl-*a*:C synthesis ratio ρ_{Chl} is described by

$$\rho_{Chl} = Q_{max}^{Chl:C} \left(\frac{f_C}{\alpha^{Chl} E_0 Q^{Chl:C}} \right) \quad (2.12)$$

where the term $Q_{max}^{Chl:C}$ is the maximum Chl-*a*:C ratio observed in cells adapted to extremely

low light levels, α^{Chl} is the chlorophyll-specific photosynthetic efficiency and E_0 is the incident irradiance in PAR.

The concept of photoacclimation in microalgal growth models was introduced by Geider [1993] and extended in a series of studies about the importance of a self-adapting chlorophyll-to-carbon ratio to the primary productivity of marine phytoplankton [Geider *et al.* 1996; 1997; 1998]. It permits an explicit mathematical description of chlorophyll-*a* synthesis coupled to the carbon assimilation. The degradation term for Chl-*a*, R_{Chl} in the Eq. (2.2), and microalgal respiration rate, R_C in the Eq. (2.1), are considered regulatory terms in the model because they affect the net production of carbon and chlorophyll-*a* [Geider *et al.* 1998]. However, Thomas *et al.* [1992] in experiments with a small *Chaetoceros* species in the Weddell Sea found no significant respiration rates under freezing temperatures. Also, the degradation of chlorophyll-*a* plays a secondary role in the Chl-*a*:C synthesis process [Geider *et al.* 1996]. Thus, R_{Chl} and R_C are assumed to be zero for sea ice microalgae. They are included in the formulations to keep model consistency.

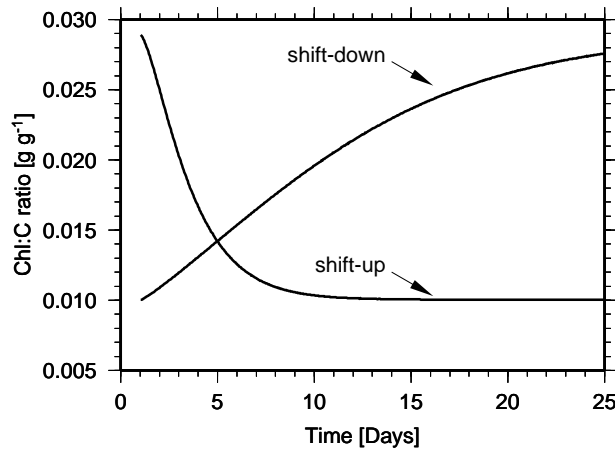


Figure 2.3: Changes in the chlorophyll-to-carbon ratio during alternate irradiance shifts between 5 and 100 $\mu\text{mol photons m}^{-2} \text{s}^{-1}$ under nutrient replete conditions. $Q_{max}^{Chl:C}$ is 0.035 and α^{Chl} is 2.5×10^{-5} .

The response of up- and down-regulation of Chl-*a*:C ratios to shifts in the irradiance occurs at different time scales (Fig. 2.3) because of a differential rate between the synthesis of Chl-*a* and carbon fixation. Under low light conditions, the rate of carbon fixation is limited by the rate of photosynthesis through basic cell physiological requirements. During an increase in the irradiance, the cell is not light limited and more carbon is assimilated with a smaller light harvesting complex. Under a shift-down in the irradiance, carbon fixation is

light limited, and consequently the Chl-*a*:C synthesis ratio is also limited. Short-term variations in the light field can lead to an oscillatory behavior of the chlorophyll-to-carbon ratio and is of major importance when determining the primary productivity in natural populations [MacIntyre *et al.* 2000].

2.2.3 Nutrient Dynamics

Since the classical work of Droop [1973] showing the importance of cellular nutrient pools or *quotas* to algal growth, many models have included formulations with variable N:C and Si:C ratios to simulate nutrient fluxes in marine food-webs [e.g. Aksnes and Egge 1991, Baretta Bekker *et al.* 1998, Aota and Nakajima 2000]. However, sea ice microalgal growth models [e.g. Arrigo *et al.* 1991, Fritsen *et al.* 1998] still use rectangular hyperbolic functions (Michaelis-Menten) to represent inorganic nutrient limitation on growth. Unfortunately, most of the algal growth models are derived from steady-state observations, and frequently consider a single limiting nutrient related to its cellular quota yield [e.g. Bernard and Gouzé 1995]. Flynn *et al.* [1994] showed that in natural conditions, cells are normally under stress due to transient changes in more than one nutrient.

To simulate this process, a co-limitation model for both dissolved inorganic and cellular nutrient quota is necessary. Here, uptake of dissolved nutrients (nitrogen and silicate) by microalgae is based on the work of Davidson and Gurney [1999] and Davidson *et al.* [1999]. Their model assumes that nitrogen is a nutrient with rapid turnover rate, integrating biochemical cellular processes. Flynn [1990] demonstrated that N stress induces changes in the uptake functions of microalgal cells to maximize their potential growth [Syrret *et al.* 1986]. The cellular silica pool is rather small. Thus cells which are Si-limited may sacrifice structural-Si requirements to meet metabolic needs [Paasche 1973]. Observations made by Sullivan [1979] show that only 15% of the total cellular silicon is represented by a transient pool of soluble-Si(OH)₄, suggesting a fast Si-deposition in the cell frustules. However, uptake and mobilization of silica in the cell requires energy and N-reserves, indicating that cellular nitrogen and Si-cycle must be coupled in a co-limitation scheme. Following Thingstad and Sakshaug [1990], nitrogen is defined as a controlling nutrient (i.e. essential for metabolic process of other nutrients and for growth) and Si as a limiting nutrient (i.e. essential nutrient for growth only). Cellular quotas are defined by $Q^{N:C} = P^N/P^C$ and $Q^{Si:C} = P^{Si}/P^C$.

Davidson and Gurney [1999] related the degree of reduction in the metabolic rate (γ) to the N:C quota using a Hill function (Fig. 2.4a) given by

$$\gamma = \begin{cases} 1 & \text{if } (Q^{N:C}/Q_{min}^{N:C}) < (Q^{Si:C}/Q_{min}^{Si:C}) \\ \left[\left(\frac{k_3}{Q^{N:C}} \right)^\beta + 1 \right]^{-1} & \text{otherwise} \end{cases} \quad (2.13)$$

where the exponent β determines the degree of inflection of the curve and k_3 is the half-saturation constant, $Q_{min}^{N:C}$ and $Q_{min}^{Si:C}$ are minimum cell quotas for N:C and Si:C, respectively.

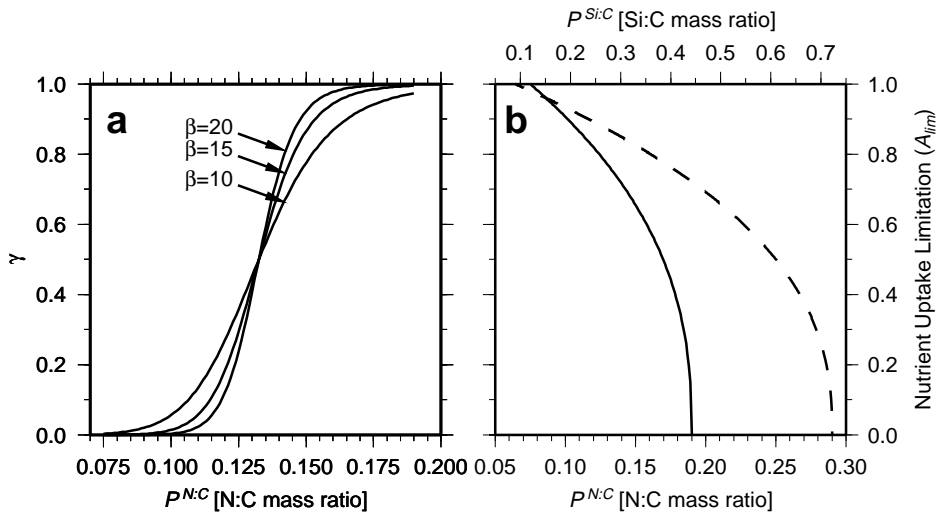


Figure 2.4: (a) The function γ controlling metabolic processes when Si is the limiting nutrient calculated for different β from Eq. (2.13). Minimum N:C quota ($Q_{min}^{N:C}$) is 0.075 and k_3 is 0.132. (b) Relation between uptake and intracellular nutrient quota from Eqs.s (2.15) and (2.16). The shape factor n is 0.4, $Q_{min}^{N:C}=0.075$, $Q_{max}^{N:C}=0.190$ (solid line), $Q_{min}^{Si:C}=0.09$ and $Q_{max}^{Si:C}=0.722$ (dashed line).

In the co-limitation model, nitrogen controls the uptake and growth when Si is a limiting nutrient ($Q^{N:C}/Q_{min}^{N:C} > Q^{Si:C}/Q_{min}^{Si:C}$). Another scenario is when N is the yield-limiting nutrient ($\gamma = 1$), assuming that intracellular Si will not affect the rate of N metabolism. The cellular limitation function A_{lim} , used in Eq. (2.10), is then defined by

$$A_{lim} = \gamma \frac{Q^{i:C} - Q_{min}^{i:C}}{Q_{max}^{i:C} - Q_{min}^{i:C}}$$

$$\text{for } i = \begin{cases} N & \text{if } Q^{N:C}/Q_{min}^{N:C} < Q^{Si:C}/Q_{min}^{Si:C} \\ Si & \text{otherwise} \end{cases} \quad (2.14)$$

where $Q_{max}^{N:C}$ and $Q_{max}^{Si:C}$ are the maximum cell quotas for N:C and Si:C, respectively. The

cellular nutritional status and the inorganic nutrient availability control together the uptake of nutrients. The carbon-specific nitrogen and silicate uptake rates are

$$A^{N:C} = A_{max}^{N:C} \frac{[N]}{k_N + [N]} \left(\frac{Q_{max}^{N:C} - Q^{N:C}}{Q_{max}^{N:C} - Q_{min}^{N:C}} \right)^n \gamma \quad (2.15)$$

$$A^{Si:C} = A_{max}^{Si:C} \frac{[Si]}{k_{Si} + [Si]} \left(\frac{Q_{max}^{Si:C} - Q^{Si:C}}{Q_{max}^{Si:C} - Q_{min}^{Si:C}} \right)^n \gamma \quad (2.16)$$

where the exponent n is the shape-factor for the relationship between uptake and N:C- and Si:C-quotas (Fig. 2.4b). To prevent unreliable cellular Si storage, $Q_{max}^{Si:C}$ is limited by the cellular nitrogen pool through a dumping factor ($\xi^{Si:N}$)

$$Q_{Si:C}^{max} = \xi^{Si:N} Q_{N:C} \quad (2.17)$$

Data collected from Antarctic phytoplankton [Sommer 1991, Nelson and Tréguer 1992], as well as empirically derived data from Davidson and Gurney [1999], suggested that $\xi^{Si:N}$ must range between 3 and 5. A value of $\xi^{Si:N} \approx 4$ is therefore used.

The nutrient co-limitation model is based on the fact that microalgal cells can maintain their nutritional status in a specific range of N:C and Si:C ratios. This approach, when applied in conjunction with the primary production and photoacclimation equations (subsections 2.2.1 and 2.2.2), shows a great flexibility to study time-dependent physiological changes under transient conditions in sea ice.

2.2.4 Grazing

The impact of herbivores on the sea ice primary production is still not well known, although the role of protists in controlling sea ice primary productivity and nutrient cycling have been recognized by many authors [e.g. Garrison and Buck 1989, Garrison 1991, Lancelot *et al.* 1991b, Archer *et al.* 1996]. Existing biological sea ice models use unsophisticated equations derived from linear functions correlating growth rates with grazing. However, herbivory is a continuous process, partially independent of primary production and related only to the availability of food.

In this work, sea ice herbivory is represented by protozoan feeding on sea ice microalgae with the carbon-specific ingestion rate, f_{PZ} , limited by the availability of food (microalgal

carbon biomass, P^C), according to

$$f_{PZ} = f_{PZ_{max}} \frac{(P^C - P_{thres}^C)}{k_{PC} + (P^C - P_{thres}^C)} \quad (2.18)$$

where $f_{PZ_{max}}$ is the temperature-dependent maximal ingestion rate, k_{PC} is the half-saturation constant for ingestion rate and P_{thres}^C is a minimum microalgal biomass constraining grazing. The temperature effect on $f_{PZ_{max}}$ and on the respiration rate is calculated over dominant size of heterotrophic protists in sea ice.

Garrison and Buck [1991] estimated herbivory in Antarctic sea ice using the allometric equations of Moloney and Field [1989] based on mass-specific maximum ingestion and respiration rates at 20°C reduced to 0°C assuming a $Q_{10}=3$

$$f_{PZ_{max}} = \left[0.292 Q_{10}^{(T-T_{ref})0.1} \right] M^{-0.25} \quad (h^{-1}) \quad (2.19)$$

$$R_{ZC} = \left[0.065 Q_{10}^{(T-T_{ref})0.1} \right] M^{-0.25} \quad (h^{-1}) \quad (2.20)$$

where M is the protozoa body mass in pg C cell^{-1} and $T_{ref} = 0^\circ\text{C}$ is the reference temperature. To calculate the maximum ingestion and respiration rates under freezing sea ice temperatures, Q_{10} is assumed to be 4 according to reported values for sea ice communities [Connolly and Coffin 1995, Laurion *et al.* 1995]. Maximum ingestion and respiration rates for sea ice protozoa are calculated to a generic heterotrophic protist with $3500 \text{ pg C cell}^{-1}$ body mass, which corresponds with measurements of Garrison and Buck [1991] for sea ice ciliates.

There are only a few observations of ingestion rates for sea ice protozoa, with a restricted temporal and spatial coverage [Garrison and Buck 1989, Garrison and Close 1993]. However Klaas [1996], working with *Protoperdinium cf. pelucidum* grazing on *Thalassiosira antarctica* in samples from the Antarctic Polar Front, found a half-saturation constant for the ingestion rate k_{PC} of $\approx 55 \mu\text{g C}_{prey} \text{ l}^{-1}$. Bjørnsen and Kuparinen [1991] also found a k_{PC} of $50 \mu\text{g C l}^{-1}$ working with dinoflagellate herbivory in the Scotia-Weddell Confluence zone. Therefore, a k_{PC} of $52 \mu\text{g C l}^{-1}$ ($=4.3 \mu\text{M C}_{prey}$) is used in the model. Following Garrison and Buck [1989] and Garrison and Close [1993], $P_{thres}^C=1.2 \mu\text{g C}_{prey} \text{ l}^{-1}$ ($=0.1 \mu\text{M C}_{prey}$) was chosen. Figure 2.5 shows the behavior of the C-specific ingestion functions for different

temperatures and predator-prey concentrations.

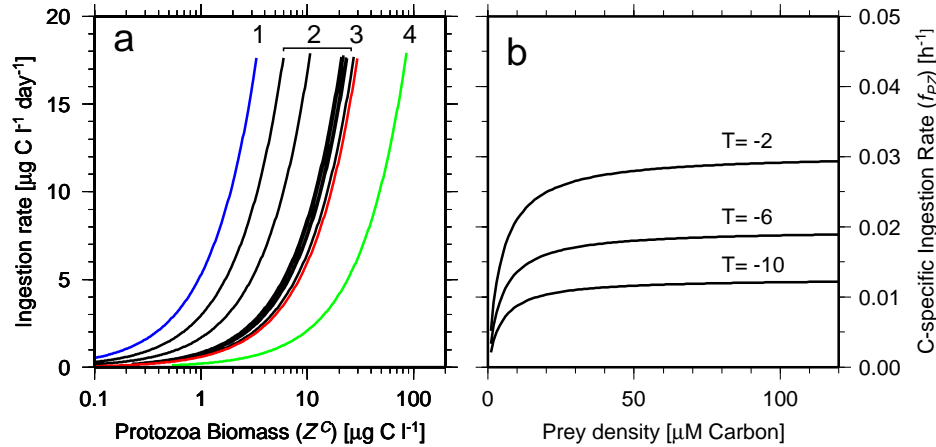


Figure 2.5: (a) C-specific maximum ingestion rates for sea ice heterotrophic protists, normalized to -1.7°C using a $Q_{10}=4$. Data from the literature, (1) Laurion *et al.* [1995], (2) Garrison and Buck [1991], (3) Bjørnsen and Kuperinen [1991] and (4) Klaas [1996]. (b) Instantaneous ingestion rates computed for a generic heterotroph with $3500 \text{ pg C cell}^{-1}$ body mass in function of prey concentration under three temperatures calculated by Eq. (2.18).

2.2.5 Nitrogen Recycling

The net carbon accumulation by heterotrophic protists (Z^C) is given by the difference between ingestion (determined by the availability of food as microalgae biomass) and respiration (proportional to the accumulated carbon). However, net nitrogen accumulation is related to their metabolic needs. In a review about predator-prey interactions in food-webs, Davidson [1996] suggested that the mechanism of N-recycling is correlated with the nutritional status of prey and also with basic requirements of predators. An excess of nitrogen in the food will enhance N-excretion by the grazers, whereas nitrogen depleted prey will induce a relatively higher carbon respiration compared to nitrogen excretion. Caron *et al.* [1990] and Davidson *et al.* [1995] proposed similar mechanisms to simulate N-recycling assuming that predators attempt to regulate their nutritional reserves and preserve a constant cellular N:C ratio. This mechanism can be mathematically described as

$$E_{ZN} = \begin{cases} 0 & \text{if } Q^{Z^{N:C}} < \delta_Z^{N:C} \\ R_{ZC} (2Q^{Z^{N:C}} - \delta_Z^{N:C}) & \text{otherwise} \end{cases} \quad (2.21)$$

where $Q^{Z^{N:C}}$ is the instantaneous protozoa nitrogen-to-carbon molar ratio and the parameter $\delta_Z^{N:C}$ is the optimum N:C molar ratio found in predators. From observations over different grazing experiments in the laboratory [Goldman and Dennett 1990, Flynn 1990, Flynn and Davidson 1993] and the Redfield ratio C:N=106:16, a $\delta_Z^{N:C} = 0.152$ (≈ 6.6 C:N molar) is assumed for sea ice protozoa. If the nitrogen-to-carbon ratio of predators is equal to $\delta_Z^{N:C}$, they retain the cellular N:C ratio respiring equivalent carbon and nitrogen biomass. If the nitrogen-to-carbon ratio drops below $\delta_Z^{N:C}$, the carbon excess is respired and cellular nitrogen is retained. For a N:C ratio higher than $\delta_Z^{N:C}$, nitrogen excess is excreted and represents a source of dissolved nitrogen.

2.3 Model Validation

Microalgal growth and primary productivity were the focus of many studies in Antarctic sea ice [e.g. Grossi *et al.* 1987, Rivkin and Putt 1987, Cota and Sullivan 1990, Thomas *et al.* 1992, Gleitz and Thomas 1993, Grossmann and Dieckmann 1994]. However, there is no available complete time-series of sea ice microalgal carbon, chlorophyll-*a*, N:C and Si:C cellular quotas for the pack-ice. Most of the data collected in the field are composed of short snapshots on the chlorophyll-*a* standing crop, or a few primary production measurements. On the other hand, some short-term studies in the Arctic were conducted in the last few years [e.g. Gosselin *et al.* 1997, Sherr *et al.* 1998]. Mock and Gradinger [2000] did experimental work with sea ice microalgae collected in the Barents Sea at the end of the melting season, between May-June 1997. Since the biological processes that regulate primary production in the Arctic and Antarctic sea ice are comparable, the experimental results of Mock and Gradinger [2000] are used to validate the model.

In their experimental design, three sea ice microalgal batch cultures were obtained from the bottom 5 cm of 33 ice cores and stored at -1.0°C and salinity 32.4 under continuous illumination ($\approx 15 \mu\text{mol photons m}^{-2} \text{s}^{-1}$). The cultures were filtered through a $100 \mu\text{m}$ sieve to exclude large grazers and after three days of acclimation the cultures were enriched with a nutrient mixture and sub sampled in intervals of 2 to 5 days through 25 days. Nutrient concentrations were analyzed according to the standard seawater procedure [Grasshoff *et al.* 1983], chlorophyll-*a* by the fluorimetric method [Arar and Collins 1992] and organic particulates (POC and PON) using a Haereus CHN-O-Rapid analyzer. The biogenic silica

in the cultures was calculated over the time variation of dissolved Si concentrations. Data collection and experimental design are discussed in detail by Mock and Gradinger [2000].

Table 2.4: Model parameters found by multidimensional fitting with experimental data and initial conditions for model integration.

Model Parameters			
Symbol	Value	Definition	Units
$f_{C_{max}}$	0.042	Maximum C-specific light-saturated photosynthetic rate	h^{-1}
$A_{max}^{N:C}$	0.083	Maximum C-specific nitrogen uptake rate	$\text{g N (g C)}^{-1} \text{h}^{-1}$
$A_{max}^{Si:C}$	0.030	Maximum C-specific silicate uptake rate	$\text{g Si (g C)}^{-1} \text{h}^{-1}$
k_N	1.0	Half-saturation constant for N uptake	$\mu\text{M [N]}$
k_{Si}	2.0	Half-saturation constant for Si uptake	$\mu\text{M [Si]}$
α^{chl}	2.5×10^{-5}	Chl-specific photosynthetic efficiency	$\text{g C (g Chl)}^{-1} \text{m}^2 \cdot (\mu\text{mol photons})^{-1}$
$Q_{max}^{Chl:C}$	0.035	Maximum Chlorophyll- <i>a</i> :Carbon ratio	g Chl (g C)^{-1}
$Q_{min}^{N:C}$	0.075	Minimum Microalgal N:C cellular quota	g N (g C)^{-1}
$Q_{max}^{N:C}$	0.190	Maximum Microalgal N:C cellular quota	g N (g C)^{-1}
$Q_{min}^{Si:C}$	0.090	Minimum Microalgal Si:C cellular quota	g Si (g C)^{-1}
$\xi^{Si:N}$	3.8	Dumping factor for Maximum Si:C cellular quota	dimensionless
β	10.0	Shape parameter for function γ	dimensionless
n	0.4	Shape parameter for function A_{lim}	dimensionless
k_3	0.132	Half-saturation constant for function γ	g N (g C)^{-1}
Initial Conditions			
$[\text{N}]_0$	43.0	Dissolved nitrogen concentration	$\mu\text{M [N]}$
$[\text{Si}]_0$	65.0	Silicate concentration	$\mu\text{M [Si]}$
P_0^C	53.6	Microalgal carbon biomass	$\mu\text{M C}$
P_0^{Chl}	7.14	Microalgal chlorophyll- <i>a</i> biomass	$\mu\text{g Chl l}^{-1}$
P_0^N	4.41	Microalgal organic nitrogen biomass	$\mu\text{M N}$
P_0^{Si}	6.4	Microalgal biogenic silica	$\mu\text{M Si}$

Model parameters were calculated over the average results of the three experiments using the multidimensional fitting method (*Downhill Simplex*) described by Nelder and Mead [1965]. The maximum carbon-specific light-saturated photosynthetic rate was taken from the experimental data described in the section 2.2.1 (see figure 2.2) and the maximum C-specific nutrient uptake rates were adjusted by $A_{max}^{N:C} = f_{C_{max}} Q_{max}^{N:C}$ and $A_{max}^{Si:C} = f_{C_{max}} Q_{max}^{Si:C}$ to keep the maximum uptake of nutrients in accordance with the maximum carbon assimilation rate. The model equations were integrated by a Fortran driver adapted from the classical fifth-order Runge-Kutta method with a Cash-Karp adaptive step-size scheme². Table 2.4 summa-

²Fortran algorithms for ODE integration can be found on <http://www.netlib.org>, including the original

rizes the model parameters found by the multidimensional fitting procedure and the initial conditions used in the model integration. The minimum and maximum nitrogen-to-carbon quotas agree well with observed values commonly found for Antarctic sea ice microalgae and phytoplankton [e.g. Nelson *et al.* 1989, Garrison and Close 1993, Kristiansen *et al.* 1992], as well as the Si:C quotas [e.g. Sommer 1991, Nelson and Tréguer 1992]. The half-saturation constant for nutrient uptake (k_N and k_{Si}) are also in the range of values reported for Antarctic diatoms [Nelson and Tréguer 1992, Kristiansen *et al.* 1992]. However, k_{Si} is considerably lower than previously values found by Jacques [1983] ($\approx 12 \mu\text{M}$ [Si] for *Fragilariopsis kerguelensis*) and Sommer [1991] ($\approx 8 \mu\text{M}$ [Si] for *F. cylindrus*). Methodological difficulties in using mono-algal cultures can be responsible for the disagreement of values [Nelson and Tréguer 1992] and nutrient kinetic studies in sea ice are still necessary to give a better estimate of these parameters. Maximum chlorophyll-to-carbon ratio ($Q_{max}^{Chl:C}$) and the Chl-specific photosynthetic efficiency (α^{Chl}) are also in the range of reported values for sea ice microalgae [e.g. Rivkin and Putt 1987, Lizotte and Sullivan 1991; 1992, Thomas *et al.* 1992].

The model was integrated for 25 days with an adaptive stepsize. The results of the model integration compared with observations are shown in the Figures 2.6 and 2.7. Simulated microalgal carbon biomass and chlorophyll-*a* present the characteristic exponential growth (Fig. 2.6a) reaching values up to $700 \mu\text{M C}$ ($=8.4 \text{ mg C l}^{-1}$) and $140 \mu\text{g Chl l}^{-1}$, respectively, showing good agreement with observations. Nutrients are strongly depleted after 11 days (Fig. 2.6b) and completely exhausted after 14 days. Silicate becomes limited at day 11, followed by dissolved nitrogen two days later. The transition between dissolved nutrient limitation and cellular nutrient quota limitation can be better delineated by observing the time evolution of cellular nutrient quotas (Fig. 2.7a). The microalgal cells are apparently nutrient depleted at the beginning of the experiment, increasing their cellular quotas in 3-4 days. When silicate becomes limiting, the Si:C cellular quota starts to decrease, followed by the N:C quota. The exponentially decreasing rate of cellular nutrient pools are followed by a reduction in the growth rate approaching the stationary phase at day 20. The same behavior is also visible when analyzing the chlorophyll-to-carbon and the chlorophyll-to-nitrogen ratios (Fig. 2.7b), where the Chl:N ratio can be used as a proxy to identify the time when nitrogen

Runge-Kutta (RK45) with Fehlberg's method for timestep splitting. The driver used in this work was adapted from the RK45 described in Press *et al.* [1992].

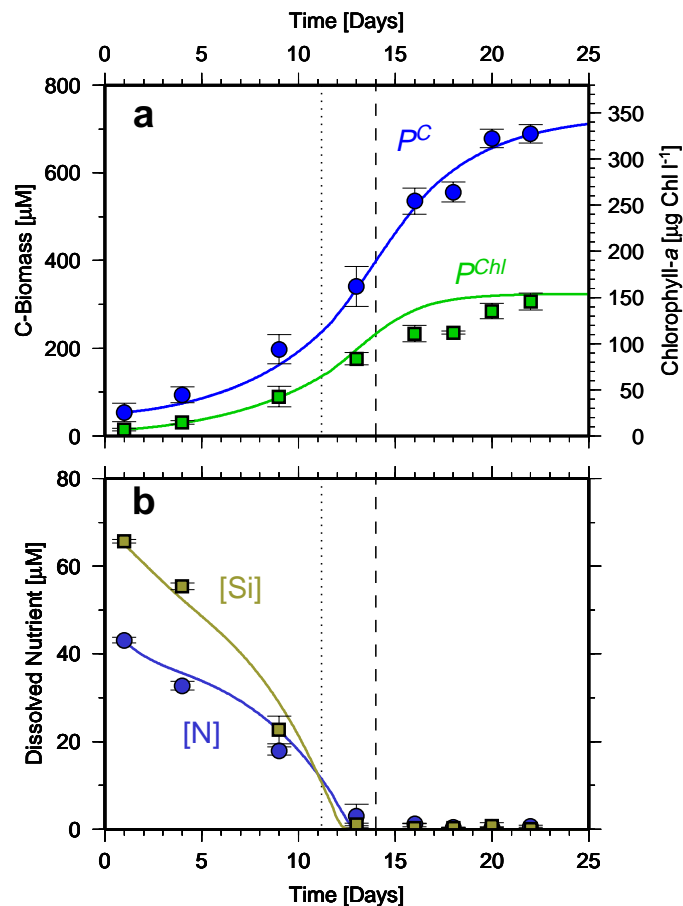


Figure 2.6: Model results (solid lines) and experimental data for (a) microalgal carbon biomass (circles) and chlorophyll-*a* (squares), and (b) dissolved nitrogen (circles) and silicate (squares). The dotted line indicate the time when dissolved nutrients become limited and the dashed line when both dissolved nutrients were completely exhausted. See text for explanation.

becomes limiting. It is important to note that after both dissolved nutrients were exhausted, microalgal biomass is still in exponential growth due to supply of nutrients from the cellular pools. This is the main advantage of Droop's quota model over typical Michaelis-Menten models [e.g. Fasham *et al.* 1990, Arrigo *et al.* 1991], showing that incorporation of carbon biomass can take place even when the medium are totally depleted of dissolved nutrients. However, the decrease in the chlorophyll-to-carbon ratio (Fig. 2.7b) suggested that microalgae also lost photosynthetic efficiency (due to the unbalance in the photoacclimation term in equation 2.12 - subsection 2.2.2). Such behavior can be simulated only by coupling the photoacclimation with nutrient co-limitation models. Cullen and Lewis [1988] demonstrated that first-order kinetic models with self-adapting mechanisms are essential to represent rapid responses of algal physiology to transient changes in the light and nutrient supply. The cellular nutritional status and the carbon assimilation change as a result of unbalanced growth,

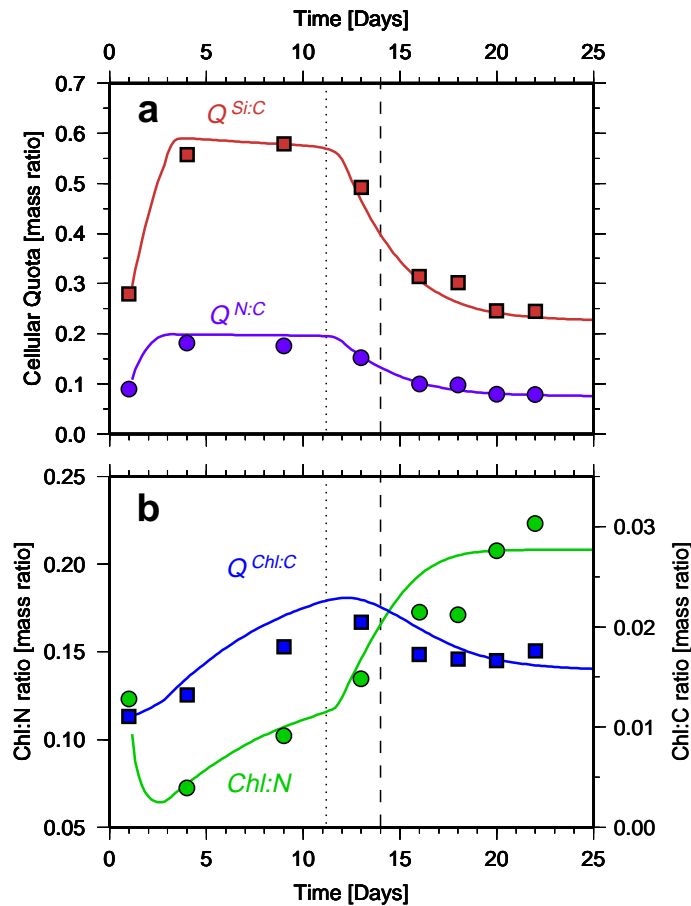


Figure 2.7: Model results (solid lines) and experimental data for (a) cellular N:C quota (circles) and Si:C quota (squares), and (b) chlorophyll-to-nitrogen (circles) and Chl-*a*:C ratios (squares). Dotted and dashed lines as in the Fig. 2.6.

but on much longer time scales than the light-harvesting complex. This fact suggests that self-adaptive models are better suited to represent realistic environmental conditions.

Unfortunately, the experiment data exclude heterotrophic protists and there was no information available about the total biomass of protozoa in the sea ice samples. To test the ability of the model to represent grazing, a simulation including a generic protozoa was conducted. Model parameters were maintained as described above and initial protozoa biomass was taken to be 1 % of microalgal C-biomass ($\approx 0.53 \mu\text{M C}$) with a cellular nitrogen concentration of $0.08 \mu\text{M N}$. The maximum ingestion and respiration rates were calculated using equations described in the subsection 2.2.4 with a mean protozoa body mass of $3500 \text{ pg C cell}^{-1}$, and optimum N:C ratio $\delta^{N:C}=0.176$, equivalent to the Redfield ratio 6.6 C:N.

The time evolution of microalgal biomass when grazing is included also shows an exponential growth following the availability of nutrients (Fig. 2.8a). However, a strong decrease in the microalgal carbon and chlorophyll-*a* concentrations is observed after nutrients are ex-

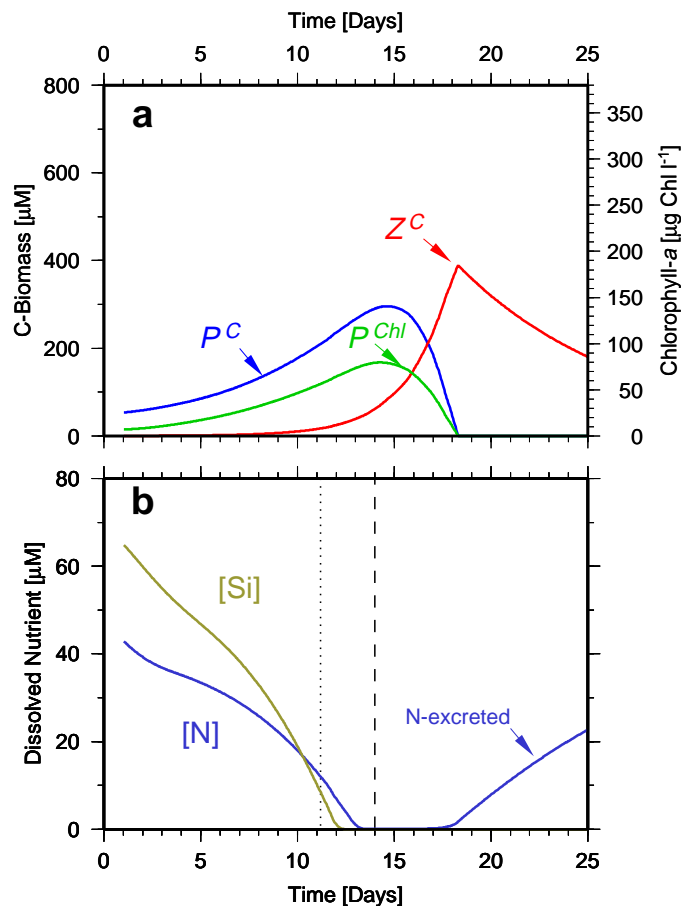


Figure 2.8: Model results including grazing. (a) microalgal carbon biomass (P^C), chlorophyll-*a* (P^{Chl}) and protozoa carbon biomass (Z^C) as indicated by the arrows. (b) dissolved nitrogen and silicate where the indicated fraction is excreted nitrogen.

hausted. In general, sea ice microalgae grow faster than heterotroph protists under optimal conditions, but growth conditions are unbalanced under limiting resources and the effect of grazing is noticeable [Garrison and Buck 1989]. Dissolved nutrients decrease exponentially accompanying the microalgal growth with a pronounced increment of excreted nitrogen after 20 days (Fig. 2.8b). However, silicate is already limiting and no further microalgal growth is evident.

The nutritional status of microalgae is not affected by grazing (compare Fig. 2.8a and Fig. 2.7). It is interesting to note that the nutritional status of protozoa, represented by $QZ^{N:C}$, is well correlated with the microalgae N:C quota ($Q^{N:C}$) due to the mechanism of selective N-excretion explained in the subsection 2.2.5. A strong signal in the nitrogen-to-carbon and nitrogen-to-chlorophyll ratio can be observed after day 22, when the few microalgal cells still alive begin to take up the excreted nitrogen (Fig. 2.9a).

The model has a relative complex design with a large number of parameters, but its ability

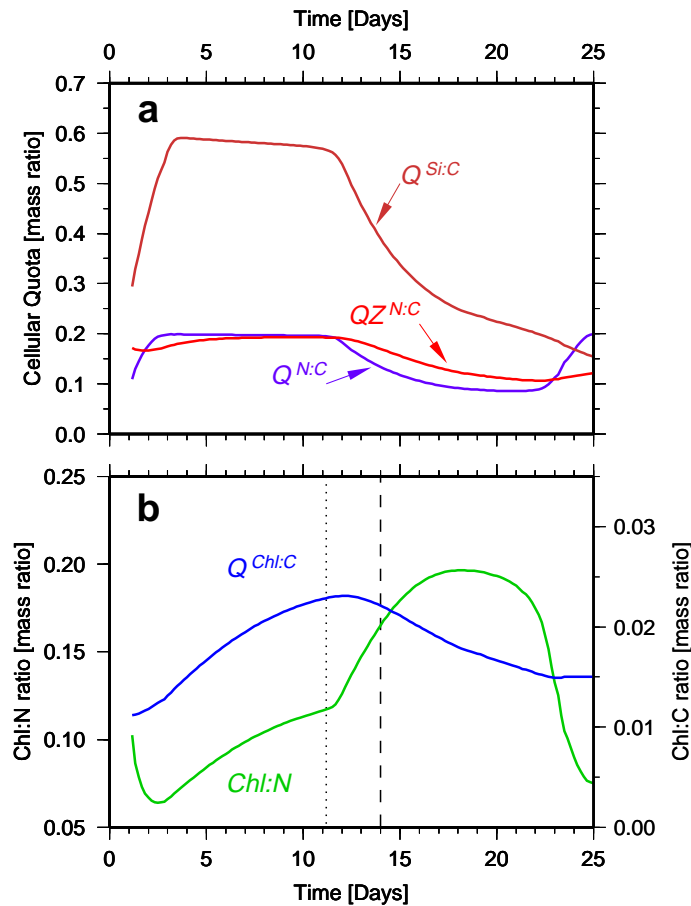


Figure 2.9: Model results with grazing for (a) microalgal cellular N:C ($Q^{N:C}$) and Si:C quotas ($Q^{Si:C}$), protozoa N:C ratio ($QZ^{N:C}$) and (b) chlorophyll-to-nitrogen and Chl-*a*:C ratios.

to represent mechanistic processes of self-adaptation in the model components is evident. The good agreement between model and observations suggests that the partial decoupling of carbon and dissolved nutrient fluxes, as well as the introduction of the photoacclimation model provide the essential information to simulate the time evolution of carbon biomass, chlorophyll-*a* and nutrients. Such an approach is strongly recommended to study sea ice microbial communities under realistic conditions.

The ability of the model to well represent nutrient dynamics in biological sea ice communities in an important aspect to be observed. Nutrient fluctuations within sea ice are much variable and difficult to interpret due to the complexity of the physical processes involved in the flux of brine and the time evolution of biological processes. Brine pockets are almost closed systems, where the ice permeability is controlled by the temperature and sea ice salinity (see Chapter 4). Therefore, dissolved nutrients in brine can be depleted very fast when primary production is high. Dieckmann *et al.* [1991b] showed that recycling of nitro-

gen takes place within the brine pockets, but dissolution and regeneration of silicate occurs probably at very low rates. These facts suggest that the cellular N- and Si-pools play a key role in the primary production when dissolved nutrients are completely exhausted. Since the biological model simulates the uptake of dissolved nutrients decoupled from the carbon production, it is possible to compute the maximal biomass production based only on the cellular N- and Si-pools.

2.4 Time Scales near the Model Stationary State

The biological model was designed to simulate the time evolution of biomass and nutrient fluxes under transient conditions in sea ice. A model stationary state is only achieved when silicate is completely exhausted in the brine, since N-recycling through grazing will contribute to the dissolved nitrogen pool. Nevertheless, some studies on the nutrient status in sea ice revealed that the contribution of grazing to remineralization of nutrients is low for most of interior communities in the pack-ice [Dieckmann *et al.* 1991b, Gleitz *et al.* 1995]. Assuming that microalgal growth is only governed by the availability of a finite nutrient concentration in brine without grazing, the stationary state is then achieved when [N] and [Si] are exhausted and the cellular pools reach their minimum ($Q^{N:C} \rightarrow Q_{min}^{N:C}$ and $Q^{Si:C} \rightarrow Q_{min}^{Si:C}$). Although the assumption of co-limiting nutrients, the final microalgal carbon biomass will depend only on one *most* limiting nutrient, which can be found by the relationship

$$P_{ss}^C = \begin{cases} P_0^C + \left[[N]_0 + P_0^C (Q_0^{N:C} - Q_{min}^{N:C}) \right] / Q_{min}^{N:C} & \text{for N-limiting} \\ P_0^C + \left[[Si]_0 + P_0^C (Q_0^{Si:C} - Q_{min}^{Si:C}) \right] / Q_{min}^{Si:C} & \text{for Si-limiting} \end{cases} \quad (2.22)$$

where P_{ss}^C is the microalgal C-biomass concentration at the stationary state, P_0^C is the initial microalgal C-biomass, $[N]_0$ and $[Si]_0$ are initial dissolved nitrogen and silicate concentrations, $Q_0^{N:C}$ and $Q_0^{Si:C}$ are initial N:C and Si:C ratios, respectively.

A simplified version of the model near the stationary state can be used to assert the microalgal growth rates under small perturbations in the dissolved nutrients. When the dissolved and cellular nutrient pools are completely exhausted (growth rate is zero), how much time do microalgae need to return to the stationary state when a small quantity of nutrients (enough to fill up the cellular pools) is added to the system? This *recovering time* can be

computed for different boundary conditions to explain how environmental changes in the brine influence the rate of primary production.

Assuming one single most-limiting nutrient, as the case described by the Eq. (2.22), the model can be simplified to a system with three equations

$$\frac{d[E]}{dt} = -\frac{A^{E:C}}{Q^{E:C}} P^E \quad \frac{dP^C}{dt} = f_C P^C \quad \frac{dP^E}{dt} = \frac{A^{E:C}}{Q^{E:C}} P^E \quad (2.23)$$

where E represents the most limiting nutrient (N or Si), $A^{E:C}$ is the nutrient uptake function, $Q^{E:C}$ is the nutrient-to-carbon quota and P^E is the microalgal nutrient concentration.

The stationary state is determined when the time variation of all variables are zero (converging to the steady state of the system). For real and positive values of P^E , P^C and $Q^{E:C}$ under constant temperature and illumination, this condition is achieved in two steps: first, when the nutrient uptake rate $A^{E:C}$ equals zero, and second, when the cellular nutrient limitation forces f_C to zero by limiting the light-saturated photosynthetic rate (see Section 2.2.1). The nutrient uptake rate is zero when dissolved nutrient are completely exhausted (see Eqns. 2.15 and 2.16) and microalgal growth depends only on the cellular nutrient quota. Therefore, near the stationary state, the model can be reduced to one equation

$$\frac{dP^C}{dt} = f_C P^C \quad (2.24)$$

The application of the linear dynamic system analysis [Stoer and Burlisch 1979] permits the simplification of this equation near the stationary state. Substituting the steady state condition given by Eq. (2.22) in (2.24) and derivating the expression with respect to P^C , the resulting solution can be represented in terms of its *normal mode* eigenvector e_1 and the associated eigenvalue λ_1 . Any perturbation in the model will decay over time as a simple exponential function with a *time constant* equal to the inverse of the associated eigenvalue, $t_1 = 1/\lambda_1$, according to

$$t_1 = \frac{Q_{max}^{E:C} - Q_{min}^{E:C}}{f_C Q_{min}^{E:C}} \quad P^C = P_0^C e^{-t/t_1} \quad (2.25)$$

As the instantaneous C-specific photosynthetic rate depends on the illumination and temperature, the time constant t_1 can be plotted for a given range of boundary conditions.

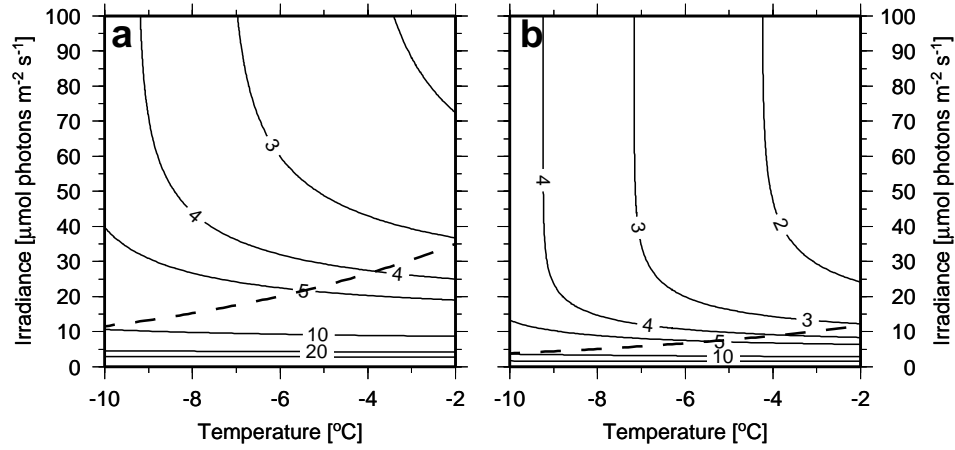


Figure 2.10: Time constant in days for the microalgal carbon accumulation under cellular nitrogen limitation and different temperature and incident light conditions. Isoclines are plotted in 1 day intervals for $t_1 < 5$ and every 10 days for $t_1 \geq 10$. The dashed line marks the point when light becomes saturated for a given temperature. Calculations were made with a Chl-*a*:C ratio of (a) 0.010 and (b) 0.03 $\mu\text{g Chl } (\mu\text{g C})^{-1}$.

When nitrogen is the most limiting nutrient, the time constant ranges from 2 up to 20 days depending on the temperature and available light to the photosynthesis. The chlorophyll-to-carbon ratio has a major impact on t_1 because the photosynthetic efficiency depends on the Chl:C ratio (see section 2.2.2). Increasing the Chl:C ratio from 0.01 $\mu\text{g Chl } (\mu\text{g C})^{-1}$ (Fig. 2.10a) to 0.03 $\mu\text{g Chl } (\mu\text{g C})^{-1}$ (Fig. 2.10b) produces significant changes in t_1 for light levels below the saturation point. The same behavior is observed when silicate is the most limiting nutrient, with the time constant varying from 6-7 days up to 50 days (Fig. 2.11). This is consistent with the fact that the maximum silicon-to-carbon quota ($Q_{max}^{Si:C}$) is ≈ 4 times greater than the nitrogen-to-carbon quota (given by the model parameter $\xi^{Si:N}$). However, if co-limitation is introduced and nitrogen is also a limiting nutrient, the time constant should decrease at a rate proportional to $\xi^{Si:N} Q^{N:C}$.

Since temperature has a direct effect on the light-saturated photosynthetic rate, its decrease causes a loss in the photosynthetic efficiency. The dashed lines in the Figs. 2.10 and 2.11 marks the point when light becomes saturating. It means that independent of an increase in light, the time constant is invariant. As expected, for a low chlorophyll-to-carbon ratio (0.01 $\mu\text{g Chl } (\mu\text{g C})^{-1}$), this light-saturation level is $2\times$ greater than for a chlorophyll-to-carbon ratio of 0.03 $\mu\text{g Chl } (\mu\text{g C})^{-1}$, with saturation levels varying between 18 $\mu\text{mol photons m}^{-2} \text{ s}^{-1}$ at -2°C to as low as 5 $\mu\text{mol photons m}^{-2} \text{ s}^{-1}$ at -10°C . Considering that in sea ice temperature and light profiles are inversely proportional in the vertical direction

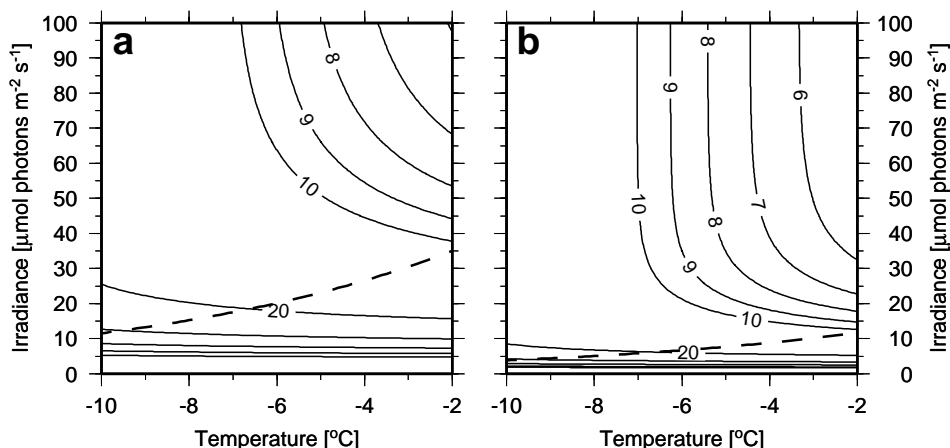


Figure 2.11: Time constant in days for the microalgal carbon accumulation under cellular silicon limitation and different temperature and incident light conditions. Isolines are plotted in intervals of 1 day for $t_1 < 10$ and every 10 days for $t_1 \geq 10$. The dashed line marks the point when light becomes saturated for a given temperature. Calculations were made with a Chl-*a*:C ratio of (a) 0.010 and (b) $0.03 \mu\text{g Chl } (\mu\text{g C})^{-1}$.

(lower temperatures and higher light at the top and higher temperatures with lower light at the bottom), the primary production of sea ice microalgae is always under a certain degree of limitation, either by temperature or by light.

In the next chapters, a bio-optical and a thermodynamic sea ice model are described to simulate the realistic conditions within sea ice. Coupling these models with the biological sea ice model will permit the investigation of how environmental conditions (temperature, light, nutrients and also grazing) impact the primary production of sea ice communities.

Chapter 3

Modeling the Spectral Solar Radiation within Sea Ice

Sea ice microalgal communities experience extensive fluctuating environmental conditions, which have a profound impact on the photosynthetic rate and algal growth, as demonstrated in the Chapter 2. Since photosynthesis depends on light, shifts in the solar radiation that penetrates sea ice will have a strong impact on the associated microalgal primary production. The solar radiation affects not only the biological processes, but also the sea ice thermodynamics, since absorption of shortwave radiation promotes internal heating becoming an important term in the sea ice heat budget.

The downward spectral solar radiation reaching the surface is the result of the attenuation of extraterrestrial solar irradiance by atmospheric constituents (e.g. ozone, oxygen, water vapor, aerosols and clouds) and by optical processes (Rayleigh scattering). Figure 3.1 shows a schematic representation of all important processes involved in light attenuation in the atmosphere and within sea ice. In this chapter, a solar spectral model adapted from Gregg and Carder [1990] and Bird and Riordan [1986] to Antarctic atmospheres is coupled to a bio-optical model in order to simulate the effects of the solar radiation in the sea ice thermodynamics and biological production.

3.1 The Incoming Solar Radiation

The model is an analytical representation of spectral attenuation processes of solar radiation in the atmosphere, based on the work of Gregg and Carder [1990] and Bird and Riordan [1986]. It estimates the incoming solar radiation in the shortwave spectrum (from 290 to 4000 nm [Iqbal 1983]) for a given solar zenith angle θ (Fig. 3.1). The determination of θ is based on the low precision astronomic formulas of Meeus [Astronomical Almanac 1998] for

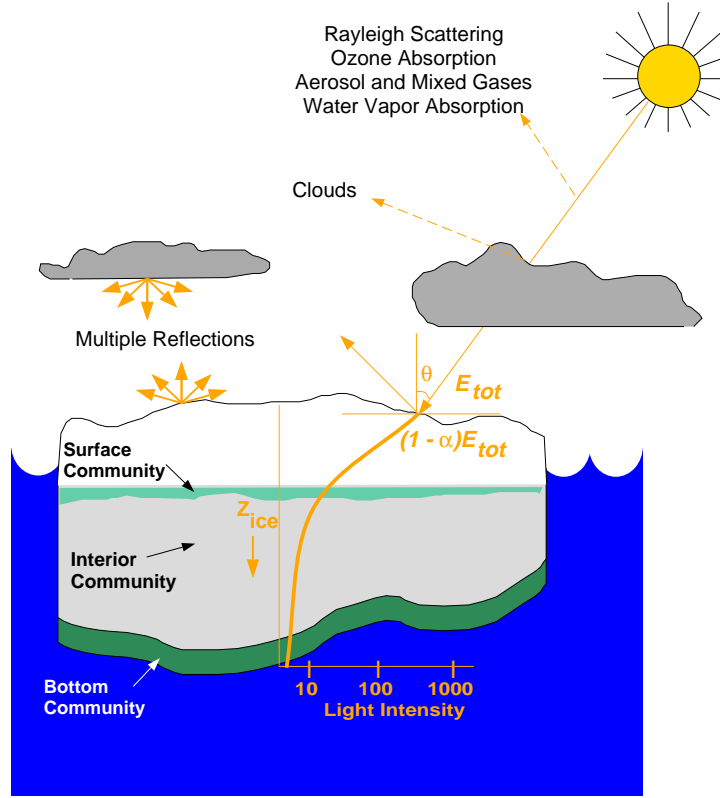


Figure 3.1: Schematic representation of light transmission through the atmosphere and sea ice, with emphasis in the atmospheric attenuation processes and the exponentially decay of light within sea ice.

a given Earth location (latitude and longitude) and the Greenwich Mean Time (GMT) given in Epoch Seconds¹.

For the biological model described in the Chapter 2, the solar radiation is represented as the integrated PAR (Photosynthetic Available Radiation), defined as

$$\text{PAR} = \frac{1 \times 10^{-3}}{h c \mathcal{N}} \int_{400}^{700} \lambda E_{tot}(\lambda) d\lambda \quad (3.1)$$

where h is the Planck's constant (6.63×10^{-34} J s), c is the speed of light (2.998×10^8 m s⁻¹), \mathcal{N} is the Avogadro number (6.022×10^{23} mol⁻¹), E_{tot} is the global incoming solar radiation in W m⁻² nm⁻¹ and λ is the wavelength in nm. The coefficient 1×10^{-3} is used to convert the integral to $\mu\text{mol photons m}^{-2} \text{s}^{-1}$. For the thermodynamic sea ice model (Chap. 4), the shortwave solar radiation F_{SW} is given in W m⁻² and determined by

$$F_{SW} = \int_{290}^{4000} E_{tot}(\lambda) d\lambda \quad (3.2)$$

¹Epoch Seconds is the number of seconds since 01.01.1970 00^{UT}.

The global incoming solar radiation is given by the sum of two main spectral components $E_{tot}(\lambda) = E_{dd}(\lambda) + E_{ds}(\lambda)$, where E_{dd} is the direct and E_{ds} is the diffuse solar radiation

$$E_{dd}(\lambda) = F_0(\lambda) \cos \theta T_r(\lambda) T_a(\lambda) T_{oz}(\lambda) T_u(\lambda) T_w(\lambda) \quad (3.3)$$

$$E_{ds}(\lambda) = I_r(\lambda) + I_a(\lambda) + I_g(\lambda) \quad (3.4)$$

3.1.1 The Direct Component of Solar Radiation

The direct component E_{dd} is calculated by multiplying the mean extraterrestrial irradiance, F_0 , corrected for orbital eccentricity and earth-sun orbital distance [Spencer 1971], for the solar zenith angle θ and the atmospherical transmittance T_r , T_a , T_{oz} , T_u , T_w after molecular Rayleigh scattering, aerosol scattering and absorption, ozone absorption, oxygen absorption and water vapor absorption, respectively. The diffuse component E_{ds} is given by the sum of diffuse Rayleigh multiple-scattering, I_r , aerosol scattering component, I_a and multiple reflections between ground and air, I_g .

The atmospherical transmittance for all components depends on the relationship between θ and the atmospherical pathlength, M , (or air mass) [Kasten 1966], written as

$$M(\theta) = \left[\cos \theta + 0.15 (93.885 - \theta)^{-1.253} \right]^{-1} \quad (3.5)$$

For oxygen absorption and Rayleigh scattering, a surface pressure-corrected air mass is needed and given by

$$M_{corr}(\theta) = M \frac{P_{surf}}{P_0} \quad (3.6)$$

where P_0 is the reference standard pressure (=1013 mb) and P_{surf} is the surface air pressure. In the case of ozone absorption, a specific-ozone air mass is used [Paltridge and Platt 1976], defined as

$$M_{oz}(\theta) = \frac{1.0035}{(\cos^2 \theta + 0.007)^{0.5}} \quad (3.7)$$

Finally, the atmosphere transmittance is determined by the contribution of each atmospherical component using the following equations:

$$\text{Rayleigh Scattering} \quad T_r(\lambda) = \exp \left\{ -M_{corr}(\theta) / \left[\lambda^4 \left(115.6406 - \frac{1.335}{\lambda^2} \right) \right] \right\} \quad (3.8)$$

$$\begin{array}{ll} \text{Aerosol Scattering} & \\ \text{and Absorption} & T_a(\lambda) = \exp \left[-\dot{\beta} \lambda^{-\dot{\alpha}} M(\theta) \right] \end{array} \quad (3.9)$$

$$\begin{array}{ll} \text{Ozone Absorption} & T_{oz}(\lambda) = \exp \left[-k_{ozo}(\lambda) H_{oz} M_{oz}(\theta) \right] \end{array} \quad (3.10)$$

$$\begin{array}{ll} \text{Oxygen Absorption} & T_u(\lambda) = \exp \left\{ \frac{-1.41 k_{oxy}(\lambda) M_{corr}(\theta)}{[1 + 118.3 k_{oxy}(\lambda) M_{corr}(\theta)]^{0.45}} \right\} \end{array} \quad (3.11)$$

$$\begin{array}{ll} \text{Water Vapor} & \\ \text{Absorption} & T_w(\lambda) = \exp \left\{ \frac{-0.2385 k_{wat}(\lambda) W_{path} M(\theta)}{[1 + 20.07 k_{wat}(\lambda) W_{path} M(\theta)]^{0.45}} \right\} \end{array} \quad (3.12)$$

where atmospheric absorption coefficients are k_{ozo} , k_{oxy} , k_{wat} for ozone, oxygen and water vapor, respectively, taken from Iqbal [1983], W_{path} is the precipitable water in a vertical atmospheric path (atm-cm) and H_{oz} is the ozone amount (atm-cm). The transmittance due to aerosol is determined by the turbidity coefficient $\dot{\beta}$ and the Angstrom exponent $\dot{\alpha}$ [Angström 1961].

Gregg and Carder [1990] suggested that aerosol and ozone are one of the most important constituents determining the light attenuation in the atmosphere. They determined that small oscillations in the atmospheric aerosol and ozone concentrations affect up to 20% the global solar radiation reaching the Earth's surface. In the Southern Ocean, Herber *et al.* [1993] found that Antarctic aerosol have strong seasonal and latitudinal signals, with relatively small longitudinal variability. Also the ozone amount H_{oz} shows a similar pattern [Arrigo 1994], with 50% reduction in stratospheric O₃ concentrations in early spring and a strong latitudinal gradient.

The aerosol optical parameters $\dot{\beta}$ and $\dot{\alpha}$, the ozone amount H_{oz} , and the precipitable water path W_{path} are forcing fields obtained from climatological datasets as described in the appendix A.

Figure 3.2 shows the spectrum of the extraterrestrial solar radiation F_0 and the absorption coefficients for different atmospheric constituents between 300 to 700 nm. The solar radiation reaching the Earth surface at these wavelengths are of major biological importance [Kirk 1981].

3.1.2 The Diffuse Component of Solar Radiation

In Eq. 3.4, the diffuse solar radiation $E_{ds}(\lambda)$ is dependent on three components: I_r the diffuse part of Rayleigh scattering, I_a the diffuse radiation arising from aerosol scattering and I_g the diffuse contribution from multiple ground-air interactions, defined as

$$I_r(\lambda) = F_0(\lambda) \cos \theta [1 - T_r(\lambda)^{0.95}] 0.5 T_{aa}(\lambda) T_{oz}(\lambda) T_u(\lambda) T_w(\lambda) \quad (3.13)$$

$$I_a(\lambda) = F_0(\lambda) \cos \theta [1 - T_{as}(\lambda)] F_a(\theta) T_r(\lambda)^{1.5} T_{aa}(\lambda) T_{oz}(\lambda) T_u(\lambda) T_w(\lambda) \quad (3.14)$$

$$I_g(\lambda) = \frac{[E_{dd}(\lambda) + I_r(\lambda) + I_a(\lambda)] r_s(\lambda) r_g(\lambda)}{[1 - r_s(\lambda) r_g(\lambda)]} \quad (3.15)$$

where $F_a(\theta)$ is the forward-to-total scattering ratio of aerosol, $T_{aa}(\lambda)$ and $T_{as}(\lambda)$ are the transmittance after aerosol absorption (without scattering) and scattering (without absorption) [Bird and Riordan 1986]

$$T_{aa}(\lambda) = \exp[-(1 - \bar{\omega}_a) \tau_a M(\theta)] \quad (3.16)$$

$$T_{as}(\lambda) = \exp[-\bar{\omega}_a \tau_a M(\theta)] \quad (3.17)$$

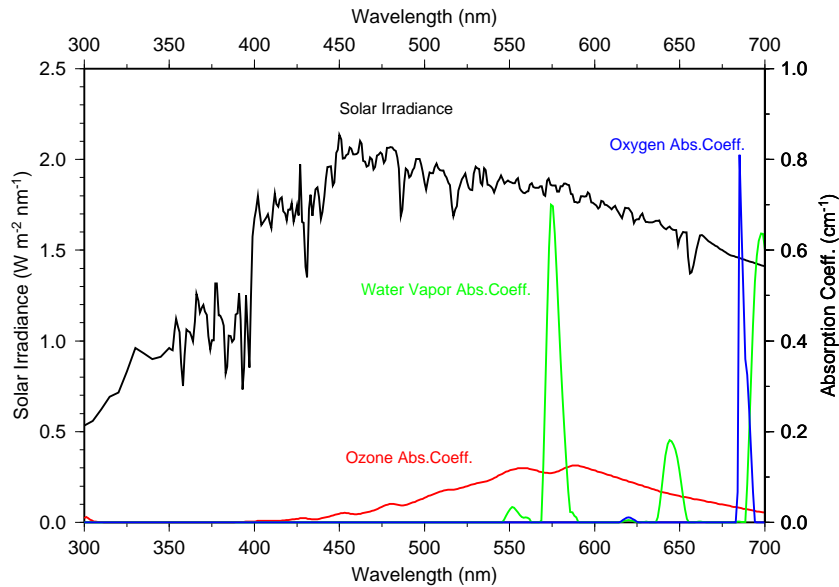


Figure 3.2: Spectrum of the extraterrestrial solar irradiance between 300 and 700 nm, and absorption coefficients of the main atmospheric constituents (ozone, water vapor and oxygen).

Three optical properties of aerosol are needed to calculate the transmittance above: the aerosol optical depth, given by $\tau_a(\lambda) = \beta \lambda^{-\alpha}$, the single-scattering albedo $\bar{\omega}_a$ and the aerosol forward-to-total scattering ratio $F_a(\theta)$. Gregg and Carder [1990] presented a reasonable approximation of these optical properties for marine conditions, based on the Navy aerosol model of Gathman [1983]. $F_a(\theta)$ is computed from the asymmetry parameter $\langle \cos \gamma \rangle$ based in the anisotropic scattering function of γ , following Tanre *et al.* [1979]

$$F_a(\theta) = 1 - 0.5 \exp[(B_1 + B_2 \cos \theta) \cos \theta] \quad (3.18)$$

$$B_1 = B_3 [1.459 + B_3 (0.1595 + 0.4129 B_3)] \quad (3.19)$$

$$B_2 = B_3 [0.0783 + B_3 (-0.3824 - 0.5874 B_3)] \quad (3.20)$$

$$B_3 = \ln(1 - \langle \cos \gamma \rangle) \quad (3.21)$$

$$\langle \cos \gamma \rangle = \begin{cases} 0.82 & : \alpha < 0 \\ -0.1417 \alpha + 0.82 & : 0 \leq \alpha \leq 1.2 \\ 0.65 & : \alpha > 1.2 \end{cases} \quad (3.22)$$

The single scattering albedo $\bar{\omega}_a$ depends on the relative humidity RH and the air mass type AM, which is set to 1 for the Antarctic pack-ice representing pure marine-aerosol conditions [Gregg and Carder 1990].

$$\bar{\omega}_a = (-0.0032 \text{ AM} + 0.972) \exp(3.06 \times 10^{-4} \text{ RH}) \quad (3.23)$$

The reflectivity of the surface, $r_g(\lambda)$, and sky, $r_s(\lambda)$, contributed to the diffuse solar radiation through multiple light reflections between ground and sky. Bird and Riordan [1986] parameterized the sky reflectivity based on the atmospheric transmittance for a standard air mass $M'(\theta)=1.8$ ($\approx \theta = 56.3^\circ$), given by

$$r_s(\lambda) = T'_{aa}(\lambda) T'_{oz}(\lambda) T'_u(\lambda) T'_w(\lambda) \{ [1 - T'_r(\lambda)] 0.5 + [1 + F'_a(\theta)] T'_r(\lambda) [1 - T'_{as}(\lambda)] \} \quad (3.24)$$

where the prime terms (') are atmospheric transmittance evaluated for $M'(\theta)$.

The surface reflectivity $r_g(\lambda)$ depends on the ice cover and the presence or not of snow

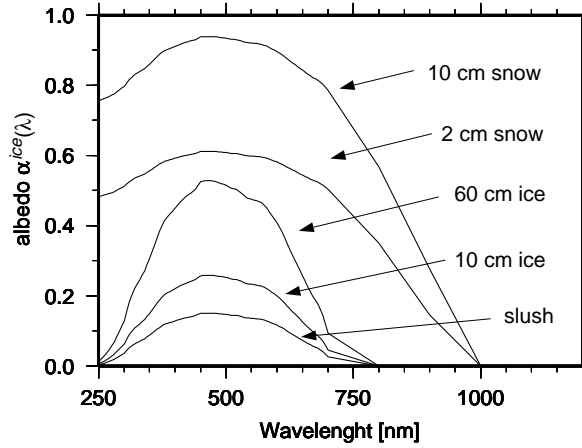


Figure 3.3: The spectral albedo of sea ice $\alpha^{ice}(\lambda)$ for different ice thickness and snow cover, following the parameterization of Bohren [1983] and Wiscombe and Warren [1980].

overlying the sea ice. It is related to the ice and water albedo by

$$r_g(\lambda) = \alpha^{ice}(\lambda) A_{ice} + \alpha^{water}(\lambda) (1 - A_{ice}) \quad (3.25)$$

where A_{ice} is the ice concentration and the spectral albedo of open water α^{water} is taken to be fixed on 0.15 [Kirk 1994]. For the sea ice, the spectral albedo α^{ice} depends on the ice thickness and the snow cover, following the parameterization of Bohren [1983] and Wiscombe and Warren [1980] (Fig. 3.3).

The sea ice concentration A_{ice} and the relative humidity RH are obtained from forcing fields as described in Appendix A.

3.2 The Bio-optical Sea Ice Model

The spectral incoming solar radiation $E_{tot}(\lambda)$ that reaches the ice surface is corrected for the effect of cloud attenuation using the empirical formula from [Laevastu 1960]

$$E_{tot}(0^+, \lambda) = E_{tot}(\lambda) (1 - 0.6 CL^3) \quad (3.26)$$

where $E_{tot}(0^+, \lambda)$ is the spectral solar radiation just above the ice (or snow) surface and CL is the cloud cover in tenths.

The determination of the spectral solar light at different sea ice vertical levels is based on Beer's Law, which assumes that the light is exponentially attenuated when transmitted

through ice layers with a specific spectral extinction coefficient $K_{ext}(\lambda)$. Physically, Beer's Law is valid only for optically thick medium. Since the bulk extinction coefficient for pure ice ranges from 0.8 to 1.5 m^{-1} [Perovich 1990], large optical thickness are found at ice depths ≥ 30 cm. On the other hand, snow has a bulk extinction coefficient $10\times$ greater than ice (around 7-10 m^{-1}) and a few centimeters of snow overlying sea ice is enough to produce the necessary condition to apply Beer's Law [Bohren 1983].

The solar radiation just below the ice or snow surface ($E_{tot}(0^-, \lambda)$) is defined as the portion of light that penetrates the surface

$$E_{tot}(0^-, \lambda) = E_{tot}(0^+, \lambda) (1 - \alpha^{ice}) \quad (3.27)$$

The specular reflectance at the surface is not explicitly considered since its effects are of secondary importance for the light transmission in sea ice [Bohren 1983].

The solar radiation at a particular wavelength λ that penetrates sea ice is exponentially attenuated within ice layers with thickness Δz and spectral extinction coefficient $K_{ext}(\lambda)$ ($=K_{ext}^{ice}$ for sea ice and $=K_{ext}^{snow}$ for snow), written as

$$E_{tot}(z + \Delta z, \lambda) = E_{tot}(z, \lambda) \exp[-K_{ext}(\lambda) \Delta z] \quad (3.28)$$

For snow layers, the extinction coefficient $K_{ext}^{snow}(\lambda)$ is taken from Bohren [1983] and depends on the snow density ρ_{snow} and the snow grain diameter d_s

$$K_{ext}^{snow}(\lambda) = 0.845 \frac{\rho_{snow}}{\rho_i} \left[\frac{\kappa_i(\lambda)}{d_s} \right]^{0.5} \quad (3.29)$$

where ρ_i is the density of pure ice (0.917 g cm^{-3}), and $\kappa_i(\lambda)$ is the spectral absorption coefficient of pure ice taken from Warren [1984]. The snow density $\rho_{snow}=0.33$ g cm^{-3} is compatible with the thermodynamic model (see chapter 4) and the snow grain diameter d_s is set to 0.3 mm, which is considered to be representative for Antarctic snow [Sturm *et al.* 1998].

For sea ice layers, the spectral extinction coefficient is a little more complex because it depends on sea ice optical characteristics governed by the partial contribution of pure ice, air bubbles, brine pockets, and biological material (i.e. chlorophyll-*a*). Brandt and Warren

[1993] suggested that spectral K_{ext}^{ice} can be approximated by

$$K_{ext}^{ice}(\lambda) = K_{ext}^{chl}(\lambda) + [\sigma_{ice} + \kappa_{ice}(\lambda)] \sqrt{(1 - \tilde{\omega})(1 - \tilde{\omega}g)} \quad (3.30)$$

where σ_{ice} and $\kappa_{ice}(\lambda)$ are the scattering and absorption coefficients of clear sea ice, $\tilde{\omega} = \sigma_{ice}/[\sigma_{ice} + \kappa_{ice}(\lambda)]$ is the single-scattering albedo and g is the average cosine of the scattering angle (or *asymmetry factor*), set to 0.845 following Grenfell [1983]. Chlorophyll-*a* contributes to the light attenuation through its spectral extinction coefficient defined as

$$K_{ext}^{chl}(\lambda) = \frac{P^{Chl} \kappa_{chl}(\lambda)}{\bar{\mu}} \quad (3.31)$$

where P^{Chl} is the chlorophyll-*a* concentration in the sea ice layer, $\kappa_{chl}(\lambda)$ is the spectral absorption coefficient for chlorophyll-*a* taken from Arrigo *et al.* [1991] and $\bar{\mu} = 0.656$ is the average cosine for light extinction in sea ice [Grenfell 1983].

The term *clear sea ice* is used to define the matrix of pure ice with its embedded inclusions (brine pockets and air bubbles). In general, relationships between the physical and optical properties of sea ice are described by separately defining each component with specific absorption and scattering coefficients and averaged by their volume. These *inherent optical properties* or IOPs, are then used in Eq. (3.30) to calculate the spectral extinction coefficient for each sea ice layer. The absorption and scattering coefficients, σ_{ice} and κ_{ice} , are defined by

$$\kappa_{ice}(\lambda) = \kappa_i(\lambda) V_i + \kappa_b(\lambda) V_b \quad (3.32)$$

$$\sigma_{ice} = \sigma_b + \sigma_a \quad (3.33)$$

where V_i is the volume of pure ice ($= 1 - V_b - V_{air}$), V_b and V_{air} are the brine and air volumes, respectively, $\kappa_b(\lambda)$ is the spectral absorption coefficient of brine (assumed to be the same as clear sea water [Smith and Baker 1981]), σ_b and σ_a are the scattering coefficients for brine pockets and air bubbles. It is important to note that brine pockets contribute to scattering and absorption of sea ice, while air bubbles affect only the scattering coefficient, and pure ice, the absorption coefficient.

3.2.1 Brine Pockets

The scattering coefficient of brine pockets, σ_b , is a function of the pocket radius, r_b , and its size distribution, N_b . Light *et al.* [1998] developed an optical model for sea ice, where brine pockets were represented by an effective inclusion size of ellipsoidal shapes with a minor radius, r_b , and major radius, R_b . For optical purposes, this brine *ellipsoids* were converted to an equivalent sphere with radius r_{sp} preserving the surface to volume ratio. The surface area of an ellipsoidal brine pocket A_{bp} is given by

$$A_{bp} = 2 r_b R_b \left[\sqrt{1 - \varepsilon^2} + \frac{\sin^{-1} \varepsilon}{\varepsilon} \right] \quad (3.34)$$

where $\varepsilon = \sqrt{1 - r_b^2/R_b^2}$ is the pocket eccentricity². The pocket volume, V_{bp} , and the equivalent sphere radius, r_{sp} , are defined by

$$V_{bp} = \frac{4\pi}{3} r_b^2 R_b \quad r_{sp} = \frac{3 V_{bp}}{A_{bp}} \quad (3.35)$$

The size distribution of brine pockets and the relationship between brine volume and the pocket radius are taken from Light *et al.* [1998]

$$N_b = 1.3 \text{ mm}^{-1} \quad r_b = \left(\frac{3 V_b}{20\pi N_b} \right)^{1/3} \quad R_b = 5.0 r_b \quad (3.36)$$

The contribution of brine pockets to the clear sea ice scattering coefficient is written as

$$\sigma_b = Q_{sca}^{br} \pi r_{sp}^2 N_b \quad (3.37)$$

where Q_{sca}^{br} is the scattering efficiency of brine pockets which is the ratio of the scattering cross section area of a particle to its geometric cross section area. Its value converges to ≈ 2 [Bohren and Gilra 1979] since brine pockets are much larger than the modeled wavelengths.

²The formulas for the surface to volume ratio between an ellipsoid and a sphere can be found at <http://mathworld.wolfram.com>

3.2.2 Air Bubbles

The scattering coefficient of air bubbles, σ_a , is obtained from the scattering efficiency of an air bubble ($Q_{sca}^{air} = 2$ similar to Q_{sca}^{br}) and the size distribution of air bubbles in ice, $N_a(r)$, written as

$$\sigma_a = \int_{r_{min}}^{r_{max}} Q_{sca}^{air} \pi r_a^2 N_a(r) dr \quad (3.38)$$

Grenfell [1983] found that the size distribution of air bubbles with radius r_a in sea ice can be approximated by

$$N_a(r) = N_0 r_a^{-1.24} \quad (3.39)$$

with upper and lower limits between $r_a = 2$ and 0.1 mm, and $N_0 = V_{air}/10.3$. The air volume V_{air} is set to 15 ppt for compatibility to the thermodynamic sea ice model (see Chapter 4, Section 4.1). The size distribution given by equation 3.39 is calculated and substituted in 3.38 to find the contribution of air bubbles in the scattering coefficient for clear sea ice.

Solid salts also contribute to scattering in sea ice, but Light [1995] showed that this contribution is relevant only at temperatures below the eutectic point ($\leq -22^\circ\text{C}$), when brine pockets freezes almost completely. However, such temperatures are unusual in Antarctic sea ice because the insulation effects of snow during the cold winter and therefore, the contribution of solid salts is not considered in the model.

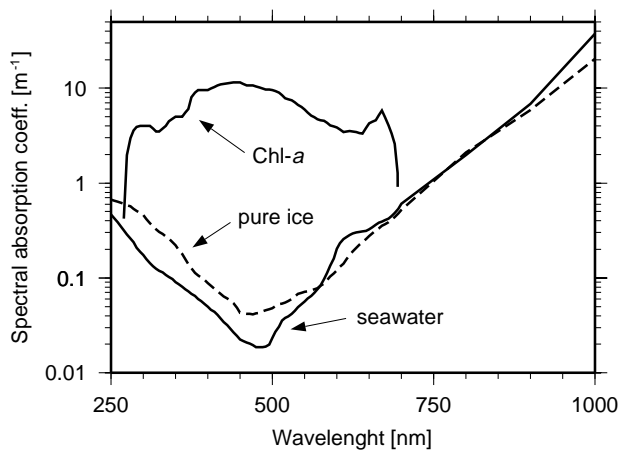


Figure 3.4: Absorption coefficients for pure ice, brine (equivalent to seawater), and chlorophyll-*a* between 250 and 1000 nm wavelengths.

The optical properties of each sea ice layer are calculated from the simulated values of brine volume, air volume and the chlorophyll-*a* concentration, in order to produce a vertical profile of the spectral solar radiation within sea ice. Although the absorption coefficients

of brine and pure ice are similar, the chlorophyll-*a* is approximately $100\times$ more effective in absorbing light in the visible spectrum (Fig. 3.4). Brine pockets and air bubbles are important components to scatter light, but the optical properties of a given sea ice layer is strongly dependent of its chlorophyll-*a* content.

3.3 Light Attenuation within the Sea Ice

To demonstrate the effect of the chlorophyll-*a* in the vertical attenuation of the solar radiation, two 40 cm-long sea ice profiles with the same brine volumes and air content but different chl-*a* distributions are used. The normalized vertical chlorophyll-*a* distributions were taken from two sea ice cores collected in the Weddell Sea during the Winter Weddell Gyre Study in 1992, one characterized by a sea ice bottom community and the other by a surface community. A maximum value of $4 \mu\text{g Chl-}a \text{ l}^{-1}$ was used to simulate the vertical distribution of chlorophyll-*a* based on the normalized profile. The PAR integrated solar radiation at the ice surface is $56 \mu\text{mol photons m}^{-2} \text{ s}^{-1}$. Figure 3.5 shows the ice profile with dominant chlorophyll-*a* concentration at the bottom layers.

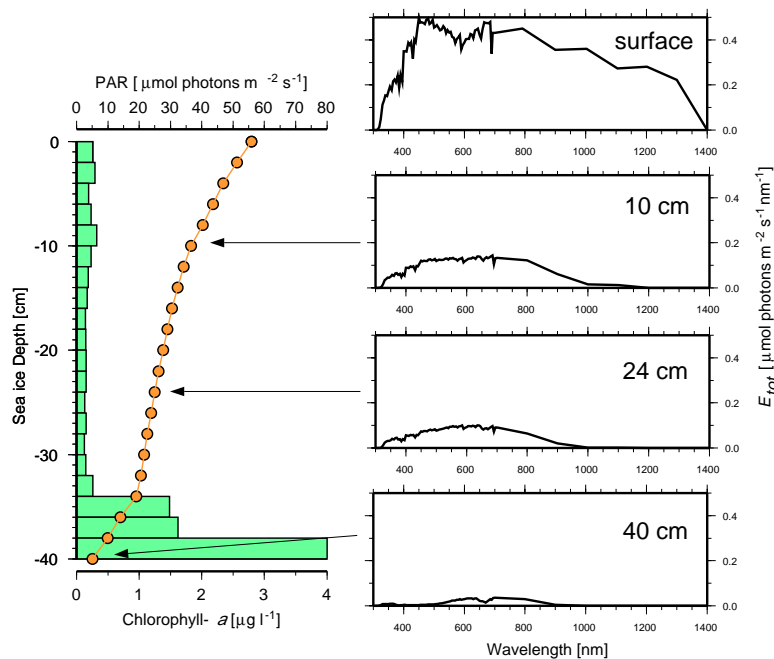


Figure 3.5: Simulated vertical distribution of light in sea ice with the dominant chl-*a* concentrations at the bottom-most layers (left) and the spectral solar radiation at indicated ice depths (right).

After 10 cm of ice, the light is attenuated to $\approx 40\%$ of its surface intensity and at 24 cm depth around 50%. However, from 34 to 40 cm depth ($\Delta z = 6$ cm), the light intensity

decreases from 20 to around $5 \mu\text{mol photons m}^{-2} \text{s}^{-1}$, showing an attenuation of 75 %. The spectral distribution of the light at different ice depths (Fig. 3.5 right) shows that the light extinction is wavelength selective. In the blue-green region of the spectrum (400-550 nm), chlorophyll-*a* dominates the light absorption, while in the upper layers, the dominant attenuation process is governed by clear sea ice.

When chlorophyll-*a* is concentrated at the top layers within sea ice (Fig. 3.6), most of the light is absorbed in the first few centimeters, decreasing from 56 to $\approx 8 \mu\text{mol photons m}^{-2} \text{s}^{-1}$ at 10 cm depth (85 %). After 24 and 40 cm ice, the light drops to 3 and $1 \mu\text{mol photons m}^{-2} \text{s}^{-1}$, respectively, with clear spectral signatures of attenuation due to chl-*a* (Fig. 3.6 right).

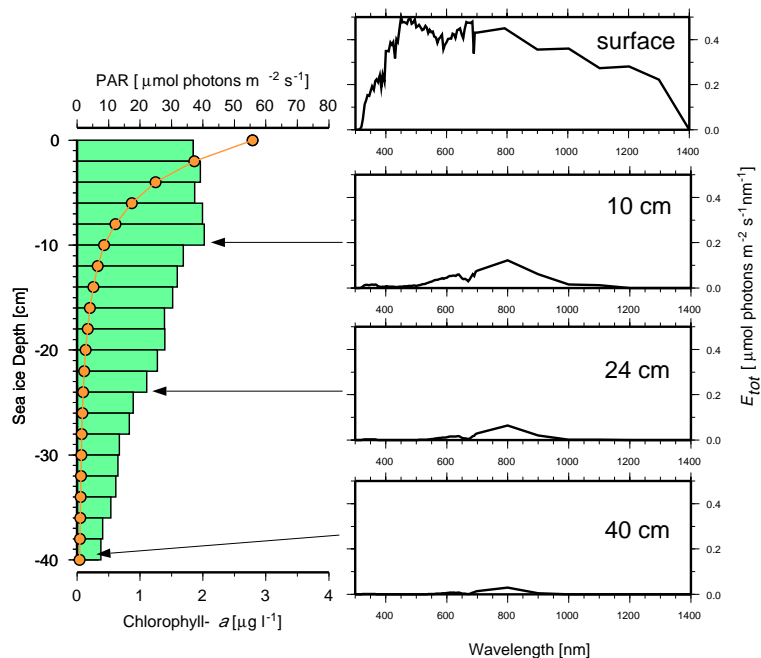


Figure 3.6: Simulated vertical distribution of light in sea ice with the dominant chl-*a* concentrations at the topmost layers (left) and the spectral solar radiation at indicated ice depths (right).

The vertical distribution of chlorophyll-*a* plays a key role in defining the optical properties of sea ice. The availability of light to the interior and bottom ice assemblages depends on the chlorophyll-*a* concentrations at the top layers. The simulations above were based on values of chl-*a* content in sea ice that are commonly found in the Antarctic pack-ice, which suggests that ice floes with dominant surface communities (chl-*a* concentrated at the top layers) may impede the development of interior and bottom communities due to shadowing. The thickness and concentration of the accumulated chlorophyll-*a* in the surface layers are

not only controlled by the *in situ* biological activity, but also depends on the incorporation of microalgal in sea ice during the initial stages of ice formation. This aspect must be taken into account when modeling the sea ice primary production.

3.4 Seasonal Variations in the Photosynthetically Available Radiation over the Sea Ice

Based on the spectral bio-optical model described in this Chapter, it is possible to estimate the maximum level of solar radiation that reaches the sea ice surface and its regional distribution. As discussed above, the solar radiation available for photosynthesis (PAR) in sea ice depends on the attenuation processes in the atmosphere and the overlying snow for a given position and time, where the local solar noon is the time of the day when the solar elevation is at its maximum. Using daily sea ice concentration and snow thickness datasets derived from satellite observations, and the spatial distribution of the atmospheric constituents like ozone, aerosol, water vapor, relative humidity (see Appendix A), monthly means of the maximum photosynthetically available radiation (PAR) at the snow/ice interface were computed for the Weddell Sea (Fig. 3.7 and 3.8).

Figure 3.7 shows the monthly means of maximum PAR between May and October, the period where the lowest incoming solar radiation is expected. The dashed and dotted lines are the limits of the polar night and very low solar elevation angles ($\theta \geq 85^\circ$), indicating that the ice below these latitudes is completely in darkness. Although between May and July most of the ice does not receive enough light to sustain biological production, a significant part of the marginal ice zone is exposed to maximum solar radiation levels between 40 and 150 $\mu\text{mol photons m}^{-2} \text{ s}^{-1}$. In August, the area of sea ice in darkness decreases drastically, with the maximum PAR levels still at the marginal ice zone, increasing up to 500 $\mu\text{mol photons m}^{-2} \text{ s}^{-1}$ in September and October. Therefore, the most productive areas in the pack-ice are situated in a zonal area of approximately 250 Km wide at the boundary of the ice edge. Figure 3.8 shows the monthly means of maximum PAR between November and April, when the daily maximum solar zenith is always $< 85^\circ$ (equivalent to a solar elevation $> 5^\circ$).

The zonal area of 250 Km in the marginal ice zone showing a maximum PAR of 600 $\mu\text{mol photons m}^{-2} \text{ s}^{-1}$ is still well delineated in November. However, most parts of the pack-ice

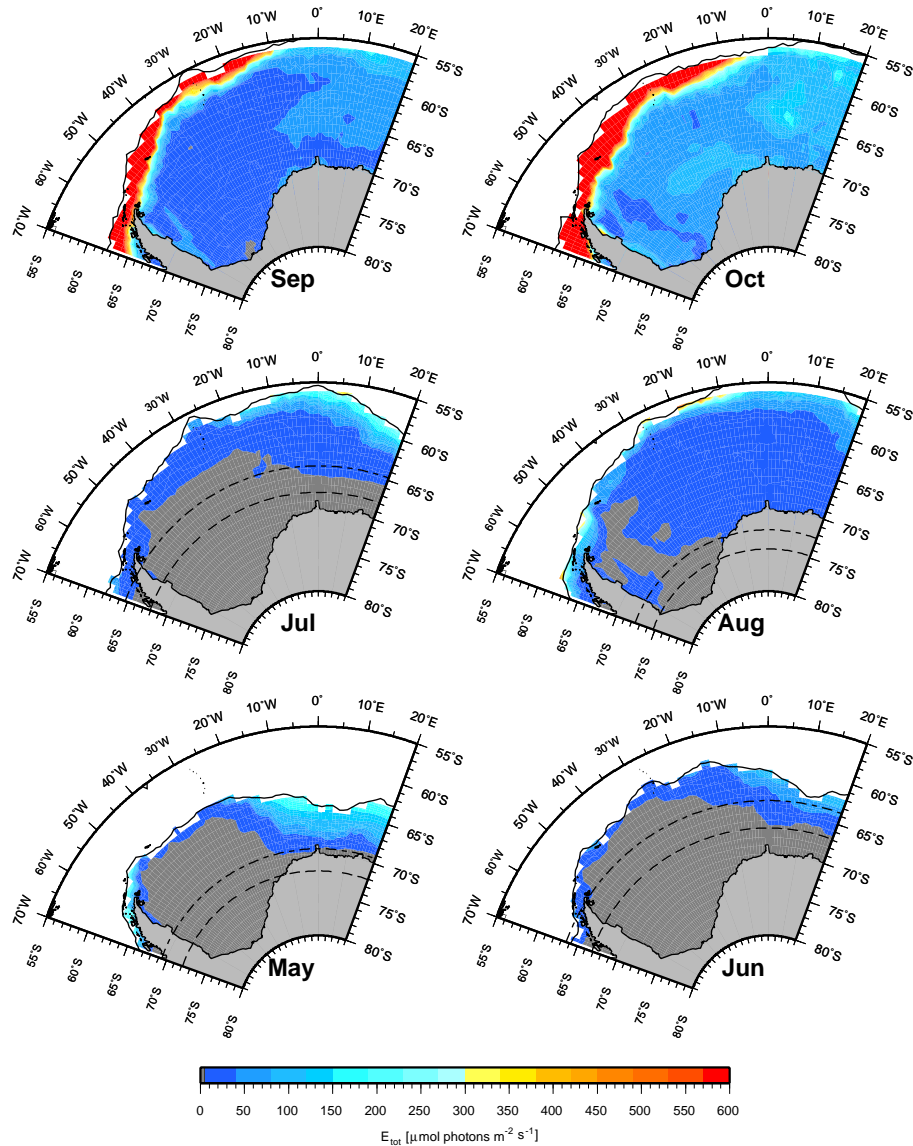


Figure 3.7: Monthly means of the maximum photosynthetically available radiation (PAR) at the snow/ice interface from May to October. The grey shade represents areas where the calculated solar radiation is below $5 \mu\text{mol photons m}^{-2} \text{s}^{-1}$. The dashed line is the zonal boundary of the polar night and the dotted line is the zonal boundary for solar zenith $\geq 85^\circ$.

are also exposed to maximum levels of solar radiation ranging from 100 to $300 \mu\text{mol photons m}^{-2} \text{s}^{-1}$. With the onset of the melting season in December, a general decrease in the snow cover and amelioration of incoming solar radiation close to the summer solstice improves the light conditions in the whole pack-ice, except in the central Weddell Sea. In this region, thicker snow cover still reduces the incoming solar radiation in 50% as compared to the eastern Weddell Sea. In January and February, the retreat of the ice is clearly noticeable and combined effects of residual snow cover and degradation of atmospheric conditions (e.g. cloud cover) result in a decrease of the maximum solar radiation levels in the central Weddell

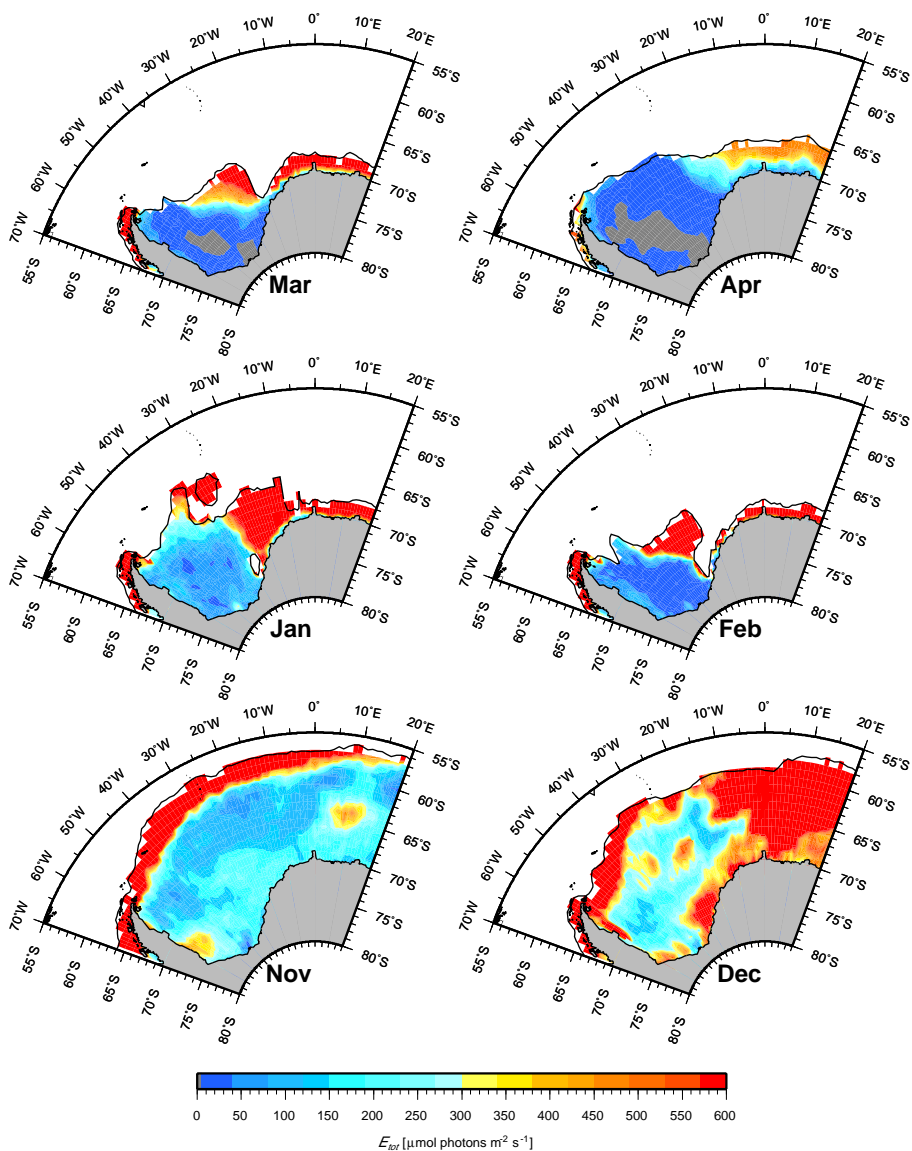


Figure 3.8: Monthly means of the maximum photosynthetically available radiation (PAR) at the snow/ice interface from November to April. The grey shade represents areas where the calculated solar radiation is below $5 \mu\text{mol photons m}^{-2} \text{s}^{-1}$.

Sea. With the onset of sea ice growth season between March and April, parts of the pack-ice are already in darkness, although this pattern is mainly governed by light attenuation due to snow and clouds, and not due to the seasonal solar declination.

One weakness in the modern sea ice primary production estimates is that only the months between October and April are taken into account. However, it was shown that a 250 Km wide area close to the ice edge is always exposed to significant levels of solar radiation, allowing a certain degree of biological activity. Although this area is considerable small when compared with the total ice extent, its ecological significance can not be ignored. Many

studies in the marginal ice zone showed that the productivity of this area play a key role in the Antarctic trophic chain [Clarke and Ackley 1984, Kottmeier and Sullivan 1990, Lancelot *et al.* 1991b, Cota *et al.* 1992].

Chapter 4

The Thermodynamic Sea Ice Model

The Antarctic sea ice cover is one of the most important seasonal features in the Southern Ocean with significant effects on the heat flux and momentum transfer between ocean and atmosphere [Lange *et al.* 1989]. Thermodynamics and radiative transfer processes in sea ice regulate the heat flux, which in turn plays a key role in sea ice growth, thickening, melting and its zonal extent. Based on the strong dependence of biological processes on light and temperature (see chapter 2), the internal structure of sea ice may play a key role in defining the main characteristics of microbial communities living within brine, since the vertical distribution of temperature, nutrients and optical properties result from physical processes during ice formation and growth.

The number of sea ice models developed in the last few years have increased considerably, in part due to the concerns about the effects of thermodynamic sea ice processes in a more global “climate change” framework. In a recent review about the formation and decay of sea ice [Wadhams 2000], two modeling studies were considered of special relevance: the one-dimensional thermodynamic sea ice model of Maykut and Untersteiner [1971], who presented a numerical method to describe the heat conduction in sea ice including snow cover effects (albedo) and internal heating due to the penetration of solar radiation; and the ice growth/salt flux model of Eicken [1992], based on the formulations of Cox and Weeks [1988] to simulate salt and brine fluxes in sea ice.

Sea ice is a mixture of liquid brine, air bubbles, solid salts and ice crystals, where the heat conduction is influenced by both porosity (i.e. as a function of the air content) and by thermodynamic effects within the liquid brine phase. Since brine is composed of tiny pockets with concentrated salt solution with a specific freezing point in phase equilibrium with the surrounding ice, it acts as a thermal reservoir retarding sea ice heating or cooling. This resistance to temperature changes is a function of both ice bulk salinity and temperature

itself, and determinant in the vertical characterization of sea ice physical properties [Yen 1981]. To simulate the effect of sea ice physical processes in the biological community and its associated primary production, it is necessary to model ice thermodynamics with a vertical resolution at relevant scale of environmental changes in the brine channels, where sea ice microorganisms are living. Brine pockets dimensions range from micrometers to tenths of millimeters [Perovich and Gow 1991] with vertical variability in the order of centimeters. To simulate biological and physical processes at such small scales, a vertical high-resolution model is needed.

In this chapter, a one-dimensional thermodynamic sea ice model is presented, including the numerical scheme to resolve heat conduction in sea ice, as well as the incorporation and vertical repartition of nutrients and biological material in the ice matrix simulating brine fluxes. These processes play the central role in structuring sea ice microbial communities and have important effects on the associated primary production. The model is based on both numerical studies of Maykut and Untersteiner [1971] and Eicken [1992].

4.1 Modeling Sea Ice Thermodynamics

In the model, sea ice is an idealized infinite slab formed by horizontally homogeneous layers with or without snow on the top. Each layer has a discrete vertical resolution of 2 cm where energy fluxes (temperature and light) are calculated at interfaces and mass fluxes (salt, nutrients and biological material) are given at the center of each layer (staggered grid scheme). The vertical grid configuration is shown in the Figure 4.1. Heat conduction through the ice layers and ice growth are controlled by the energy balance fluxes at both atmospheric (also referred as *skin surface*) and oceanic interfaces, and the sea ice temperature profile is numerically determined by solving the one-dimensional heat conduction equation. Salt, nutrient, biological and bio-optical properties for each layer are then determined based upon changes in the vertical temperature gradient within sea ice. In the following subsections, mathematical details of the model are given with emphasis in thermodynamic ice growth and repartitioning processes that drive the incorporation and accumulation of biological material in the sea ice.

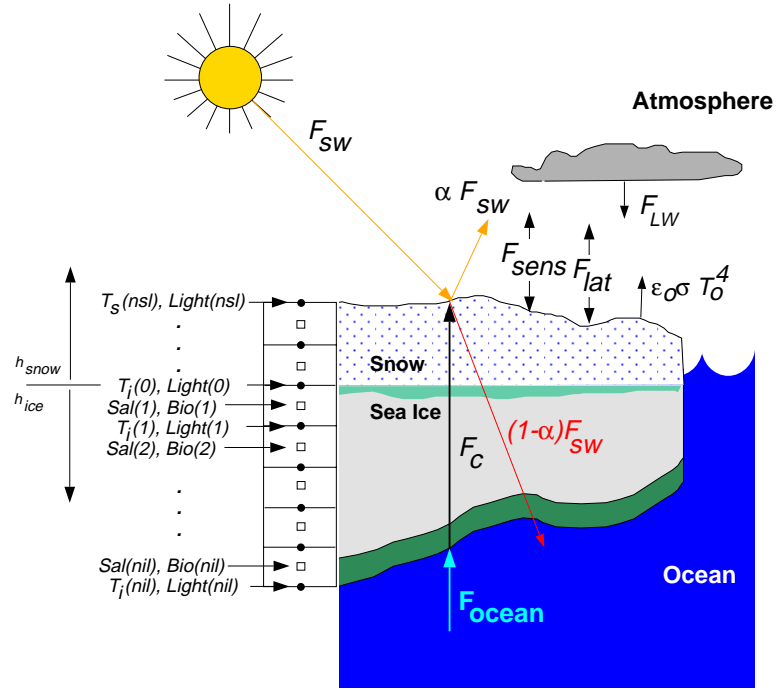


Figure 4.1: Schematic representation of important heat fluxes in sea ice with emphasis in the surface energy balance and placement of physical and biological variables in the model grid. See text for description of symbols.

4.1.1 Heat Fluxes at the Atmosphere-Ice Interface

At the uppermost ice boundary or *skin surface*, the heat flux is governed by the balance between the net energy flux F_{net} and the conductive heat flux at the topmost layer $F_c|_0$, with positive values pointing downward through the surface. In the absence of melting, the energy budget at the skin surface is given by

$$F_{net} = F_c|_0 \quad \text{with} \quad (4.1)$$

$$F_{net} = (1 - \alpha) F_{SW} + F_{LW}^\downarrow - F_{LW}^\uparrow + F_{sens} + F_{lat}$$

where the term $(1 - \alpha) F_{SW}$ represents the parcel of the incoming solar shortwave radiation F_{SW} that penetrates into the ice (α is the sea ice albedo), F_{LW}^\downarrow is the atmospheric downward longwave radiation and F_{LW}^\uparrow is the surface upward longwave thermal emission, F_{sens} and F_{lat} are the sensible and latent heat fluxes, respectively. The term $F_{LW}^\uparrow = \varepsilon_0 \sigma T_0^4$ on the right hand side of F_{net} contains the unknown surface *skin* temperature T_0 which differs from the air temperature. Equation 4.1 is therefore numerically solved for T_0 using the iterative

Newton-Raphson procedure [Press *et al.* 1992]. However, for T_0 at the melting point (273.15 K for snow and 273.05 K for sea ice) the imbalance in equation 4.1 causes melting of part of the top layer h_{si} according to

$$-\rho_0 L \frac{dh_{si}}{dt} = F_{net} + F_c |_0 \quad (4.2)$$

where ρ_0 is the density of the topmost layer and L is the heat of fusion of ice, respectively, and T_0 is constrained to the melting point. Some terms in the surface energy budget depend on the type of the topmost layer (snow or sea ice) which are described as follows.

Net shortwave radiation is defined as the parcel of the solar spectral shortwave radiation (from 290 to 4000 nm wavelength) that penetrates in the ice, written as

$$(1 - \alpha) F_{SW} = \int_{290}^{4000} [1 - \alpha(\lambda)] E_{tot}(\lambda) d\lambda \quad (4.3)$$

The sea ice spectral albedo $\alpha(\lambda)$ is a function of the surface type (snow or ice) and depends on the sea ice thickness and its optical characteristics, and $E_{tot}(\lambda)$ is the incoming solar spectral shortwave radiation given by the sum of the direct and diffuse solar radiation components ($E_{tot} = E_{dd} + E_{ds}$). The incoming solar radiation, as well as the optical properties of sea ice, are obtained coupling the thermodynamic model to a solar spectral atmospheric attenuation model and to a bio-optical sea ice model, described in detail in the Chapter 3.

Net longwave radiation is given by the balance between the downward longwave radiation F_{LW}^\downarrow and the surface upward thermal radiation F_{LW}^\uparrow , parameterized by Parkinson and Washington [1979] as

$$F_{LW}^\downarrow = \left\{ 1 - 0.261 \exp \left[-7.77 \times 10^{-4} (273.15 - T_{air})^2 \right] \right\} \times (1 + 0.275 \text{ CL}) \sigma T_{air}^4 \quad (4.4)$$

$$F_{LW}^\uparrow = \varepsilon_0 \sigma T_0^4 \quad (4.5)$$

where σ is the Stefan-Boltzmann constant ($5.67 \times 10^{-8} \text{ W m}^{-2} \text{ K}^{-4}$) and CL is the cloud cover (in tenths), T_{air} is the air temperature, ε_0 is the surface emissivity ($\varepsilon_{snow} = 0.99$ for snow and $\varepsilon_{ice} = 0.97$ for ice [Parkinson and Washington 1979]). The influence of the cloud

cover in the longwave radiation budget is a clear positive enhancement of the heat flux at the ice surface. This effect (second term on the right hand side of equation 4.4) is also called *greenhouse* and its relevance has been discussed by many authors [Liou *et al.* 1978, Brandt and Warren 1993, Ebert *et al.* 1995, Makshtas *et al.* 1998].

Sensible and Latent heat fluxes are important surface heat fluxes, with strong seasonal variability. Their parameterization follows the standard bulk aerodynamic formula [e.g. Ebert and Curry 1993]

$$F_{sens} = \rho_{air} c_{air} C_{sens} u (T_{air} - T_0) \quad (4.6)$$

where $\rho_{air} = 1.3 \text{ kg m}^{-3}$ is the air density, $c_{air} = 1006 \text{ J kg}^{-1} \text{ K}^{-1}$ is the specific heat of the air at constant pressure, $C_{sens} = 0.003$ is the sensible heat transfer coefficient, u is the wind speed in m s^{-1} , T_{air} and T_0 are the air and the skin surface temperature in Kelvin. The latent heat flux is parameterized for the Weddell Sea according to Eicken [1992]

$$F_{lat} = 0.25 F_{sens} \quad (4.7)$$

Heat conduction in the topmost layer is defined by the product between the temperature gradient and the thermal conductivity of the uppermost layer given by

$$F_c|_0 = k_0 \left. \frac{\partial T(z)}{\partial z} \right|_0 \quad (4.8)$$

where the thermal conductivity k_0 depends on the type of the topmost layer (k_{snow} for snow or k_i for ice). Details on determining k_0 are given in the next subsection.

4.1.2 Heat Conduction in Snow and Sea Ice Layers

The conduction of heat within snow and sea ice is calculated by solving the second-order heat diffusion equation defined as

$$\rho c \frac{\partial T}{\partial t} = \frac{\partial}{\partial z} \left(k \frac{\partial T}{\partial z} \right) + \frac{\partial \mathcal{F}_i(z)}{\partial z} \quad (4.9)$$

where ρ is the bulk density (ρ_{snow} for snow or ρ_{ice} for ice), c is the specific heat of ice, k is the thermal conductivity (k_{snow} for snow or k_i for ice) and T is the temperature in the layer with depth z . The last term on the right hand side is the divergence of irradiance [Zeebe *et al.* 1996], or the *internal heating source* caused by the absorption of shortwave radiation within sea ice and snow layers. In the model, the snow density is assumed to be constant ($\rho_{snow} = 0.33 \text{ g cm}^{-3}$) and its thermal conductivity [Yen 1969]

$$k_{snow} = 2.85 \rho_{snow}^2 \quad (4.10)$$

where k_{snow} , is given in $\text{W m}^{-1} \text{K}^{-1}$. The sea ice density ρ_{ice} and the thermal conductivity k_{ice} were given by [Cox and Weeks 1983; 1988]

$$\rho_{ice} = (1 - V_{air}) \frac{\rho_i F_1(T)}{F_1(T) - \rho_i S_i F_2(T)} \quad (4.11)$$

$$k_{ice} = (1 - V_{air} - V_b) k_i + V_b k_b \quad (4.12)$$

$$V_b = \frac{\rho_{ice} S_i}{F_1(T)} \quad (4.13)$$

where the V_{air} is the gas volume (defined as 15 ppt or 1.5%), V_b is the brine volume and ρ_i is the density of pure ice (0.917 g cm^{-3}). The sea ice bulk salinity S_i is time-dependent and calculated from the brine flux model detailed in the Section 4.2. The empirical polynomial functions $F_1(t)$ and $F_2(T)$ with coefficients given in the Table 4.1 [Leppäranta and Manninen 1988, Cox and Weeks 1983] are calculated as

$$F(T) = \alpha_0 + \alpha_1 T + \alpha_2 T^2 + \alpha_3 T^3 \quad (4.14)$$

The relationships between brine volume, sea ice bulk salinity, temperature and the brine salinity are shown in Fig. 4.2.

The thermal conductivity of pure ice k_i and pure brine k_b are given by

$$k_i = 418.6 \left[5.35 \times 10^{-3} - 2.568 \times 10^{-5} (T - 273.15) \right] \quad (4.15)$$

$$k_b = 418.6 \left[1.25 \times 10^{-3} + 3.0 \times 10^{-5} (T - 273.15) \right] \quad (4.16)$$

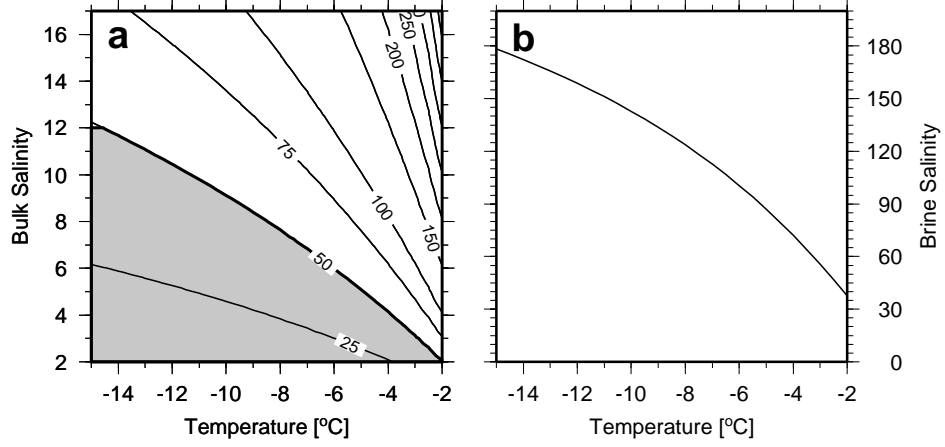


Figure 4.2: (a) Isolines of brine volume in ppt dependent on sea ice temperature and bulk salinity. The shaded area represents values where the ice is considered impermeable (see Section 4.2). (b) Brine salinity vs. temperature following the phase relations described by Assur [1958].

The specific heat of a sea ice layer c_{ice} is taken from Schwerdtfeger [1963]

$$c_{ice} = c_i - \frac{S_i (c_w - c_i)}{\alpha_{TS}(T - 273.15)} + \frac{S_i L}{\alpha_{TS}(T - 273.15)^2} \quad (4.17)$$

where $c_i = 2.01 \times 10^3 \text{ J kg}^{-1} \text{ K}^{-1}$ is the specific heat of pure ice, $c_w = 4.23 \times 10^3 \text{ J kg}^{-1} \text{ K}^{-1}$ is the specific heat of water, $L_i = 333.4 \times 10^3 \text{ J kg}^{-1} \text{ K}^{-1}$ is the latent heat of pure ice and $\alpha_{TS} = 18.2 \text{ K}^{-1}$ is the slope of the linear relationship between temperature and salinity of the brine. It is important to note that the thermal properties of each layer depends on its temperature and salinity, and are calculated in each timestep.

Table 4.1: Coefficients for the functions $F_1(T)$ and $F_2(T)$ used to determine the sea ice brine volume, density and thermal conductivity, taken from Leppäranta and Manninen [1988] for the temperature range between 0 and -2°C and from Cox and Weeks [1983] for temperatures below -2°C .

$F_1(T)$				
Temp. Range ($^\circ\text{C}$)	α_0	α_1	α_2	α_3
$0.0 \geq T > -2.0$	-4.221×10^{-2}	-1.8407×10^1	5.4802×10^{-1}	2.4154×10^{-1}
$-2.0 \geq T > -22.9$	-4.732	-2.245×10^1	-6.397×10^{-1}	-1.074×10^{-2}
$-22.9 \geq T > -30.0$	9.899×10^3	1.309×10^3	5.527×10^1	7.160×10^{-1}
$F_2(T)$				
Temp. Range ($^\circ\text{C}$)	α_0	α_1	α_2	α_3
$0.0 \geq T > -2.0$	9.0312×10^{-2}	-1.6111×10^{-2}	1.2291×10^{-4}	1.3606×10^{-4}
$-2.0 \geq T > -22.9$	8.903×10^{-2}	-1.763×10^{-2}	-5.330×10^{-4}	-8.801×10^{-6}
$-22.9 \geq T > -30.0$	8.547	1.089	4.518×10^{-2}	5.819×10^{-4}

The divergent of irradiance or internal heating source ($\frac{\partial \mathcal{F}_i(z)}{\partial z}$ in Eq. 4.9), is given by the parcel of the shortwave radiation transmitted within sea ice which is absorbed and consequently, re-emitted in form of thermal radiation, including the energy absorbed by chlorophyll but not used in the photosynthesis.

$$\frac{\partial \mathcal{F}_i(z)}{\partial z} = \begin{cases} \int_{290}^{4000} [K_{ice}(\lambda) + f_{phot} K_{chl}(\lambda)] E_{tot}^{z^0}(\lambda) \\ \quad \times \exp \{ [K_{ice}(\lambda) + f_{phot} K_{chl}(\lambda)] z \} d\lambda & \text{for sea ice} \\ \int_{290}^{4000} K_{snow}(\lambda) E_{tot}^{z^0}(\lambda) \exp [-K_{snow}(\lambda) z] d\lambda & \text{for snow} \end{cases} \quad (4.18)$$

where $E_{tot}^{z^0}(\lambda)$ is the spectral solar irradiance in the top of the layer z , $K_{ice}(\lambda)$, $K_{snow}(\lambda)$ and $K_{chl}(\lambda)$ are the spectral extinction coefficient contribution of sea ice, snow and microalgae, respectively. The factor f_{phot} is the energy absorbed by chlorophyll and re-emitted as heat [Zeebe *et al.* 1996]. In theory $f_{photo} = 1 - \nu$, where ν is the photosynthetic efficiency. Since values of ν for natural sea ice populations are still lacking on field observations, a conservative value of $f_{phot} = 0.95$ is assumed [Zeebe *et al.* 1996]. They work demonstrated that the magnitude of melting influenced by the divergence of irradiance is negligible as compared with other energy fluxes within sea ice, but it has considerable ecological significance since small changes in the temperature-brine phase relations will directly impact the habitat of sea ice microbial populations. The determination of the spectral extinction coefficients of sea ice, as well as the spectral solar irradiance, are detailed in the Chapter 3.

4.1.3 Freezing and Melting at the Ice-Ocean Interface

After the determination of the temperature profile and the gradient of temperature in the bottom-most layer, melting or accretion in the bottom of ice (H_{ice}) is given by the energy balance at the ice-water interface, according to

$$\rho_{ice} L \frac{dH_{ice}}{dt} = k_{ice} \left. \frac{\partial T}{\partial z} \right|_{bot} - \mathcal{F}_{ocean} \quad (4.19)$$

where ρ_{ice} is the density of the bottom-most layer, L is the latent heat of fusion, k_{ice} is the thermal conductivity in the bottom-most layer and \mathcal{F}_{ocean} is the oceanic heat flux.

Although many studies in the Weddell Sea showed that the oceanic heat flux can have strong spatial and temporal fluctuations depending on different hydrodynamic processes [Lytle and Ackley 1996, McPhee *et al.* 1999], most of the sea ice models use fixed values of \mathcal{F}_{ocean} varying from 0-2 W m⁻² [Lemke *et al.* 1990, Hibler III and Ackley 1983] to 20 W m⁻² [Martinson 1994], to estimate ice thickness. However, the dynamic incorporation of biological material and posterior brine fluxes in sea ice are thermodynamically driven process related to ice growth and melting rates [Ackley and Sullivan 1994]. Realistic vertical profiles of sea ice properties can be simulated only by assuming the variability in the boundary conditions used to solve the thermodynamic model. For this reason, a climatological dataset with monthly means of oceanic heat flux is used instead of a fixed value. This dataset is obtained from the BRIOS-2 coupled sea ice-ocean model [Timmermann *et al.* 2001] with an original spatial resolution of $1.5^\circ \times 1.5 \cos \text{latitude}$ and used as a forcing field for the thermodynamic sea ice model.

4.2 Fluxes of Brine, Salt, Nutrients and Biological Material

Vertical profiles of sea ice salinity and brine volumes have been the focus of some modeling studies [Cox and Weeks 1988, Eicken 1992; 1998], with emphasis on their interactions with thermodynamic processes. Basically, the amount of brine entrapped within a newly formed bottom layer is a function of the ice growth rate (the velocity of the advancing ice-ocean interface). The bulk salinity S_i of newly accreted layers is determined by a partitioning coefficient k_{eff} and the salinity of the underlying seawater S_{wat} (≈ 33.5 for the Weddell Sea following Olbers *et al.* [1992]), written as

$$S_i = k_{eff} S_{wat} \quad (4.20)$$

The relationship between k_{eff} and the sea ice growth velocity v_i (in mm s⁻¹) is described by Eicken [1998] as

$$k_{eff} = \begin{cases} 0.12 & \text{for } v_i < 1.25 \times 10^{-5} \\ 0.7617 + 0.0568 \ln v_i & \text{for } 1.25 \times 10^{-5} \leq v_i \leq 3.6 \times 10^{-4} \\ \frac{0.26}{0.26 + 0.74 \exp(-724.3 v_i)} & \text{for } v_i > 3.6 \times 10^{-4} \end{cases} \quad (4.21)$$

During sea ice growth, newly accreted layers cool down and freeze the liquid brine, forming a differential decrease in porosity with segregation and expulsion of brine. This *brine expulsion* process is defined as a decrease in salinity controlled by a drop in the temperature from T_1 to T_2 , empirically given by [Cox and Weeks 1986]

$$\frac{S_i(T_2)}{S_i(T_1)} = \left[1 - \frac{1}{\rho_i} \right] \frac{S_b(T_2) \rho_b(T_2)}{S_b(T_1) \rho_b(T_1)} \exp \left[\frac{C}{\rho_i S_b(T_1) - S_b(T_2)} \right] \quad (4.22)$$

where S_b is the brine salinity and ρ_b is the brine density at temperatures T_1 and T_2 , respectively, ρ_i is the density of pure ice ($\rho_i = 918 \text{ kg m}^{-3}$) and C is a constant describing the density variation in function of the temperature ($C \equiv d\rho_b/dT = 0.8 \text{ kg m}^{-3} \text{ K}^{-1}$). In the same way, a rise in the temperature within a ice layer causes an increase in bulk salinity (with brine salinity decreasing) due to differential increase in the pore volume [see also Cox and Weeks 1974].

In sea ice, salinity and density of the brine are a function of the temperature. The colder the ice, the saltier and dense the brine [Richardson 1976]. As the ice grows, a positive gradient in temperature is formed (the top layers are colder than the bottom layers) which produces an instability in the brine density profile. The convective overturn and exchanges of denser brine within ice layers and with the less saline underlying seawater depend not only of the temperature but also of the ice permeability. Due to complexities in the internal ice brine structures, a rigorous theoretical model of brine drainage is still lacking, but quantitative estimates can be obtained using the empirical formulas of Cox and Weeks [1975]. Their laboratory experiments showed that the changes in the bulk salinity $\Delta S_i/\Delta t$ can be related to the temperature gradient and the brine volume following the relationship

$$\frac{\Delta S_i}{\Delta t} = 1.68 \times 10^{-5} \frac{\partial T}{\partial z} - 3.37 \times 10^{-7} V_b \frac{\partial T}{\partial z} \quad (4.23)$$

where V_b is the brine volume (ppt). When V_b drops below a threshold of 50 ppt, the ice layer is then considered impermeable and the brine gravity drainage is set to zero. The relationship between the change in bulk salinity due to gravity drainage, temperature and brine volume is shown in the Fig. 4.3a.

The model assumes that sea ice grows as congelation ice, which deviates significantly from the Antarctic sea ice growth patterns (accumulation of frazil ice at the initial stages of

the pancake cycle). However, Eicken [1992] demonstrated that desalination processes occur in the same way for both frazil and congelation ice, with no significant differences in the salinity profiles for both ice types.

4.2.1 Nutrient Dynamics in Sea Ice

Although there are no observations or experimental data describing nutrient fluxes in Antarctic sea ice, the accumulation of dissolved nutrients from the underlying seawater in brine must be driven by the same mechanism responsible for salt accumulation (Eq. (4.20)), with a specific partition coefficient k_{eff} . To simulate the accumulation and segregation of dissolved nutrients in sea ice brine, their fluxes are coupled with brine fluxes, assuming that they decrease at the same proportion that brine is lost by expulsion and drainage. Nutrient concentrations of newly accreted layers are calculated after determining their bulk salinity following the equation

$$N_i = S_i \frac{N_{wat}}{S_{wat}} \quad (4.24)$$

where N_{wat} is the concentration of dissolved nitrogen [N] or silicate [Si] in the underlying seawater.

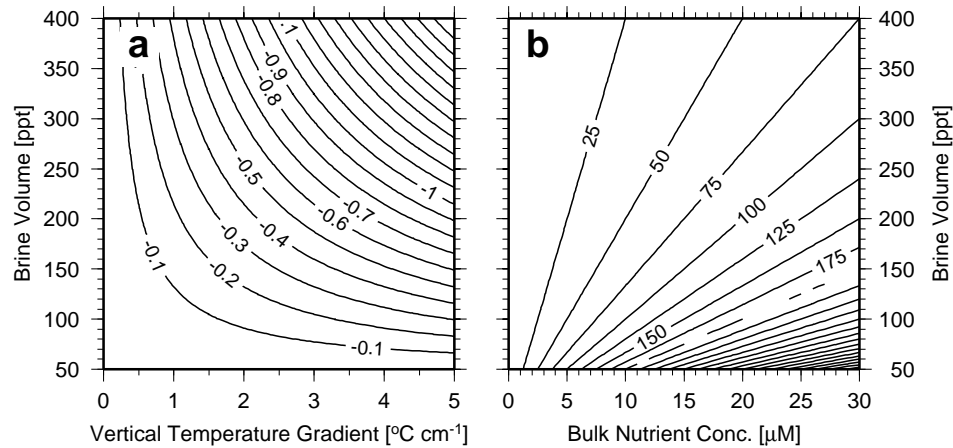


Figure 4.3: (a) Isolines of $\Delta S_i / \Delta t$ (in $\Delta S_i \text{ h}^{-1}$) as a function of the brine volume and the temperature gradient. (b) The nutrient in brine as a function of the bulk nutrient concentration and brine volume, as calculated by Eq. (4.26).

Since the brine expulsion and drainage affect the bulk salinity, changes in the sea ice nutrients must obey the same processes as salts, as follows

$$\frac{N_i(t_2)}{N_i(t_1)} = \frac{S_i(t_2)}{S_i(t_1)} \quad (4.25)$$

where (t_1) refers to the time before and (t_2) the time after brine expulsion and drainage. The time variation of nutrients is also related to their biological uptake which is simulated in parallel within the thermodynamic model and coupled after each model cycle (see Section 4.3).

The brine nutrient concentration N_b , which is the *real* concentration sea ice microalgae experiments within brine channels, is related to the brine volume V_b (in percent volume = ppt/1000) by the relationship

$$N_b = \frac{N_i}{V_b} \quad (4.26)$$

Figure 4.3b shows how a generic nutrient with concentration N_b changes as a function of the brine volume. The direct measurements of nutrient concentrations in brine is very difficult because contamination effects due to brine flow and melting ice can easily occur during sampling [Smith *et al.* 1990].

Observations at different seasons for ice covered conditions in the Weddell Sea showed that nutrients in seawater have a constant background value, except when the ice cover fraction drops below 20% enhancing the availability of light in the water column and nutrients depletion due to phytoplankton blooms [Cota *et al.* 1992, Arrigo *et al.* 1999]. For the sea ice model, the background values of dissolved nutrients in seawater are 30 μM DIN and 65 μM $\text{Si}(\text{OH})_4$, following the observations of Dieckmann *et al.* [1991a].

4.2.2 Incorporation and Accumulation of Biological Communities in Sea Ice

Algal cells and other particles in the water column are harvested into sea ice when frazil ice develops in the water column as suspended crystals during turbulent freezing conditions [Ackley and Sullivan 1994]. They adhere to the crystal surface and are transported upward to the surface during the initial phase of ice formation. Physical accumulation of biological material may help to explain some regional differences found in the vertical distribution of sea ice assemblages. Garrison *et al.* [1983] suggested that sea ice microalgal populations in the Weddell Sea are characterized by interior communities contrasting with bottom and top ice assemblages in other polar regions. Lange *et al.* [1989] found that the frazil ice production in the Weddell Sea is an almost continuous process, which may contribute to the constant harvesting of algal cells from the water column to the sea ice. Turbulent mixing

associated with the transference of momentum between ice and water also results in transport of material from the underlying water column to the ice-ocean interface [Smith and Morison 1993] and new material can be incorporated during sea ice growth.

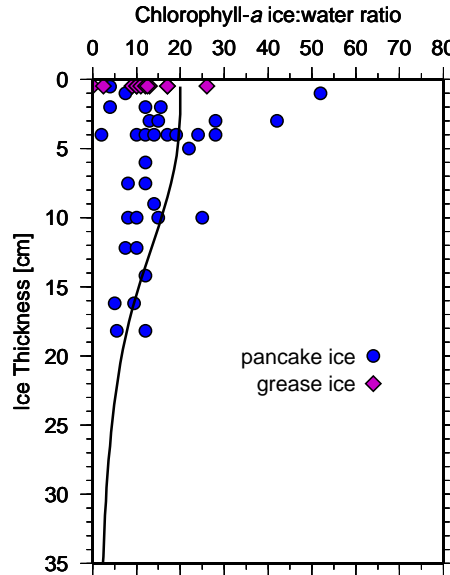


Figure 4.4: Accumulation of chlorophyll-*a* in newly forming sea ice as a function of ice thickness observed by Garrison *et al.* [1989]. Note that values are expressed as a ratio of chlorophyll-*a* between sea ice and the underlying water. The solid line is the accumulation function (γ_{chl} , equation 4.27) used in the model to initialize the chlorophyll-*a* concentrations in newly formed sea ice layers.

Field measurements of chlorophyll-*a* from Garrison *et al.* [1989], indicated that microalgae can be accumulated in sea ice up to 50 times the concentration observed in the water column (Fig. 4.4) with representative values ranging between 15 and 20 times for very thin ice and exponentially decreasing at greater ice thickness. To simulate this incorporation process in the sea ice, the ratio between the chlorophyll-*a* concentration in ice and the underlying seawater is given by a cubic hyperbolic function

$$\gamma_{chl} = 1 + 19 \left\{ 1 - \left[\left(\frac{I_k}{I_t} \right)^3 + 1 \right]^{-1} \right\} \quad (4.27)$$

where I_t is the ice thickness (in cm) and the I_k is the inflexion point of the hyperbola, representing the ice thickness when γ_{chl} (solid line in the Fig. 4.4) is at half of its maximum. Following Garrison *et al.* [1989], γ_{chl} is assumed to have a maximum value of 20 and the $I_k = 15$ cm. For a given chlorophyll-*a* concentration in the water column (P^{Chl}), the sea ice

chl-*a* in newly formed layers is given by

$$P_{ice}^{Chl} = P_{ocean}^{Chl} \gamma_{chl} \quad (4.28)$$

The initialization of the biological variables in the sea ice (P^C , P^N and P^{Si}) is calculated over the initial chlorophyll-*a* concentration and fixed ratios between Chl-*a*:Carbon $Q^{Chl:C}=0.01$ g Chl (g C)⁻¹, nitrogen-to-carbon cellular quota $Q^{N:C}=0.176$ g N (g C)⁻¹, and silicon-to-carbon ratio $Q^{Si:C}=0.671$ g Si (g C)⁻¹, following the proportions C:N:Si \approx 106:16:30.5 molar. These values are based on observations from young sea ice and water column samples in the Weddell Sea [Nelson and Gordon 1982, Cota *et al.* 1992, Gleitz and Thomas 1993]. Initial protozoa carbon biomass in the sea ice is assumed to be incorporated at a ratio of 1% of microalgal carbon biomass and a protozoa nitrogen-to-carbon mass ratio of 0.176 (\approx 6.6 C:N molar).

4.2.3 Vertical Reallocation of Biological Material

After incorporation, the biological sea ice community formed in each layer is subject to environmental changes (light, temperature, nutrients) related to the physical processes which occur during sea ice growth. Little information is available on how thermodynamic processes affect the distribution of microbial assemblages in sea ice, but observations made in young ice in the Weddell Sea [Melnikov 1995] suggest that brine fluxes and desalination processes within sea ice just after its formation enhance the vertical reallocation of newly incorporated biological material.

Krembs and Engel [2001] found a high concentration of extracellular polymeric substances (EPS) produced by diatoms in sea ice microbial bottom communities in the Laptev Sea. Their observations suggest that sea ice microalgae uses the adhesive properties of EPS to maintain their position near the advancing ice-water interface during ice growth. However, the vertical migration of organisms inside the ice brine channels depends on the sea ice permeability and how the channels are interconnected. To simulate the vertical reallocation of biological material within sea ice, the time-dependent advection of cells is coupled to the brine flux calculated at each model cycle. Assuming that gravity drainage is the dominant process controlling the flux of brine, the temporal change of a biological variable E ($\equiv P^C$,

P^{Chl} , P^N , P^{Si} , Z^C or Z^N) for a given ice layer with vertical position j is written as

$$\frac{\Delta E^{(j)}}{\Delta t} = \gamma_g^{(j-1)} E^{(j-1)} - \gamma_g^{(j)} E^{(j)} \quad (4.29)$$

where the coefficient $\gamma_g = C \left| \frac{\Delta S_i}{\Delta t} \right|$ is related to the brine gravity drainage (Eq. (4.23)) with the constant C representing the microorganisms mobility in the brine ($\approx \Delta E / \Delta S_i$). For the topmost layer ($j = 1$), the first term on the right hand side of Eq. (4.29) is set to zero and for the bottom-most layer ($j = N$ where N is the number of model layers), no outflow of biological material to the water column is assumed and the second term on the right hand side of Eq. (4.29) is zero.

Based upon chlorophyll-*a* and bulk salinity of sea ice samples obtained from young sea ice in the Weddell Sea (ice thickness ≤ 20 cm) during the onset of the ice growth season [Dieckmann *et al.* 1998], C was empirically defined as ≈ 4 . The sensitivity of γ_g to the value of C is noticeable only for strong variations in the ice salinity, since this coefficient depends on the changes in the flux of brine given by $\frac{\Delta S_i}{\Delta t}$. Because sea ice protozoa have a considerable higher motility in the liquid brine than microalgae, the constant C should be proportionally greater than 4. Experimental data of Krembs *et al.* [2000] indicated that the expulsion of heterotrophic protists due to cooling of sea ice and brine drainage is 2 times faster than for microalgae, in part due to the reduction of the available internal ice surface in the brine channels and the size distribution of sea ice heterotrophic protists. Therefore, the value of γ_g for sea ice protozoa is assumed to be $= 8$.

During the initial stages of ice formation, desalination of ice layers will enhance the flux of biological material to underlying ice layers. Decreasing the sea ice salinity, the ice layers become impermeable when the brine volume drops below 50 ppt (Fig. 4.2), stopping the vertical flux of biological material. When the ice warms, the brine volume increases (Eq. (4.13)) resulting in a proportional rising in γ_g .

A simulation of the redistribution mechanism described above was performed by forcing the thermodynamic model with a time-series of air temperature obtained from the central Weddell Sea (Fig. 4.5) for a 75-days period starting on 15 May 1992, and keeping a constant oceanic heat flux $\mathcal{F}_{ocean} = 30 \text{ W m}^{-2}$ [McPhee *et al.* 1999]. These boundary conditions are representative for the beginning of the ice growth season in the Weddell Sea [Lytle and

Ackley 1996]. The chlorophyll-*a* concentration of newly formed ice layers was calculated using Eqs. (4.27) and (4.28) with P_{ocean}^{Chl} set to $0.1 \mu\text{g Chl-}a \text{ l}^{-1}$. The time-dependent vertical distribution of chl-*a* in sea ice was determined using Eq. (4.29) with $C = 4$ and the partial results plotted at 15, 30 and 60 days of simulation, which correspond to 20, 40 and 60 cm of ice thickness, respectively (Fig. 4.6).

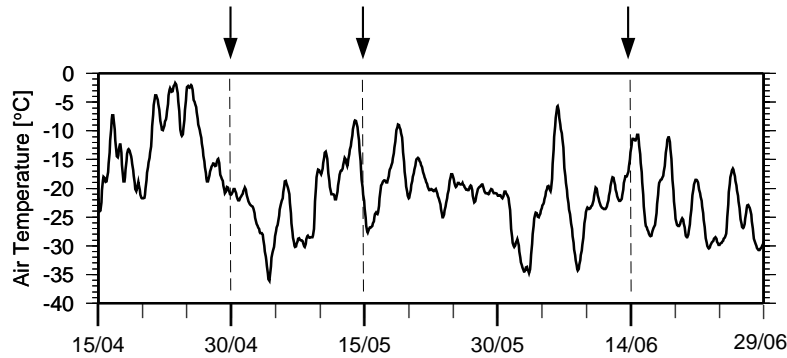


Figure 4.5: Air temperature during the simulated run to show accumulation and redistribution of biological material in sea ice. The arrows mark the days where vertical profiles of ice properties were taken (see Fig. 4.6).

In the first 5 days of ice formation, low air temperatures forcing the conductive heat flux through the ice were responsible for strong changes in the ice salinity and downward flux of chlorophyll-*a* from the topmost layers to the bottom of the ice. The period with relatively warmer air temperatures ($\sim -5^\circ\text{C}$) between day 5 and 10 was followed by a drop to -20°C forming a vertical gradient in the salinity profile (Fig. 4.6 left). In this period, the ice thickness reached 20 cm resulting in a mean ice growth of 1.3 cm day^{-1} . In the following 5 days, the air temperature decreased to -35°C and the brine volume at 15 cm ice depth was reduced below 50 ppt producing an impermeable layer. Below this vertical position, newly accreted material still moved downward forming a second vertical maximum of chlorophyll-*a* after 30 days, corresponding to an ice thickness of 40 cm (Fig. 4.6 center). The following 30-days period was marked by fluctuations in the air temperature and the formation of a second impermeable layer at 40 cm depth (Fig. 4.6 right). The final thickness of 60 cm was reached after 60 days with a mean ice growth rate of $\approx 0.7 \text{ cm day}^{-1}$ in the period.

The simulated vertical profile of chlorophyll-*a* in sea ice is very similar to observed patterns in the Weddell Sea during the winter [Ackley *et al.* 1979, Garrison and Close 1993, Drinkwater and Haas 1994, Fritsen *et al.* 1994]. Since no biological production is expected to

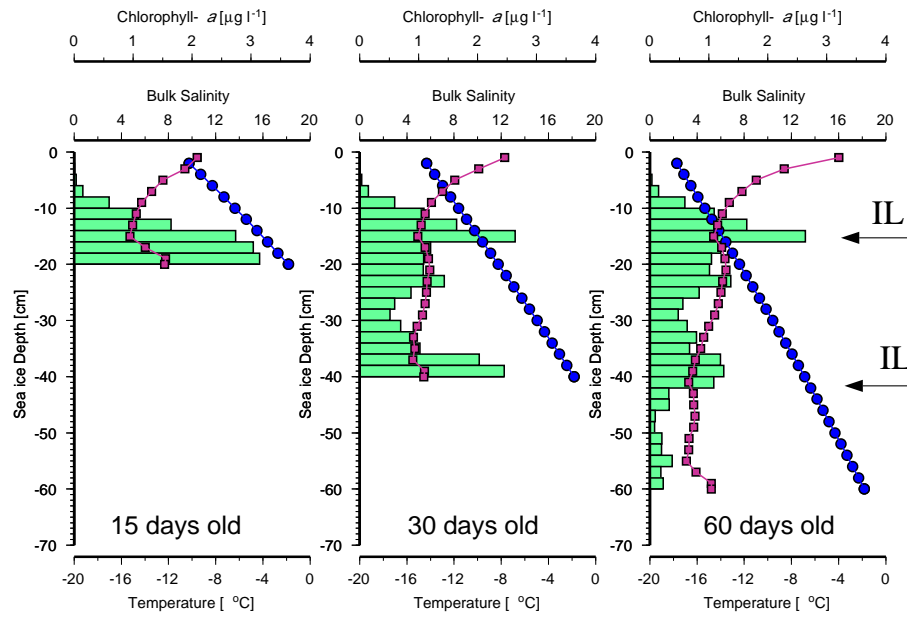


Figure 4.6: Simulated time-dependent accumulation and vertical redistribution of chlorophyll-*a* in sea ice during thermodynamic growth. Vertical profiles of temperature (circles), salinity (squares) and Chl-*a* (bars) after 15 days of simulation (left), 30 days (center) and 60 days (right). The arrows mark the vertical position of impermeable layers (IL). See text for details.

occur during the dark winter in the central Weddell Sea, the vertical distribution of biological material in sea ice may be influenced only by the physical processes related to the ice growth and dynamics, as indicated by the simulation.

4.3 Model Time Step

In contrast to the empirical functions used to estimate the ice desalination and the vertical redistribution of biological material, the heat conduction equations (Section 4.1), as well as the biological model (Chapter 2) have to be solved numerically. However, physical and biological processes occur at different time scales making necessary their separated integration. The model components (biology and thermodynamics) are coupled every $\Delta t=2$ hours. Figure 4.7 shows a schematic representation of the model timestep, showing the time *nodes* where the model components are coupled. The thermodynamic sea ice model is solved in a forward-time centered-space (FTCS) finite-difference scheme with a vertical resolution of $\Delta z=2$ cm. Newly accreted bottom ice layers have a variable Δz , depending on the ice rowth rate. Therefore, the model timestep is set to $\Delta t_{thermo} = 36$ s, which is 5 times below the minimum Δt required for numerical stability.

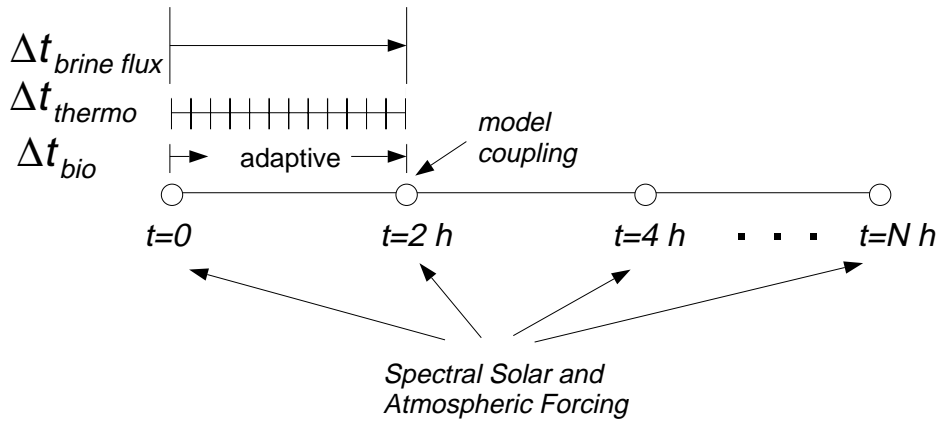


Figure 4.7: Schematic representation of model timestep and coupling. The update of atmospheric forcing fields and the calculation of the incoming solar spectral radiation are made at each main timestep (2 h), before each model cycle.

The biological sea ice model, described in the Chapter 2, is solved for each ice layer using a fifth-order Runge-Kutta Cash-Karp algorithm [Press *et al.* 1992], with adaptive stepsize in the time intervals constrained by the main model timestep (2 hours). An analysis of the estimated time intervals used by Runge-Kutta algorithm revealed that for relative high carbon assimilation rates ($\approx 0.6 \text{ day}^{-1}$), the integration time interval vary from 1 to 5 minutes, increasing to ≈ 15 minutes for low assimilation rates. The adaptive stepsize scheme allows the self-adjusting time interval for integration, leading to a better description of the model time evolution.

The incoming spectral solar radiation, as well as the ice desalination and the vertical redistribution of biological properties are calculated at the main timestep, as indicated in Fig. 4.7. Coupling is performed by updating the model variables at each main timestep.

Chapter 5

Coupling Physical and Biological Processes in Sea Ice

The modeled sea ice thermodynamics and biological production can be validated comparing simulated and observed time-series of the vertical distribution of sea ice properties. Such a comparison is difficult since long observational time-series in the Antarctic pack-ice are still lacking. Currently, the monitoring of sea ice consists of snapshots of vertical gradients of temperature, salinity and chlorophyll-*a* which are available for most seasons, especially in the Weddell Sea region.

Sea ice is not stationary but driven by oceanic currents and winds since the first stages of its formation. Previous attempts to compare observational data with modeled results showed difficulties to represent the vertical distribution of sea ice properties. Synoptic effects of atmospheric forcing and the spatial variability of ice dynamics lead to a differentiation of sea ice characteristics that most models do not take into account.

Biological communities in the sea ice are subject of constant environmental changes (e.g. temperature, light, nutrients). The existent estimates of sea ice biological production are made in an *Eulerian* approach, i.e. the coordinates used to simulate the time evolution of sea ice are fixed in space. However, sea ice shows a typical *Lagrangian* pattern, where ice floes experience a continuous drift exposing sea ice communities to different environmental conditions at moderate regional scales. This can be demonstrated comparing time-series of air temperature experienced by a stationary and a drifting floe (Fig. 5.1).

The computed air temperatures for both stationary (Eulerian) and drifting (Lagrangian) ice floes are similar during the first months due to their proximity and the small horizontal gradient in the air temperature. By the middle of March, when the sea ice edge advances northward and the distance between the stationary and drifting floes reaches ≈ 400 km,

differences in the air temperature for the present and initial floe positions increase up to 30 K. The impact of this spatial variability on the biological sea ice production is still not well understood.

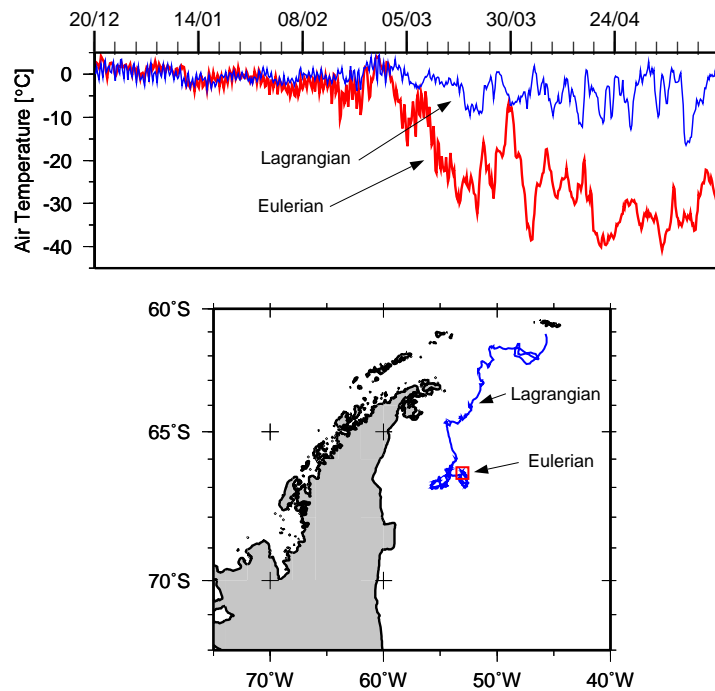


Figure 5.1: Variability in the air temperature observed for a drifting ice buoy (Lagrangian) compared with its initial position (Eulerian). Data from Kottmeier *et al.* [1997].

The use of simulated Lagrangian drifters in modeling studies to track the movement of water masses is a common task since the beginning of ocean modeling [Garwood Jr. *et al.* 1998]. This approach has been used in some sea ice models in the so called *free drift solution* schemes [Gutfraind and Savage 1997, Bitz and Lipscomb 1999, Bitz 2000] where the ice is assumed to be a reference unit area that moves as if it was an isolated object (i.e. a single floe).

In this chapter, the time evolution of sea ice thickness and the associated biological production are simulated by coupling physical and biological one-dimensional models in a Lagrangian approach, where the time-dependent floe positions are computed from ice motion fields. Model forcing (e.g. air temperature, oceanic heat flux, solar radiation) is obtained for each floe position allowing the tracking of the past thermodynamic history of the ice floes.

5.1 Simulating Sea Ice Lagrangian Drifters

Ice cores collected during the expedition ANT X/4 on board the R/V *Polarstern* in 1992 [Lemke 1994] within the framework of the Winter Weddell Gyre Study (WWGS92) were used to validate the coupled physical-biological sea ice model. The sea ice program of the WWGS92 consisted in sampling a main ice core for subsequent analysis of snow and ice thickness, temperature, bulk salinity and ice texture, and a biological core to chlorophyll-*a* measurements [Drinkwater and Haas 1994]. The time-backward trajectories from positions (ice floes) where ice cores were obtained can be used to simulate the thermodynamic history of the cores and, therefore, to assert the influence of environmental changes in the sea ice biota.

Table 5.1: Simulated origin and final position of ice floes collected during the WWGS92. The symbol \odot marks the position where the ice core was sampled and \square the simulated origin of the floe. Core number is used as a label in Fig. 5.2 and the code between brackets refers to the original ice core identification [Lemke 1994].

Core Nr.	Date	Lat	Lon	Days of Drift
1 [n0416801]	\odot 16/06/1992	67° 18.30' S	000° 01.02' E	27
	\square 20/05/1992	67° 39.06' S	004° 48.72' E	
2 [n0418701]	\odot 05/07/1992	71° 22.26' S	016° 16.14' W	72
	\square 23/04/1992	70° 30.30' S	009° 50.40' W	
3 [n0418901]	\odot 07/07/1992	71° 58.98' S	017° 49.08' W	23
	\square 13/06/1992	71° 27.54' S	012° 49.14' W	
4 [n0419201]	\odot 10/07/1992	69° 09.78' S	025° 03.84' W	106
	\square 25/03/1992	74° 24.60' S	022° 04.86' W	
5 [n0419301]	\odot 11/07/1992	68° 27.42' S	026° 15.54' W	114
	\square 18/03/1992	74° 05.34' S	030° 25.56' W	
6 [n0419501]	\odot 13/07/1992	65° 37.74' S	033° 22.56' W	87
	\square 17/04/1992	67° 16.26' S	041° 32.40' W	
7 [n0419701]	\odot 15/07/1992	65° 12.30' S	037° 24.60' W	89
	\square 16/04/1992	66° 37.44' S	050° 56.82' W	
8 [n0420101]	\odot 19/07/1992	63° 23.76' S	043° 22.08' W	60
	\square 19/05/1992	62° 41.58' S	049° 55.56' W	

One of the most recent studies in regional sea ice modeling is the coupled sea ice-ocean model (BRIOS-2) [Timmermann *et al.* 2001]. The ice component of the BRIOS-2 is a dynamic-thermodynamic sea ice model with a viscous-plastic rheology, allowing the computation of the ice velocity field with a spatial resolution of 1.6875° in the zonal and 0.5625° in the meridional directions in the Weddell Sea. Using the modeled ice velocity fields obtained

for every 6 hours, the positions of individual floes are calculated backward in time until the drift of the floe reaches a boundary (land or open ocean) of the ice field¹. This position is considered to be the primordial origin of the floe and the resulting temporal series of subsequent positions is used to compute atmospheric forcing fields (air temperature, surface atmospheric pressure, precipitable water vapor, relative humidity, wind velocity and cloud cover) from NCEP/NCAR Reanalysis 4× daily surface dataset².

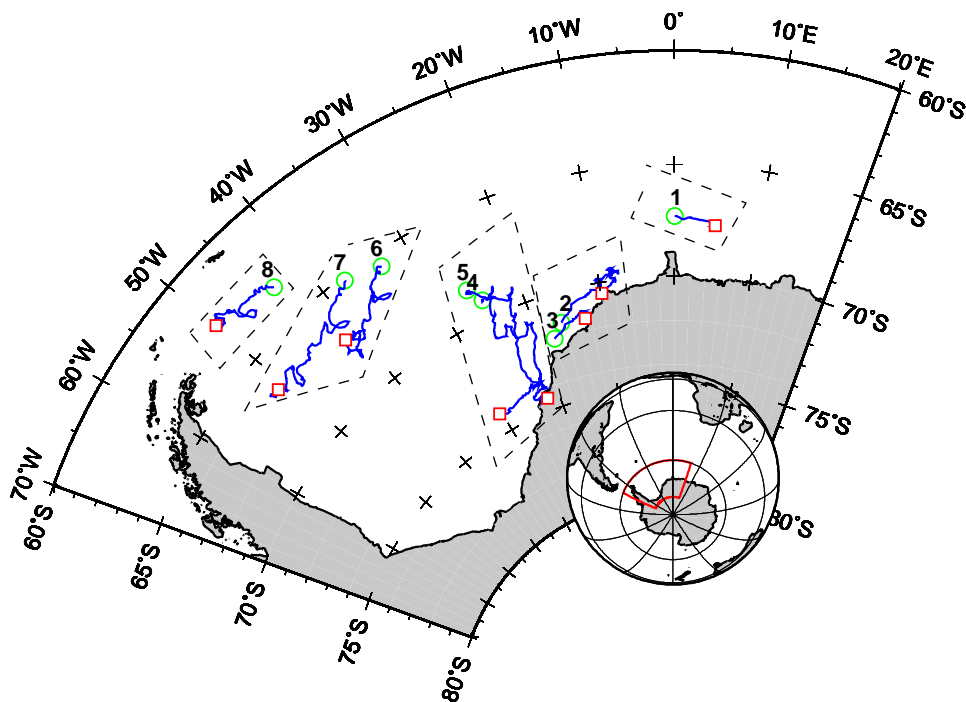


Figure 5.2: Simulated track of ice floes sampled during the WWGS92. Green circles (⊙) mark the station positions where ice cores were taken and red squares (□), the simulated origin of the floes computed from daily sea ice drift estimates of the BRIOS-2 coupled sea ice-ocean model. See Table 5.1 for labels.

Eight stations were selected from a total of 33 in the original WWGS92 ice core dataset, representing 5 different ice conditions and with similar initial and final positions. The ice texture of all eight cores indicate that they are typical first-year ice, ranging from 46 to 100 cm length. Figure 5.2 shows the simulated drifts (labels are described in the Table 5.1). The time evolution of temperature, salinity and the associated biological production in sea ice was simulated coupling all described models: the biological sea ice model (Chapter 2),

¹It is important to note that due to the computation of drift backward in time, the floe can reach a position with no ice in the velocity field, indicating the primordial area of ice formation.

²NCEP/NCAR - National Centers for Environmental Prediction/National Center for Atmospheric Research datasets from meteorological and modeling data assimilation in a $2.5^\circ \times 2.5^\circ$ resolution global grid provided by the NOAA-CIRES Climate Diagnostic Center, Boulder - Colorado USA. More information at <http://www.cdc.noaa.gov>.

the spectral bio-optical model (Chapter 3) and the vertical high-resolution thermodynamic model (Chapter 4). The final simulated sea ice vertical profiles of temperature, salinity and chlorophyll-*a* were compared with observed values for each ice core. The daily rates of snow accumulation used in the coupled model were computed from the observed snow thickness and the days of drift (see Table 5.2).

To verify the degree of agreement between observed and simulated values of chlorophyll-*a* biomass, the mean *bias* was computed according to

$$\text{bias} = \frac{\sum_{i=1}^n O_i^{Chl} - S_i^{Chl}}{n}$$

where O_i^{Chl} is the observed chlorophyll-*a* concentration and S_i^{Chl} is the simulated chlorophyll-*a* concentration in the vertical section i at the end of the simulation. Since the vertical sections in the ice cores where chlorophyll-*a* was measured (in general 10 cm thick) differs from the model grid spacing ($\Delta z = 2$ cm), simulated chlorophyll-*a* concentrations were averaged at the same vertical intervals where data were available. The *bias* is a statistical residual-based measurement that determines the correspondence between the mean forecast and the mean observation. It shows the distortion in $\mu\text{g Chl-}a \text{ l}^{-1}$ of estimated Chl-*a* values when compared to the observed values.

Table 5.2: Summary of observed and simulated vertical profiles with emphasis in the ice thickness, integrated chlorophyll-*a* biomass, mean ice growth rate and statistical analysis. TC means top communities and IBC interior-bottom communities. See text for details.

Core Nr.	Observed			Simulated			Snow Accum. [cm day ⁻¹]	<i>mean</i> <i>bias</i> [$\mu\text{g l}^{-1}$]	Group
	Snow thick. [cm]	Ice thick. [cm]	Integrated Chl- <i>a</i> [mg m ⁻²]	Ice thick. [cm]	Integrated Chl- <i>a</i> [mg m ⁻²]	Mean Ice Growth [cm day ⁻¹]			
1	7	92	2.34	93.0	2.25	3.4	0.26	-0.15	TC
2	2	46	0.12	45.7	0.14	0.6	0.03	-0.10	TC
3	3	54	0.55	54.3	0.59	2.3	0.13	-0.08	TC
4	12	60	2.26	58.8	2.22	0.5	0.11	-0.10	IBC
5	5	53	0.12	53.9	0.16	0.4	0.04	-0.10	IBC
6	5	65	0.62	65.8	0.62	0.7	0.06	-0.08	IBC
7	16	76	1.84	76.5	1.82	0.8	0.18	-0.29	IBC
8	11	100	2.55	98.8	2.48	1.6	0.18	-0.04	IBC

The computed floe drifts (Fig. 5.2) showed trajectories accompanying the main flow of the Weddell Gyre. Mean ice growth rates were calculated from the final ice thickness and flow age. They vary from 0.4 to 3.6 cm day⁻¹ which are in the range of ice growth rate estimates for the Weddell Sea [Eicken 1998]. In general, a good agreement between modeled and observed integrated chlorophyll-*a* was found, with the *bias* varying from -0.04 to -0.29. The negative *bias* for all samples suggests that the simulated values are slightly lower than observations (around 3-5%).

Based on the vertical position where the maximum chlorophyll-*a* concentration was observed, the simulated ice cores can be divided in two groups (Table 5.2): top communities (TC), where highest chlorophyll-*a* concentrations are found near the top sea ice layers, and interior-bottom communities (IBC), when the maximum chlorophyll-*a* concentrations are located in the interior and near the bottom ice layers. The first three cores, situated in the eastern Weddell Sea (see Table 5.2 and Fig. 5.2) show characteristic peaks in the top ice layers, while the cores westward of 20°W present typical development of interior and bottom communities. The individual analysis of each ice core revealed that such differences are related to the thermodynamic history of the floes during their drift in the Weddell Sea.

5.2 Individual Analysis of Simulated Ice Cores

Core #1 (see Table 5.1 and Fig. 5.2) drifted for 27 days along the latitude 67°S with decreasing solar light availability through the first 10 days. After this initial period, the ice floe entered in the polar night (Fig. 5.3, top). The floe was subject to relatively low air temperatures with two short cold events (< 3 days) reaching -20°C (Fig. 5.3, bottom) .

The observed salinity profile shows a typical *S*-shape [Eicken 1992] which was in general represented by the model (Fig. 5.4). The simulated vertical profile of the chlorophyll-*a* biomass shows that 80% of the total biomass is concentrated in the first 50 cm near the surface of the ice (Fig. 5.4). However, a second small peak of chlorophyll-*a* observed at 80 cm depth was not represented by the model. Since the bottom most layers were formed when the ice floe was already in the dark, this second chlorophyll-*a* peak is probably due to previous accumulation rather than production. In the model, the accumulation of biological material is associated to brine flux which depends on the salinity and temperature profiles. Therefore,

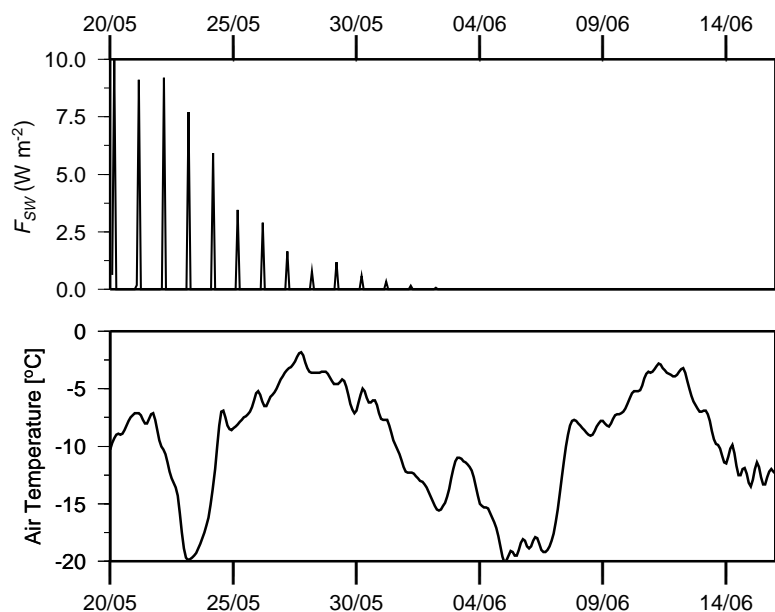


Figure 5.3: Time series of incoming solar radiation (top) and air temperature (bottom) during the drift of core #1.

the highest deviation between observed and simulated ice bulk salinities in the bottom most layers is the main cause of differences in the vertical position of the chlorophyll-*a* peaks.

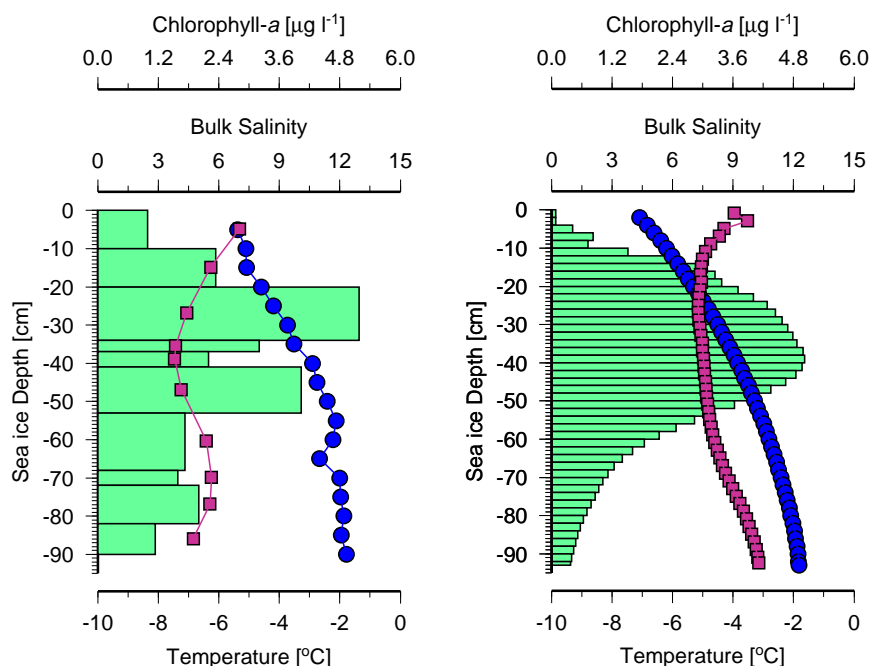


Figure 5.4: Observed (left) and simulated (right) vertical sea ice profiles for core #1 showing the temperature (circles), salinity (squares) and chlorophyll-*a* (bars).

In general, simulated and observed temperature profiles shows good good correlation (Fig. 5.4), with slightly lower simulated temperatures in the top layers (≈ 1 K) caused by differences between in situ air temperatures and the NCEP atmospherical forcing data used

in the model (see Appendix A). The time evolution of sea ice temperature and bulk salinity for core #1 (Fig. 5.5, bottom) shows that the effect of the short air temperature events (cold fronts) is transmitted through the sea ice up to a depth of ≈ 20 cm, but with less effect in the ice bulk salinities (Fig. 5.5, top).

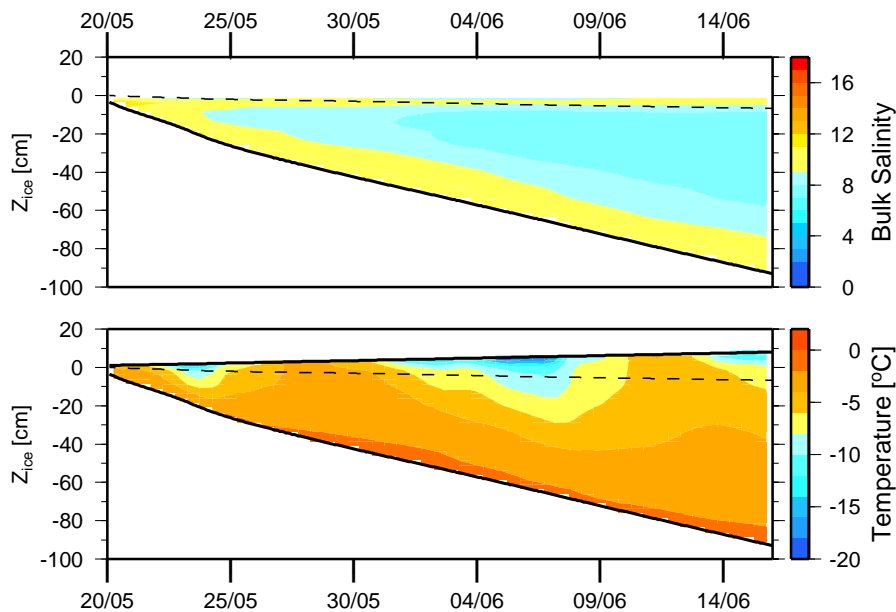


Figure 5.5: Simulated time evolution of the sea ice vertical salinity (top) and snow-ice temperature (bottom) profiles of core #1. The dashed line marks the relative seawater level.

Biological activity was computed in terms of sea ice daily net primary production (difference between microalgal photosynthetic carbon assimilation and grazing) and net secondary production (difference between protozoa carbon ingestion and respiration) integrated in the whole ice thickness. The daily net primary production for core #1 (Fig. 5.6) reduced drastically from $0.3 \text{ mg C m}^{-2} \text{ day}^{-1}$ in the first 6 days to $-0.08 \text{ mg C m}^{-2} \text{ day}^{-1}$ due to a constant decrease in the light regime and grazing. The daily integrated chlorophyll-*a* increased almost exponentially in the first days due to production, reaching an quasi-stationary state.

The decreasing rate in the primary production during the first 5 days suggests that the combined effects of low light conditions, drop in temperature and grazing play a key role in determining the initial biomass accumulation rate in sea ice. An increase in the solar radiation for the latitude 67°S will only occur in late October, implying that the sea ice in this region is in the dark for five months.

The sea ice cores #2 and #3 have similar drift trajectories, accompanying the Antarctic Coastal Current (Fig. 5.2). All 8 ice floes experienced short light periods with the excep-

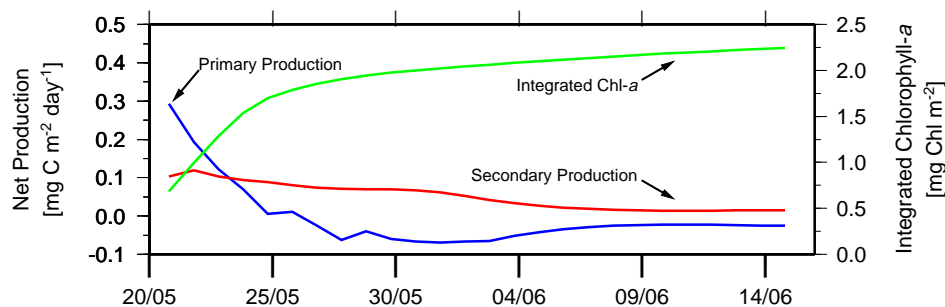


Figure 5.6: Simulated daily integrated chlorophyll-*a* (green), net primary production (blue) and net secondary production (red) for core #1.

tion of core #3, which had its origin in the middle of June at approximately 71°S latitude, drifting southwestward for 23 days in the dark. Its vertical profile (Fig. 5.7) shows that the chlorophyll-*a* biomass is concentrated in the top 30 cm and the bulk salinity is distributed in a C-shape profile, typical of first-year ice [Eicken 1992]. Significant differences between observed and simulated profiles occurred in the last 30 cm near the bottom, although the calculated $bias = -0.08$ indicates that the vertical variability in both simulated and observed cores are similar.

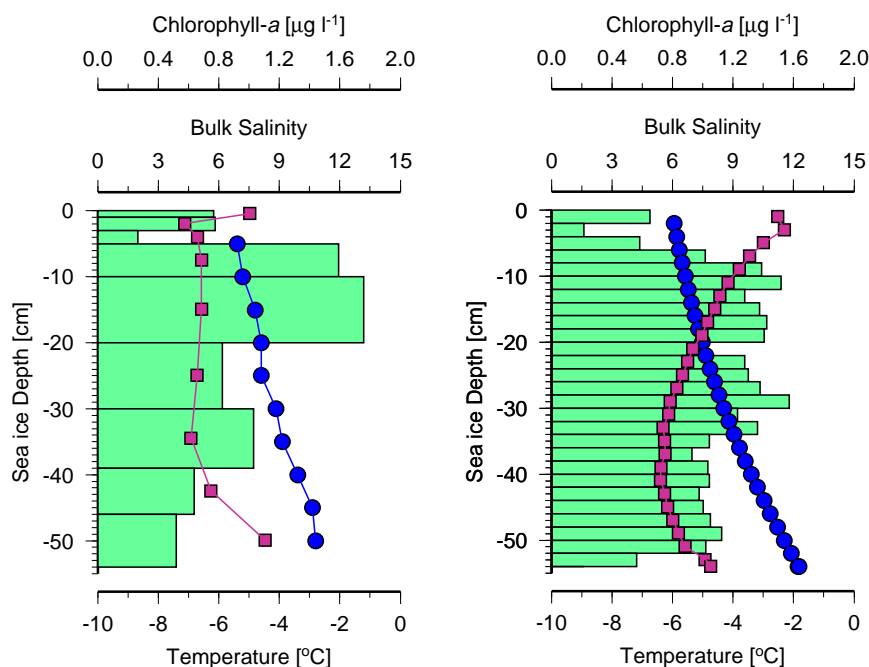


Figure 5.7: Observed (left) and simulated (right) vertical sea ice profiles for core #3 showing the temperature (circles), salinity (squares) and chlorophyll-*a* (bars).

These differences are caused by the vertical position of the impermeable layer. As discussed in Chapter 4, the ice is practically impermeable when the brine volume drops below 50 ppt (see Fig. 4.2) and the vertical flux of brine is interrupted. Since the flux of brine

is a function of the vertical gradients of temperature and salinity, the comparatively higher simulated ice salinities induce some degree of permeability in the upper 30 cm ice layers, allowing the flux of biological material to the layers below. In the observed vertical salinity profile, the ice is already impermeable at 20 cm depth. Differences between the simulated and observed vertical Chl-*a* profiles for this core are caused mostly by short-term pulses in the brine flux and consequently, the vertical redistribution of biological material. These fluctuations are governed by changes in the air temperature and, consequently, in the heat conduction within sea ice (Fig. 5.8).

There was no simulated primary production in the core #3, as the ice floe remained in the dark for the whole period of drift. Therefore, core #3 is a good example of how the thermodynamic ice growth affects the vertical distribution of biological material. Daily variations in the integrated chlorophyll-*a* for this core (not shown) were related only to the accumulation of biological material during ice growth. Core #2 showed similar characteristics to core #3 in both vertical profiles and the thermodynamic history, and therefore will not be shown.

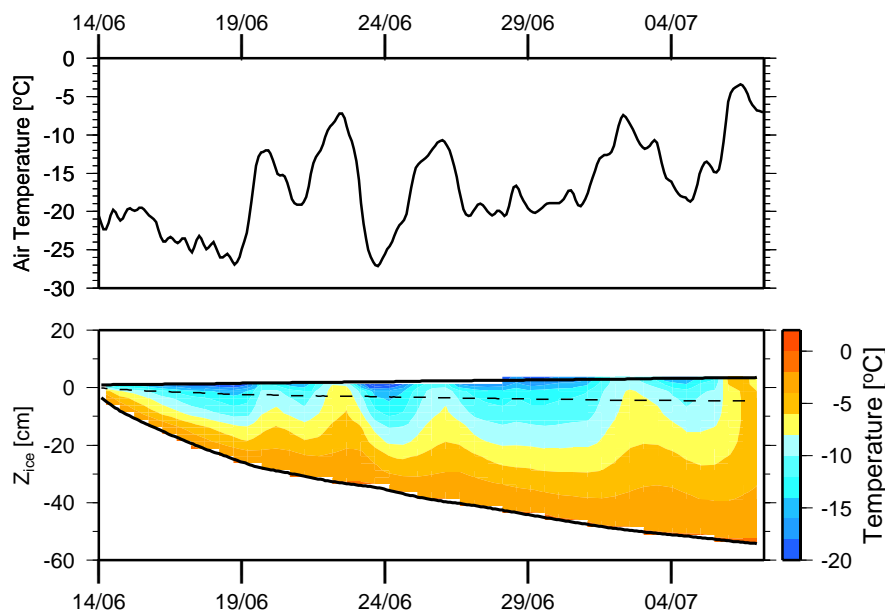


Figure 5.8: Time series of air temperature (top) and simulated vertical profile of snow and sea ice temperatures during the drift of core #3. The dashed line marks the relative seawater level.

Cores #4 to #8 differ significantly from the first ones because they drift in the north-northeast direction, accompanying the main offshore ice velocity field in the Weddell Sea. Cores #4 and #5 showed similar growth patterns, ice thicknesses and float trajectories (Table 5.2 and Fig. 5.2). However, their final integrated chlorophyll-*a* biomass is different, probably

due to differences in the chlorophyll-*a* concentrations in the water column during the initial stages of ice formation. Core #4 was formed near the shore, when phytoplankton blooms are commonly observed in late summer [Sullivan *et al.* 1993]. It showed a final integrated Chl-*a* of $2.26 \text{ mg Chl-}a \text{ m}^{-2}$, almost 20 times greater than core #5 ($=0.12 \text{ mg Chl-}a \text{ m}^{-2}$) which was formed in more offshore conditions. The similar vertical profiles of temperature and salinity for both cores (not shown) indicate that they experienced the same thermodynamic events, with a rapid ice formation and growth followed by a period of slow bottom congelation. Figure 5.9 shows the vertical profile of observed and simulated ice properties for core #4.

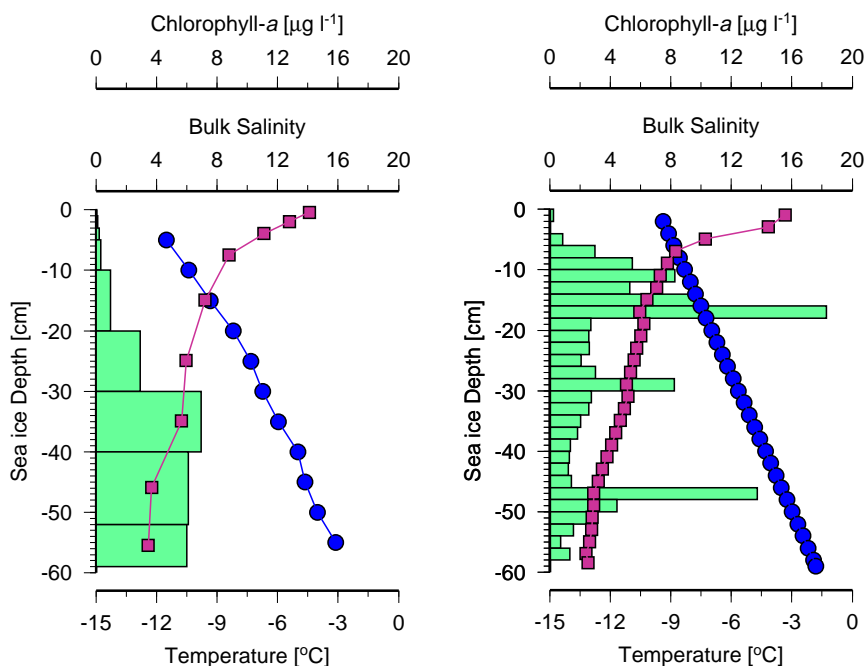


Figure 5.9: Observed (left) and simulated (right) vertical sea ice profiles for core #4 showing the temperature (circles), salinity (squares) and chlorophyll-*a* (bars).

The maximum chlorophyll-*a* peak in the core #4 is located at the last 30 cm near the bottom ice layers, showing a relatively low *bias* (-0.10). Nevertheless, care must be taken when comparing observed and simulated chl-*a* profiles in Fig. 5.9. Although the apparent discrepancy between the chl-*a* peaks, one must remember that the observed chl-*a* biomass is measured at core sections with 10 cm thickness (Fig. 5.9, left) while the model vertical spacing $\Delta z=2 \text{ cm}$ (Fig. 5.9, right). Averaging the simulated chlorophyll-*a* biomass in the same sections that the observed core results in similar values and therefore, a relatively low *bias*. Temperature differences in the first 20 cm between observed and simulated cores also affect the vertical distribution of chlorophyll-*a* by setting a different vertical position of the

impermeable layer.

The final observed ice temperatures for core #4 are slightly lower than the simulated profile in the top layers, indicating that the ice floe may have experienced more stable conditions than those simulated. Nevertheless, the air temperature time series used to force the model (not shown) was characterized by short term fluctuations (< 3 days) with temperature rises from -25°C to -5°C . Small spatial oscillations in the model forcing terms (air temperature, snow cover and oceanic heat flux) may be the source of the differences in the simulated and observed vertical ice profiles

Cores #6 and #7 drifted in the northeast direction during approximately the same number of days (87 and 89 days, respectively). Contrary to the other cores, they experienced an extended light period during the first 40 days and, also during the last 10 days of drift, being only about 30 days in the dark. The computed *bias* from observed and simulated final vertical chl-*a* profiles shows a value of -0.08 for core #6 and -0.29 for core #7, with both cores showing two chl-*a* peaks: one at interior layers (between 20 and 30 cm depth) and a second one in the last 15 cm near the bottom ice boundary (core #6, Fig. 5.10).

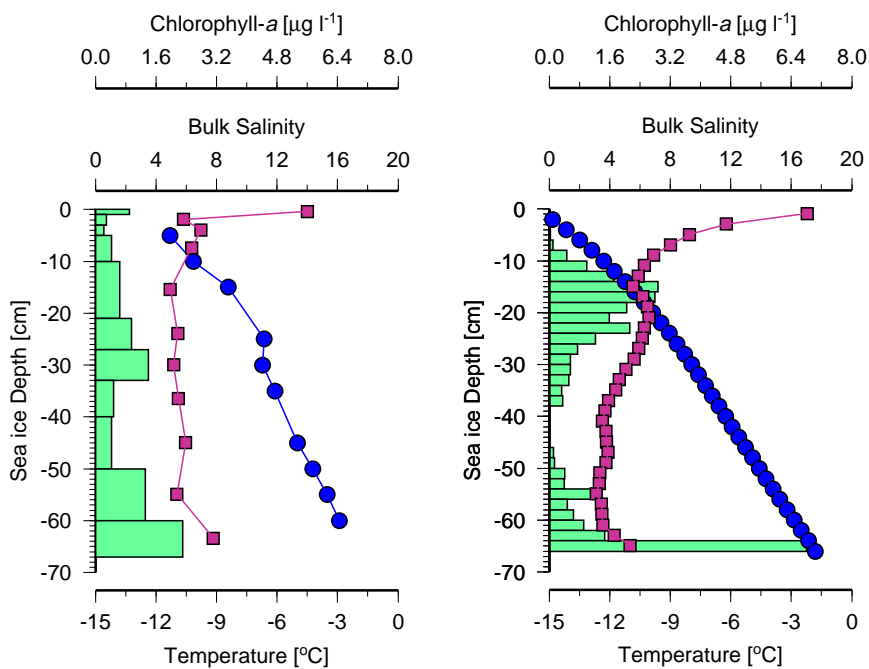


Figure 5.10: Observed (left) and simulated (right) vertical sea ice profiles for core #6 showing the temperature (circles), salinity (squares) and chlorophyll-*a* (bars).

The salinity profiles have the characteristic C-shape, as observed in cores #2 and #3, with a small discontinuity at 15 cm depth in ice, associated with a 6-day long warm period with

air temperatures around -2°C between April 22th to 28th (Fig. 5.11, top). During this time, basal melting and enhanced brine flux due to warming ice temperatures (Fig. 5.11, bottom) contributed to salt fractionation and consequently, changes in the sea ice salinity profile.

If the brine flux is increased, the vertical redistribution of biological material is strongly affected due to brine drainage. In the same period, the vertical distribution of chlorophyll-*a* showed a clear accumulation pattern in the bottom most layers, followed by a loss in the total biomass due to bottom melting (Fig. 5.12).

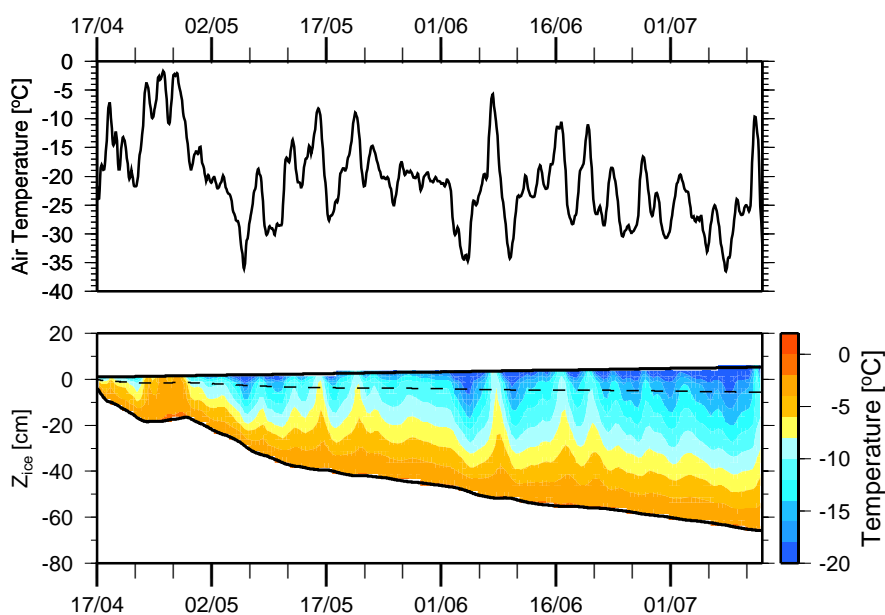


Figure 5.11: Time series of air temperature and simulated vertical profile of snow and sea ice temperatures during the drift of core #6. The dashed line marks the seawater level.

Daily net primary production decrease from $3.5 \text{ mg C m}^{-2} \text{ day}^{-1}$ to negative values (Fig. 5.13) accompanying a decrease in the incoming solar radiation (not shown). After drifting for one month, the ice floe entered the dark polar night and at this time grazing becomes evident (Fig. 5.13). Small fluctuations observed in the daily variation of integrated chl-*a* are due to oscillating ice growth rates caused by thermodynamic effects in the sea ice heat conduction.

The simulated drift of core #8 showed a clear eastward direction during 60 days, accompanying the northern boundary of the Weddell Gyre (Fig. 5.2). Due to its zonal position ($\approx 63^{\circ}\text{S}$), incoming solar radiation was available for the whole period of drift, ranging from 10 to 80 W m^{-2} at local noon (≈ 2.5 to $20 \mu\text{mol photons m}^{-2} \text{ s}^{-1}$). Air temperatures were higher than in other regions (Fig. 5.14), however with stronger fluctuations between the

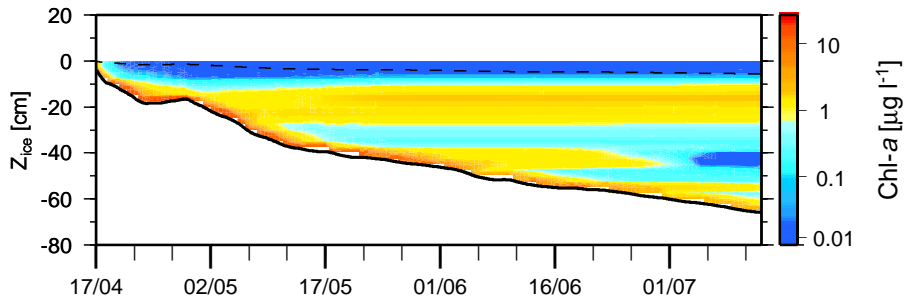


Figure 5.12: Simulated time evolution of the sea ice vertical chlorophyll-*a* profile of core #6.

coldest mark of -35°C on June 5th, rising to 0°C in only five days.

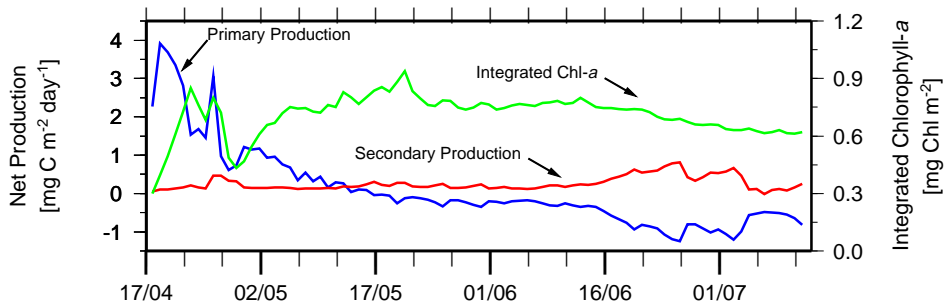


Figure 5.13: Simulated daily integrated chlorophyll-*a* (green), net primary production (blue) and net secondary production (red) for core #6.

The simulated and observed vertical profiles of chlorophyll-*a* showed a satisfactory correspondence (Fig. 5.15) indicated by a very low *bias* (-0.04). However significant differences in the topmost layers suggest that the higher simulated salinities in the first 15 cm may be related to higher ice growth rates at the initial stages of ice formation. This discrepancy may be responsible for an effective accumulation of biological material in the simulated core which was not observed in the sampled ice core.

The daily net primary production for this core decreased from $0.9 \text{ mg C m}^{-2} \text{ day}^{-1}$ to zero in the first 30 days, following the decrease of solar radiation in the period. Around June 25th, when the solar light begins to increase again, ice temperatures as low as -15°C in the first 40 cm near the top (not shown) limited the sea ice primary production (Fig. 5.16).

5.2.1 Productivity and Nutrient Dynamics

The time evolution of the C:Chl-*a* ratio together with the nutritional status of the sea ice community, are essential parameters to relate chlorophyll-*a* biomass measurements in sea ice to primary production. Photosynthesis versus irradiance relationships for Antarctic sea

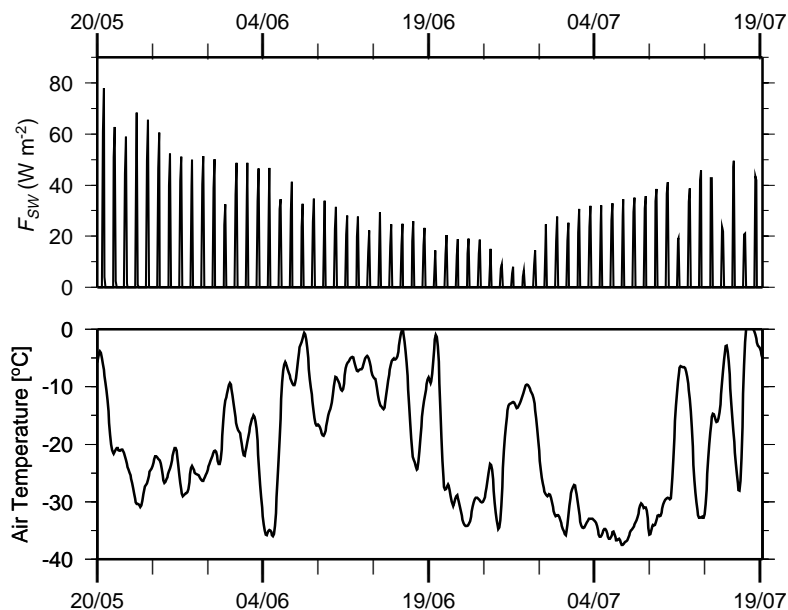


Figure 5.14: Time series of incoming solar radiation (top) and air temperature (bottom) during the drift of core #8.

ice microalgae were relatively well studied by many authors [Barlow *et al.* 1988, Cota and Sullivan 1990, Lizotte and Sullivan 1992, Thomas *et al.* 1992]. However, the photoacclimation mechanism is not well understood, since the broad range of transient light conditions found in the pack-ice hampers the extrapolation of experimental results to the environment.

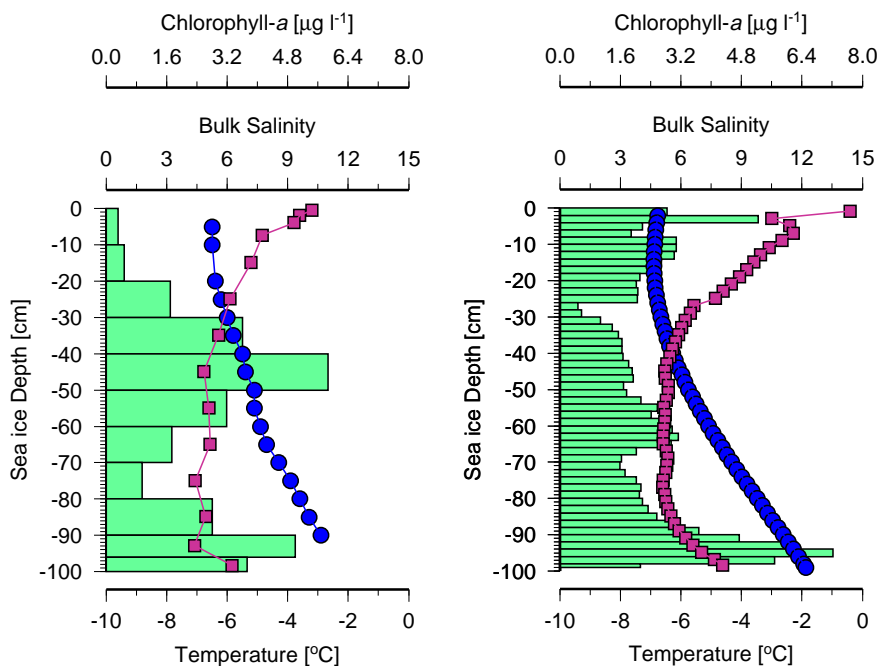


Figure 5.15: Observed (left) and simulated (right) vertical sea ice profiles for core #8 showing the temperature (circles), salinity (squares) and chlorophyll-a (bars).

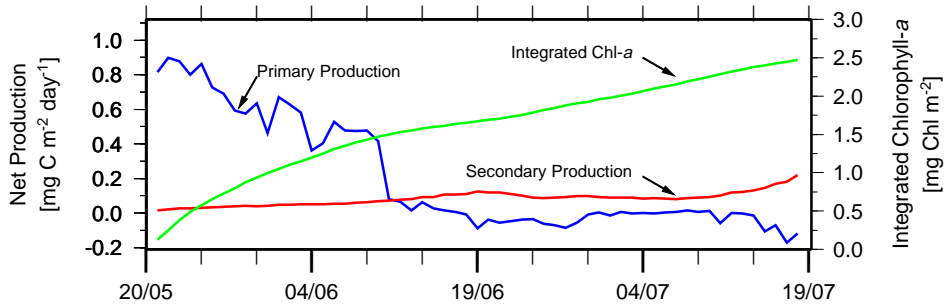


Figure 5.16: Simulated daily integrated chlorophyll-*a* (green), net primary production (blue) and net secondary production (red) for core #8.

The degree of photoacclimation in sea ice microalgae can be asserted from the simulated ice cores through the analysis of the chlorophyll-*a* to carbon ratio. The model assumes a Chl-*a* :C ratio of $0.01 \mu\text{g } \mu\text{g}^{-1}$ ($\equiv \text{C:Chl-}a \text{ of } 100 \mu\text{g } \mu\text{g}^{-1}$) for each new accreted ice layer, and uses the photoacclimation mechanism described in Chapter 2 to freely vary the chl-*a* to carbon ratio during the simulation. Figure 5.17 shows the frequency distribution of the Chl-*a* :C ratio taken from the time-series of biological variables of simulated cores. The values deviate from the initial ratio reaching up to $0.02 \mu\text{g Chl-}a (\mu\text{g C})^{-1}$ (equivalent to a C:Chl-*a* ratio of $50 \mu\text{g } \mu\text{g}^{-1}$).

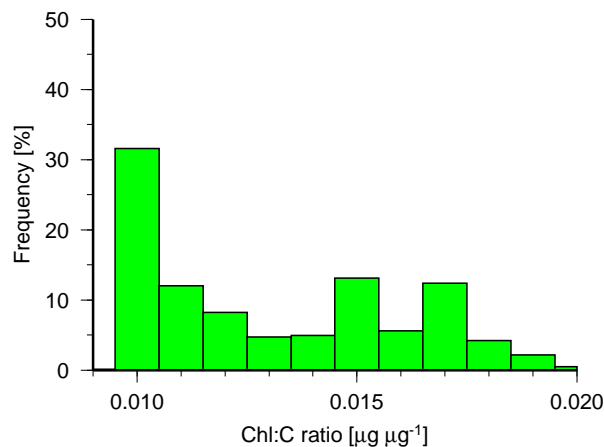


Figure 5.17: Frequency histogram of Chlorophyll-*a* to carbon ratio from simulated ice cores.

High values of Chl-*a* :C ratio are expected since the ice cores were taken between June and July in the pack-ice. During the winter, when the incoming solar light decreases, photoacclimation of sea ice microalgae is enhanced, as described in the Chapter 2, subsection 2.2.2. Thomas *et al.* [1992] found values of up to $0.035 \mu\text{g Chl-}a (\mu\text{g C})^{-1}$ (equivalent to $28 \mu\text{g C } (\mu\text{g Chl-}a)^{-1}$) in experiments with a small Antarctic *Chaetoceros* species, suggesting that during the winter, sea ice microalgae must reach their maximum degree of photoaccli-

mation, with the lowest values of C:Chl-*a* ratio.

The nutrient status in sea ice for the simulated cores also showed the expected variability attributed to the biological activity. The simulated dissolved nutrients in the brine is a function of the bulk salinity (section 4.2.1, Chapter 4). It means that changes in relationship between ice salinity and nutrients are directly related to biological processes in the model. Figure 5.18 shows the distribution of nutrients in sea ice as a function of the ice bulk salinity from all cores. Note that dissolved inorganic nitrogen is clearly depleted along the whole range of ice salinities, while silicate shows a more conservative pattern. Concentrations above the line for dissolved nitrogen (Fig. 5.18, left) are attributed to excretion of nitrogen from protozoan activity. This distribution is very similar to observations made by Dieckmann *et al.* [1991b] on young sea ice in the Weddell Sea, although they related these high nitrogen concentrations to problems in the sample manipulation.

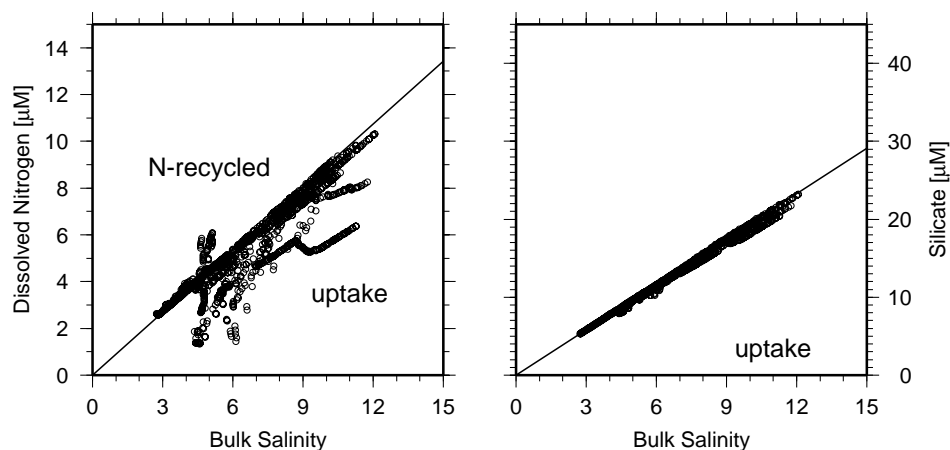


Figure 5.18: Simulated dissolved nitrogen (left) and silicate (right) as a function of the bulk sea ice salinity. The solid lines represent the expected nutrient concentration from dilution of seawater, as described in the section 4.2.1, Chapter 4. Data points below the line are due to microalgal uptake and DIN values over the line are due to N-recycling.

The integrated daily net primary production for the simulated ice cores (Figure 5.19) showed values ranging from 2 to 8 mg C m⁻² day⁻¹ in March, decreasing to < 4 mg C m⁻² day⁻¹ in April-May and negative net production rates in June and July. Negative values result from microalgal carbon loss due to grazing. Similar values were found during 3 winter cruises in the Antarctic pack-ice [Lizotte and Sullivan 1992], indicating that the model can well represent the sea ice primary production and nutrient dynamics during the onset of the pack-ice growth season.

The predicted sea ice production and its decline during the winter is governed mainly by

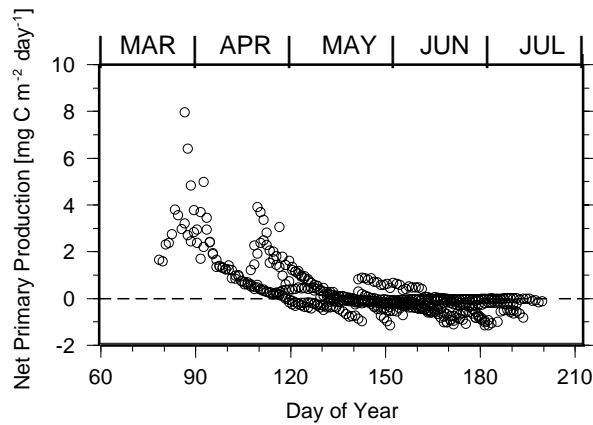


Figure 5.19: Daily net primary production for simulated ice cores.

light and temperature, since nutrients and grazing presented relative normal levels for young first-year sea ice. Lizotte and Sullivan [1992] also found that although the low temperature commonly found in most of the pack-ice during the autumn, the solar light play a key role determining the magnitude of the biomass-specific primary production P^* (the rate of carbon production per chlorophyll-*a* biomass given in $\text{mg C (mg Chl-}a\text{)}^{-1} \text{ day}^{-1}$).

Figure 5.20 shows the distribution of P^* calculated over the daily primary production rates and the chlorophyll-*a* biomass. The irradiance $\text{PAR}^{\text{ice}+}$ is the photosynthetically available radiance at the snow-ice interface. These values are in good agreement with *in situ* measurements in the pack-ice [Kottmeier and Sullivan 1987, Garrison and Buck 1991], suggesting that during the winter sea ice production is possible, even probable, although the low light levels under the snow cover.

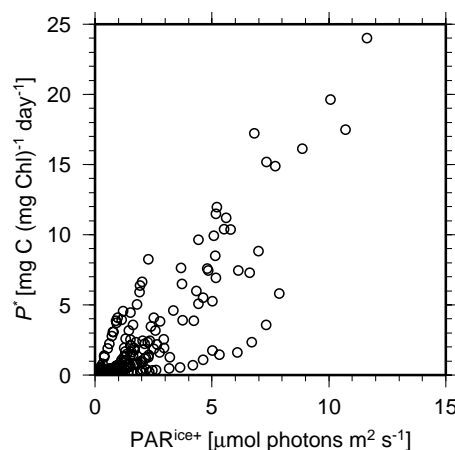


Figure 5.20: Biomass-specific primary production (P^*) versus the irradiance at the snow-ice interface ($\text{PAR}^{\text{ice}+}$) for Simulated ice cores.

One weakness in the previous estimates of sea ice primary production is that the biolog-

ical models employed do not consider the winter months [Lizotte 2001]. Although most of the pack-ice is in the dark polar night between June and August, part of the ice-edge still receives solar radiation, the most important condition for the photosynthesis and biological production in sea ice (see Chapter 3).

Chapter 6

Estimates of the Sea Ice Primary Production for the Weddell Sea

Although our understanding of the biological and physical processes in sea ice is improving, supported by model results which are consistent with field observations, little is known about the large-scale distribution of the pack-ice primary production and its contribution to the total Southern Ocean productivity. In Chapter 5, it was demonstrated that the drift of sea ice plays a key role in determining the thermodynamic history of the ice floes, which in turn strongly influences the associated biological communities. Physical and biological processes of individual floes must be taken into account when estimating the total sea ice biological productivity at regional scales. Using the coupled physical-biological model described in the last chapters, it is possible to simulate individual ice floes distributed over the whole Weddell Sea, thereby assessing the regional patterns of the sea ice productivity.

6.1 The Distribution Sea Ice Properties at Regional Scales

Time-series of ice floe positions in the Weddell Sea were generated using sea ice concentrations obtained from the SSM/I sensor (see Appendix A) between March 1992 and February 1993 and the ice velocity fields from the BRIOS-2 model. Individual ice floes were initialized at every 2° of latitude and longitude in intervals of 10 days. Their positions were traced backward in time, as described in Chapter 5, and floes that drifted for less than 15 days were discarded. A total of 7600 time-series of floe positions were obtained, distributed over the whole Weddell Sea and covering all seasons. The coupled biological-physical model was then used to simulate the time evolution of physical and biological sea ice variables in all individual ice floes, forced with atmospheric and oceanic climatological datasets, as described in the Appendix A. Nutrient concentrations in the water column were fixed to $30 \mu\text{M}$

DIN and $65 \mu\text{M Si(OH)}_4$ [Dieckmann *et al.* 1991b], and the salinity of the seawater to 33.5 [Olbers *et al.* 1992]. These data were used in the initialization of new accreted ice layers as described in Chapter 4.

Variations in snow cover for each ice floe were simulated through daily estimates of snow thickness derived from satellite observations (see Appendix A). The satellite grid has an area of 625 Km^2 which smooths sub-pixel variability [Markus and Cavalieri 1998]. Consideration of the influence of such variability in the sea ice primary production were discussed in detail by Arrigo *et al.* [1998], who proposed the use of a weighted sub-pixel splitting scheme to overcome this problem. However, the main source of snow thickness variability at regional scales is caused by horizontal *inter-pixel* gradients, as pointed out by [Markus and Cavalieri 1998]. Considering ice drift, this variability is explicitly accounted in the sea ice model.

Daily estimates of biological variables (e.g. chlorophyll-*a* biomass, primary production, nutrients) and physical parameters (e.g. ice thickness, salinity, temperature and solar radiation) were obtained from the individual simulations and their spatial distribution were used to produce regional maps of physical and biological processes in the Weddell Sea. To verify the consistency of model results, a comparison with field observations was made.

6.1.1 Sea Ice Algal Standing Crop in the Weddell Sea

Before the advent of biological models, most of the estimates of the sea ice primary production were based upon standing crop and productivity data obtained in field campaigns. However, a complete dataset joining all information available (e.g. sea ice texture, temperature and salinity profiles, chlorophyll-*a* concentrations, nutrients) is still lacking, despite the numerous sea ice cruises carried out in the Antarctic pack-ice in the last 30 years.

Dieckmann *et al.* [1998] compiled the available data on sea ice algal standing crop from the Weddell Sea, based on observations of ice thickness, texture and chlorophyll-*a* biomass made during 10 cruises between 1983 and 1994. They found a strong seasonal variability in the standing stocks of sea ice algae, ranging from 0.05 to $50 \text{ mg Chl-}a \text{ m}^{-2}$ (Fig. 6.1, bottom). The Chl-*a* biomass is poorly correlated with other parameters such as the ice thickness (Fig. 6.1, top). However, some trends are perceptible with higher standing stocks measured during the summer, when the maximum biological activity is expected. In the same way, the vertical integrated chl-*a* biomass is relatively higher in sea ice cores longer than one meter. The

lowest standing stock was recorded during the winter, as well as increasing chl-*a* biomass during spring and early summer. The wide range of ice regimes, floe ages and variable ice thickness, collected during all cruises are the main source of the high variability in the data.

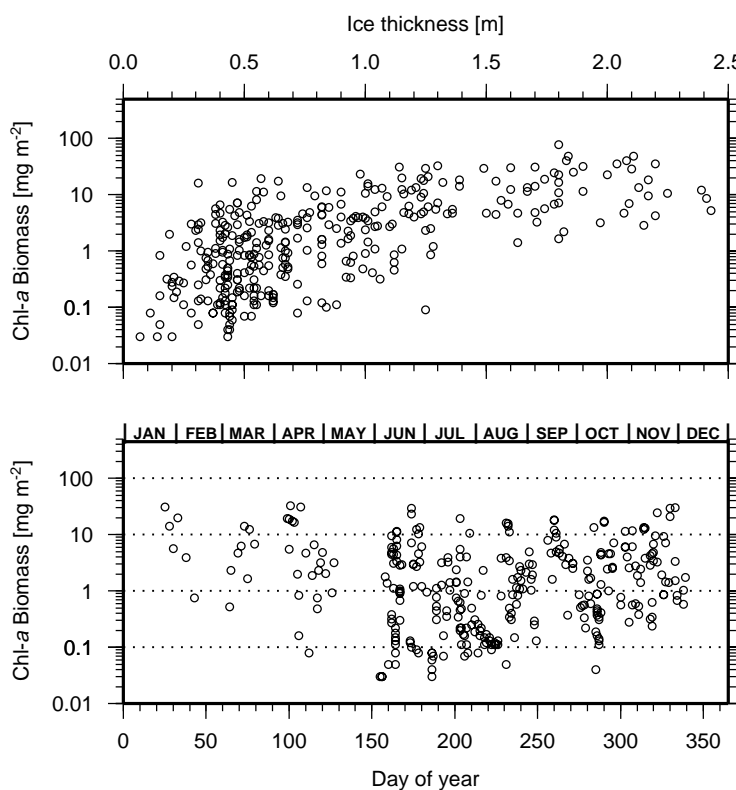


Figure 6.1: Relationship between the vertical integrated chl-*a* biomass and ice thickness (top) and the day of year (bottom) from 439 sea ice cores collected during 10 expeditions in the Weddell Sea. Data from [Dieckmann *et al.* 1998].

Monthly means of the vertical integrated chlorophyll-*a* biomass, ice thickness, sea ice nutrients and the Chl-*a*:C ratios from all 7600 simulated cores were compared with the observations above. Similar trends are noticeable in both datasets when the chl-*a* standing stocks are averaged over monthly intervals (Fig. 6.2). Higher values of vertical integrated chl-*a* biomass are observed in the summer with a significant decrease between March and June. During winter, simulated and observed microalgal standing crop showed a good agreement, with a subsequent increase in the chl-*a* biomass between August and December. Differences between observed and simulated chl-*a* biomass in January-March are mainly due to the low number of observations. While a few ice cores were collected in this period, model results are averaged over a large number of simulated ice floes. However, the similarity between observed and simulated values indicates that the model can well represent the seasonal variation of the integrated chlorophyll-*a* biomass in the Antarctic pack-ice.

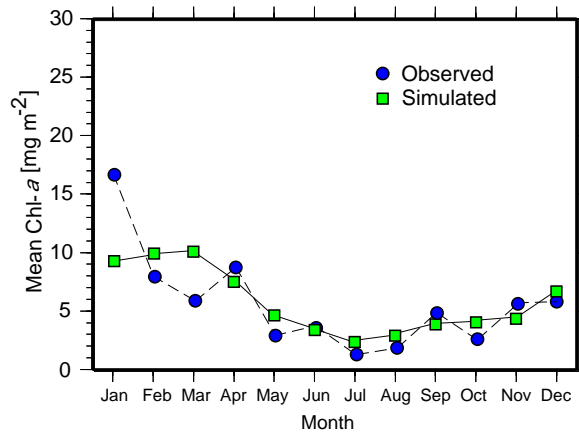


Figure 6.2: Monthly means of vertical integrated chl-*a* derived from sea ice cores (circles) and model results (squares) for the Weddell Sea.

The distribution frequency of the vertical integrated chl-*a* biomass from simulated ice floes (Fig. 6.3) shows that in the autumn, when the ice growth season starts, the dominant range of chl-*a* biomass is <2 mg Chl-*a* m⁻² with small contribution of older ice floes containing higher biomass (Fig. 6.3, bottom right). During the winter, 65% of the simulated chl-*a* biomass is still in the range 0-2 mg Chl-*a* m⁻², however with a significant increase in the frequency of higher chl-*a* biomass values (Fig. 6.3, top left). In the spring, the frequency of chl-*a* biomass in the range 2-10 mg Chl-*a* m⁻² clearly increases (Fig. 6.3, top right) reaching a balanced distribution in the summer (Fig. 6.3, bottom left).

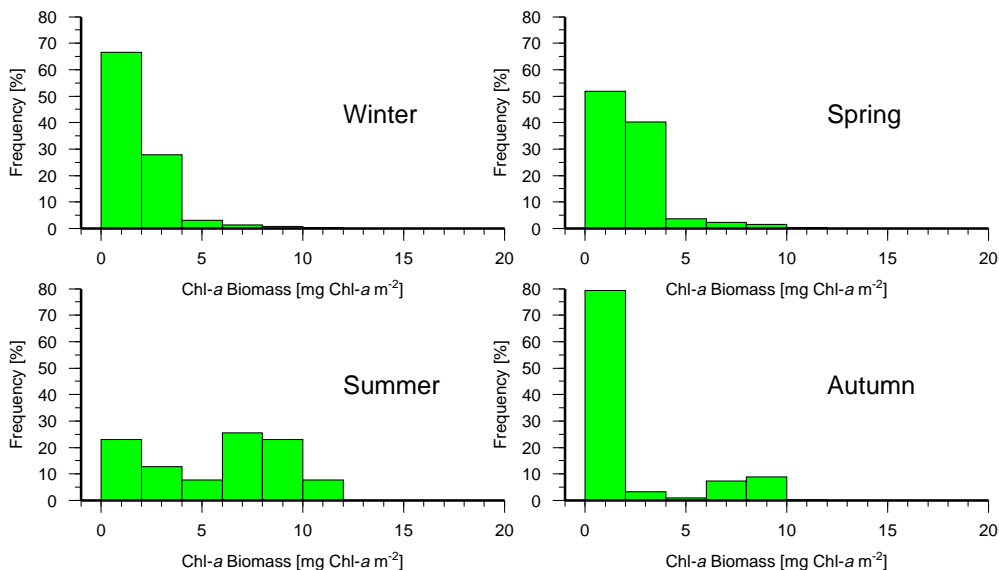


Figure 6.3: Seasonal frequency distribution of the vertical integrated chl-*a* biomass from simulated ice cores in the Weddell Sea.

Some attempts to estimate the total sea ice productivity were made in the past using

monthly means of microalgal chlorophyll-*a* standing crop converted to carbon biomass [Smith Jr. and Nelson 1991, Legendre *et al.* 1992, Smith *et al.* 2001]. However, the major constraint in this approach is the lack of measurements of C:Chl-*a* ratios in the sea ice. Variable physiological conditions experienced by sea ice microalgae may change the C:Chl-*a* ratios from 30 to 100 $\mu\text{g } \mu\text{g}^{-1}$. However, the inverse ratio (Chl-*a*:C) is a diagnostic variable in the model, as described in Chapter 2 and by analyzing the monthly means of the Chl-*a*:C ratio computed from the simulated ice floes, a clear seasonal cycle can be observed (Fig. 6.4).

As expected, the Chl-*a*:C ratio in the topmost ice layers are lower than for the bottom-most layers. Bottom ice communities must photoacclimate since the incoming solar radiation decreases almost exponentially through the sea ice (see Chapter 3). Between November and March, the Chl-*a*:C ratio in the topmost layers ranges from 0.012 to 0.017 $\mu\text{g Chl-}a (\mu\text{g C})^{-1}$ (equivalent to 58-83 $\mu\text{g C } (\mu\text{g Chl-}a)^{-1}$) increasing to 0.023 $\mu\text{g Chl-}a (\mu\text{g C})^{-1}$ (equivalent to C:Chl-*a* ratio of 43) during the winter. However, the Chl-*a*:C ratio at the bottom-most layers are notably higher (ca. 10-15%) than for the topmost ice layers. In early spring, when levels of solar radiation within sea ice increase again, the sea ice communities start to modulate their light harvesting complex and the Chl-*a*:C ratio decreases. However, this trend is not so pronounced in the bottom-most layers. The reason for these differences may be related to shadowing effects caused by the high concentrations of chl-*a* in the ice layers above during this period [Ackley and Sullivan 1994].

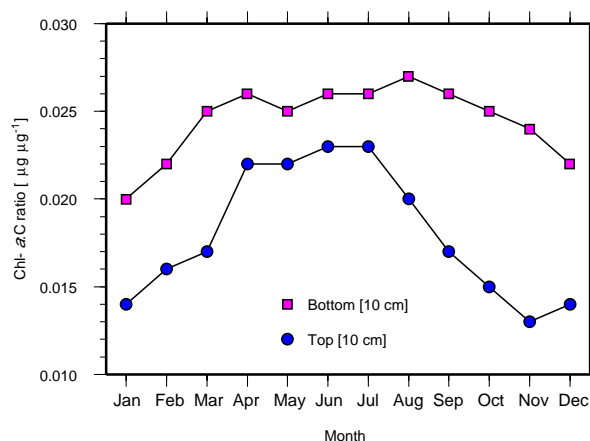


Figure 6.4: Monthly means of the Chl-*a*:C ratio for the topmost 10 cm layers (circles) and bottom-most 10 cm layers (squares) of ice obtained from simulated floes in the Weddell Sea.

Nutrients in sea ice also show a strong variability during all seasons. Dissolved inorganic nitrogen and silicate became very depleted due to the increasing demand in the late spring

and early summer. Figure 6.5 shows the status of nutrients in the simulated ice floes in relation to the bulk salinity in the late spring-early summer, at the end of the ice growth season. Since the model assumes constant values of seawater salinity and nutrients to initialize new accreted ice layers (see Chapter 4), the deviation from the dilution values, represented by the solid line in Fig. 6.5, can be only resulted from biological activity. Dissolved inorganic nitrogen (Fig. 6.5, left) shows a distribution similar to that found in ice cores collected in the Weddell Sea [Dieckmann *et al.* 1991b]. High values of DIN associated to ice with low bulk salinity may result from N-excretion, indicating that the protozoa herbivory plays a key role in the nutrient dynamics in sea ice. Silicate also appears to be depleted, although its concentrations are more widespread in the range of observed ice salinities.

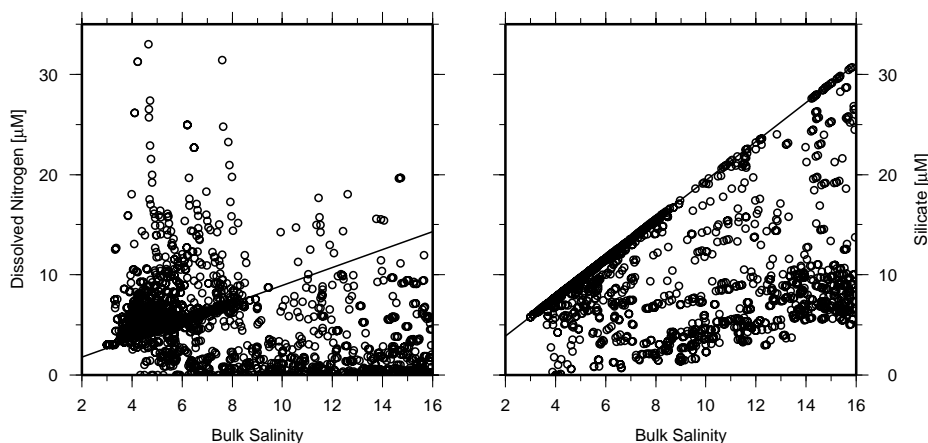


Figure 6.5: Status of dissolved inorganic nitrogen (left) and silicate (right) in function of sea ice bulk salinity at the end of the ice growth season.

As discussed in Chapter 4, the nutrient dynamics in sea ice is linked with the vertical flux of brine, and therefore, depending on thermodynamic processes that control brine drainage. Since the most dominant salinity distribution found in the first-year ice in the Weddell Sea shows a C-shape profile [Eicken 1992], higher bulk salinities are expected to be found in the top- and bottom-most ice layers, while interior layers show relatively lower bulk salinities. Analyzing the nutrient distributions in the Fig. 6.5, one recognizes that the highest values of DIN are observed at low ice salinities suggesting enhanced biological activity at interior ice layers. Gleitz *et al.* [1995] made similar observations in the Weddell Sea, indicating that the model are representing the nutrient dynamics in sea ice with relatively good accuracy. The regeneration of nitrogen and silicate in sea ice is also related to the bacterial activity [Kottmeier and Sullivan 1987, Grossmann and Dieckmann 1994, Arrigo *et al.* 1995]. How-

ever, bacterial production and nutrient regeneration in sea ice still need further investigation.

6.2 Estimates of the Sea Ice Biological Production

The annual rate of biological productivity within the Antarctic sea ice is a function of both the sea ice extent and the rate of carbon production per unit surface area. Estimates of monthly means of sea ice productivity were made using the simulated ice floes. In the model, the net primary production (i.e. the difference between microalgal photosynthetic carbon assimilation and grazing) is used to estimate the daily areal sea ice biological productivity. Monthly means of sea ice primary production (Fig. 6.6) shows a strong seasonal variability with the greatest values observed between December and February, when light and temperature conditions in the sea ice are considerably enhanced compared to the winter.

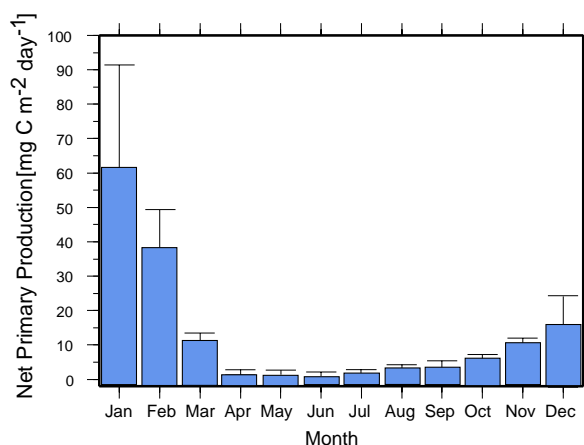


Figure 6.6: Monthly means and standard deviation of the net primary production computed from daily microalgal carbon production in simulated ice floes.

The abrupt decline of the sea ice biological productivity from February to March is mainly caused by the strong retreat of the ice in this period and the relative amounts of new and old ice. Most of the seasonal ice disappears by the end of the summer and the biological production is constrained to the persistent ice fields in the western Weddell Sea. The sea ice productivity computed with the coupled biological-physical model is representative over the large number of sea ice habitats in the pack-ice, and, therefore, the observed variability in the seasonal sea ice cycle has a significant impact on the associated biological communities. Using this information plus the monthly sea ice extent, the total annual sea ice productivity can be estimated (Table 6.1).

Table 6.1: Total extent of the pack-ice and the associated primary production, calculated from simulated ice floes in the Weddell Sea.

Month	Sea ice extent [$\times 10^6$ Km ²]	P. Production [g C m ⁻² month ⁻¹]	P. Production [Tg C month ⁻¹]
January	1.558	1.922	3.0
February	1.021	1.039	1.1
March	1.285	0.341	0.4
April	2.163	0.058	0.1
May	3.313	0.049	0.2
June	4.445	0.050	0.2
July	5.364	0.056	0.3
August	5.834	0.079	0.5
September	5.800	0.109	0.6
October	5.599	0.229	1.3
November	4.836	0.322	1.6
December	2.993	0.519	1.5
Annual Production (Tg C)			10.8

Although during May and September the sea ice primary production contributes only 17% of the total annual sea ice primary production, its importance for the ecosystem should not be underestimated. Most of the pack-ice in this period is practically in the dark. However, a small portion of the pack-ice near the ice edge receives enough solar radiation to sustain biological production as shown in Chapter 3. This sea ice production can reach values of up to 3.6 mg C m⁻² day⁻¹ during the winter, and it is of essential importance for the sea ice ecosystem, specially for the overwintering organisms associated with the pack-ice.

Previous biological sea ice modeling studies considering only near surface communities in the Weddell Sea [Arrigo *et al.* 1997; 1998] determined a comparatively higher estimate of sea ice primary production (15.8 Tg C year⁻¹) for the pack-ice. However, the effects of grazing and the vertical distribution of biological properties were strongly parameterized. On the other hand, these models included a description of infiltration communities (formed due to flooding at the snow/ice interface during heavy snow loading) which are not accounted in the coupled physical-biological model presented here. Little is known about the physical processes governing the heat conduction and brine fluxes in flooded snow layers during the formation of snow ice [Fichefet and Morales Maqueda 1999], making difficult their inclusion in a biological-physical model. The previous estimates did not include the months between May and September, which were shown to be of significantly importance for the Antarctic

sea ice ecosystem.

The results of the sea ice coupled biological-physical model presented many advances to our knowledge about the Antarctic sea ice ecosystem. First, the regional estimates of biological variables, like the chlorophyll-*a* standing crop, Chl-*a*:C ratios, sea ice nutrient status and primary production, showed a good agreement with observed sea ice properties in the Weddell Sea, indicating that the model can be used as an auxiliary tool in studying the ecological aspects of the seasonal cycle of Antarctic sea ice. Second, the use of the self-adapting biological model proved to be of extreme importance when coupling physical and biological processes, allowing a better description of environmental factors that control biological production in sea ice.

Chapter 7

Conclusions and Outlook

In this study, a sea ice coupled biological-physical model was developed to investigate the influence of transient changes in environmental conditions on sea ice biological communities. The biological component of the model includes physiological self-adaptive schemes to simulate microalgal photoacclimation and uptake of dissolved nutrients in response to transient changes of light, temperature and nutrient supply. Grazing is simulated by the incorporation of heterotrophic protists (protozoa) in the model with specific organic carbon and nitrogen pools. The excretion of nitrogen excess by the sea ice protozoa proved to be of importance in sea ice nutrient dynamics. This model is coupled with an one-dimensional thermodynamic sea ice model including a numerical scheme to resolve the heat conduction in sea ice, as well as the incorporation and vertical redistribution of biological material due to brine flux. It was shown that these physical processes play a key role in the vertical structuring of sea ice biological communities and their associated primary production. The inclusion of brine fluxes in the physical model proved that vertical differentiation in the salinity profiles, commonly observed in ice cores collected in the Antarctic pack-ice, results from variable ice growth rates and consequently salt partitioning, which cause distinct bulk salinity profiles. These differences associated with the vertical position of the impermeable layer play a key role in the formation of banded layers where high accumulation of biological material is commonly observed.

The coupled biological-physical model is used in a Lagrangian approach, where the time-dependent position of simulated floes extracted from ice velocity fields are used to compute model forcing parameters (e.g. air temperature, oceanic heat flux, solar radiation). This approach is essential to determine the thermodynamic history of floes and to obtain a good agreement between model results and field observations. During the drift, synoptical changes in environmental conditions lead to a differentiation of vertical sea ice characteristics that

most models do not take into account [Bitz and Lipscomb 1999, Bitz 2000].

One of the most important environmental parameters governing the sea ice primary production is the incoming solar radiation. The model includes the simulation of the spectral solar radiation attenuated by the atmosphere and clouds and a bio-optical sea ice model, determining the vertical distribution of light within sea ice. The solar radiation is also of significant importance for the sea ice thermodynamics, governing the temperature profile within sea ice during the summer months. Simulations with the spectral bio-optical sea ice model showed that part of the marginal pack-ice during the winter receives enough light to support biological production. This fact is of extreme importance for overwintering organisms associated with the sea ice.

Model results showed that the thermodynamic processes controlling ice formation are fundamental in governing the vertical distribution of biological communities. The impermeable layer formed due to vertical temperature gradients and brine segregation acts as a barrier to the flux of biogenic material entrapped in the sea ice. Observed vertical variability in chlorophyll-*a* profiles from collected ice cores in the Weddell Sea are caused mainly by differential incorporation rates of biological material during the ice growth. Figure 7.1 represents the seasonal cycle of the Antarctic pack-ice with emphasis on the physical processes controlling the incorporation and redistribution of biological material within sea ice.

During autumn, dynamic accumulation of microorganisms in the water column due to frazil ice scavenging result in high incorporation rates of biological material within newly accreted ice layers. During winter, the thermodynamic growth of the pack-ice controls the vertical distribution of ice assemblages, mainly due to the effect of brine flux. With the onset of the melting season in spring and summer and increasing solar radiation over sea ice, the biological activity reaches its maximum followed by a rapid decline in the primary production rates between February and March. The sea ice retreat constrains the primary productivity to persistent ice fields in the summer, characterized by nutrient depleted conditions and heavy snow cover, indicating a significant degree of limitation for microalgal production.

The coupled biological-physical sea ice model was used to estimate the total sea ice productivity in the Weddell Sea, showing an annual carbon production of ≈ 11 Tg C. During the winter, the sea ice productivity ranges from 0.16 to 0.6 Tg C month⁻¹, contributing to 17% of the total annual production. These results are lower than previous estimates for the

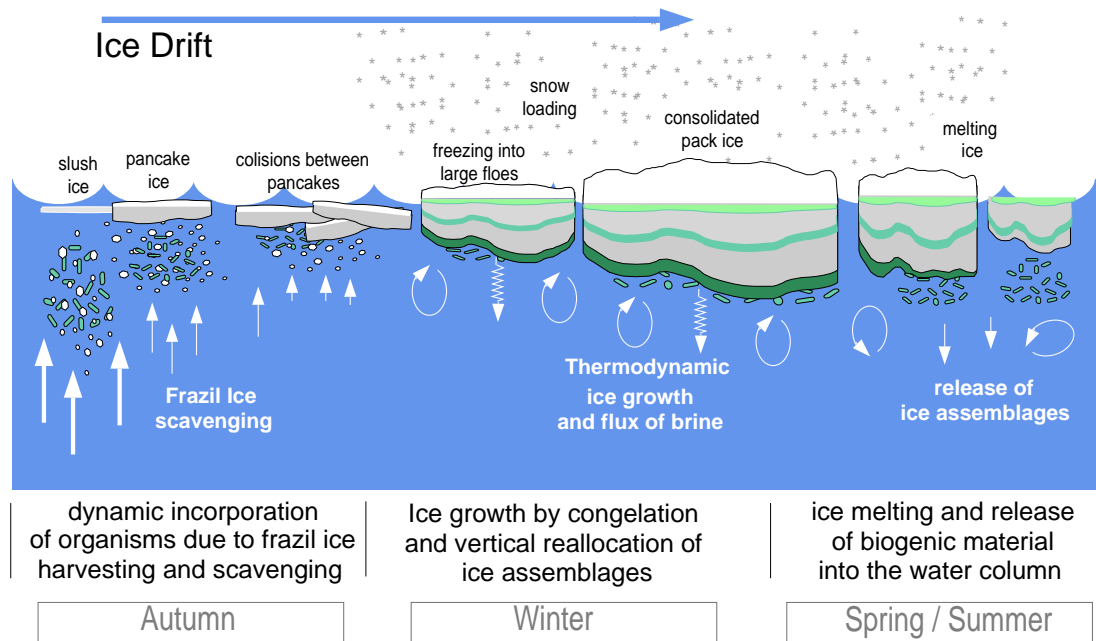


Figure 7.1: Schematic representation of the seasonal cycle of the Antarctic pack-ice, with emphasis on important processes of incorporation of biological material and the physical evolution of sea ice until the melting season.

Weddell Sea pack-ice [Arrigo *et al.* 1998] computed for infiltration communities associated with flooded snow and snow-ice formation [Horner *et al.* 1988, Ackley and Sullivan 1994]. However, the coupled biological-physical sea ice model described here does not consider the formation of snow-ice and, therefore, infiltration communities are not taken into account. Snow flooding is restricted to the later spring/early summer in some areas of the Weddell Sea [Fichefet and Morales Maqueda 1999] and cannot be generalized to the whole seasonal ice zone. Alternatively, most of the ice cores collected in the Weddell Sea indicate that infiltration communities occur in only a small fraction of the pack-ice [Dieckmann *et al.* 1998] and the simulations shown in the Chapter 5 revealed a dominance of interior and bottom ice assemblages.

The ecological distinction between these two assemblages is relevant to understanding the time course of sea ice colonization. Garrison and Buck [1991] found that most of the sea ice infiltration assemblages are contained within a porous layer of hard ice near the freeboard level (i.e. the space between the ice surface and the seawater level) and apparently developed from internal assemblages. They also showed that interior assemblages are apparently established at the time of ice formation and thus overwinter survival in the ice is an important consideration. In contrast, an infiltration assemblage, which is inoculated when flooding

occurs, would be heavily influenced by the composition of the plankton at the time of flooding. The results of simulated ice cores suggest that the surface assemblages are related to the impermeable characteristic of topmost ice layers. However, the low temperatures associated with this vertical level must limit primary production.

Therefore, the estimates of the sea ice primary production in the Weddell Sea obtained by modeling should be considered conservative, since the simulated pack-ice consisted only of first-year ice. Many other ice habitats like multi-year ice, rafted ice floes, refrozen leads, infiltration layers, which are potential sites for the settlement of biological sea ice assemblages were not considered. The contribution of these communities to the total sea ice primary production needs to be further investigated.

Appendix A

Model Forcing Fields and Parameterization

The coupled biological-physical model presented in this work uses a series of forcing fields to simulate the sea ice thermodynamic growth and the time evolution of the associated biological communities. Basically, the required forcing fields are used as input parameters to the thermodynamic and the spectral solar model components. Table A.1 summarizes the forcing variables used in the model and their source.

Table A.1: Forcing variables used in the model and their source. Acronyms are explained in the text.

Variable	Definition	Units	Model component	Source
T_{air}	Air temperature	Kelvin	thermodynamic	NCEP
CL	Cloud cover	tenths	thermodynamic and spectral solar	NCEP
u	Wind speed	m s^{-1}	thermodynamic	NCEP
P_{surf}	Surface air pressure	mb	spectral solar	NCEP
W_{path}	Precipitable water path	atm-cm	spectral solar	NCEP
RH	Relative humidity	tenths	spectral solar	NCEP
β	Atmospherical aerosol turbidity	dimensionless	spectral solar	GACP
α	Aerosol Angstrom exponent	dimensionless	spectral solar	GACP
H_{oz}	Atmospherical Ozone amount	atm-cm	spectral solar	SeaWiFS
A_{ice}	Sea ice concentration	tenths	spectral solar	DMSP-SSM/I
h_s	Snow thickness	cm	thermodynamic	DMSP-SSM/I
\mathcal{F}_{ocean}	Oceanic Heat Flux	W m^{-2}	thermodynamic	BRIOS-2
P_{ocean}^{Chl}	Chl- <i>a</i> concentration in the ocean	$\mu\text{g Chl-}a \text{ l}^{-1}$	thermodynamic	SeaBASS

The atmospherical parameters (air temperature, cloud cover, wind speed, surface air pressure, precipitable water path and relative humidity) are obtained from global NCEP¹ Re-analysis datasets distributed by the National Center for Atmospherical Research (NCAR)

¹NCEP - National Centers for Environmental Prediction

including meteorological observations around the world and modeling data. The global NCEP grid has a spatial resolution of $2.5^\circ \times 2.5^\circ$. The datasets are distributed in annual files written in NetCDF format with temporal resolution of 6 hours. For more details, see <http://www.cdc.noaa.gov>.

Since the air temperature is one of the most important forcing parameters for the thermodynamic model, a comparison between the NCEP datasets and field observations were made. Air temperature observations collected by the meteorological station on board the RV *Polarstern* during the German Antarctic Expedition in 1992 were directly compared with the NCEP Reanalysis data by interpolating ship positions in the global NCEP grid. The absolute difference between the observed air temperature T_{air}^{obs} and the NCEP derived air temperature T_{air}^{NCEP} were plotted against the day of year (Fig. A.1).

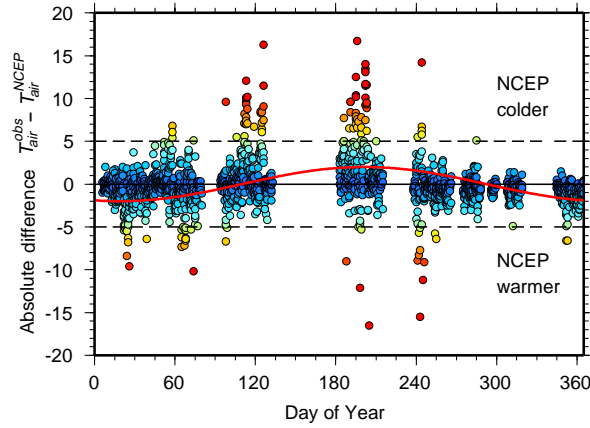


Figure A.1: Seasonal variability of the absolute difference between observed and NCEP derived air temperatures. The solid red line represents the seasonal trend used to correct the NCEP Reanalysis data.

The absolute difference between observed and NCEP derived air temperatures ranged between -5 and 5°C with a clear seasonal trend of $\pm 2^\circ\text{C}$ showing NCEP derived air temperatures relative warmer in the summer and colder during the winter. Most of this variability is caused by the incorporation of global climate models in the NCEP Reanalysis dataset, which over- and underestimate the atmospheric heating due to the solar radiation. This effect is more noticeable at the polar regions due to the seasonal solar cycle. To get corrected values of air temperature to the coupled physical-biological model, a seasonal trend is applied over the NCEP Reanalysis dataset

$$T_{air} = T_{air}^{NCEP} + 2 \sin [2\pi(i - 110)/365] \quad (\text{A.1})$$

where i is the day of year.

Atmospherical aerosol parameters were obtained from the Global Aerosol Climatology Project (GACP). Global distributions of the aerosol Angstrom exponent $\mathring{\alpha}$ and the optical depth at 550 nm $\tau(550)$ based upon satellite and field observations with an original resolution of $1^\circ \times 1^\circ$ resolution were averaged in latitudinal monthly means with a zonal resolution of 1° (Fig. A.2). Since the aerosol turbidity $\mathring{\beta}$ is independent of the wavelength, it was determined from the aerosol optical depth τ_a and the Angstrom exponent $\mathring{\alpha}$ following

$$\mathring{\beta} = \frac{\tau_a(550)}{550^{-\mathring{\alpha}}} \quad (\text{A.2})$$

The atmospherical ozone concentrations were obtained from the climatological dataset of the SeaWiFS Project (Sea-viewing Wide Field-of-view Sensor) based on diverse satellite and meteorological observations around the world.

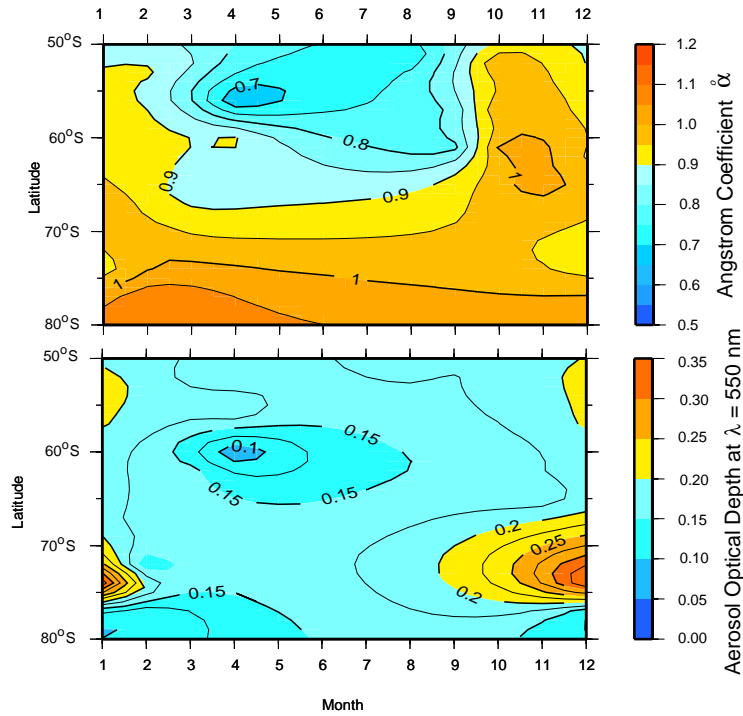


Figure A.2: Climatological data from aerosol Angstrom exponent $\mathring{\alpha}$ (top) and Aerosol optical depth τ_a for 550 nm (bottom) used in the spectral solar model.

The original 9 km daily climatological dataset was averaged in the latitudinal 1° monthly means of total atmospherical ozone in DU (Dobson Unit), as shown in the Fig. A.3. The ozone amount H_{oz} in atm-cm used in Eq. (3.10) is equivalent to the ozone concentration in DU divided by 10.

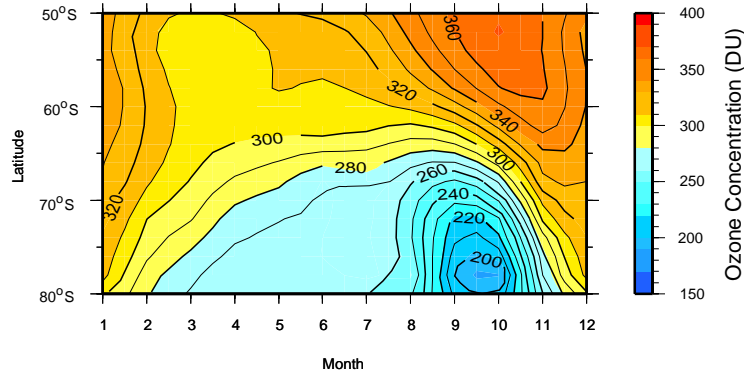


Figure A.3: Climatological data from total atmospherical ozone used in the spectral solar model.

Daily distributions of sea ice concentration and snow thickness were obtained from passive microwave data of the defense meteorological satellite program (DMSP) special sensor microwave/imager (SSM/I), distributed by the National Snow and Ice Data Center (NSIDC). The dataset has a spatial resolution of 25 Km in a polar stereographic grid covering the whole Southern Hemisphere. Passive microwave sensors are unhampered by cloud cover and unaffected by the darkness being very effective for monitoring changing conditions in the Antarctic sea ice cover. Sea ice concentrations are derived from the microwave brightness temperature (TB) polar grid using the NASA Bootstrap algorithm [Comiso 1995] and used to compute the ground albedo in the spectral solar model. Snow thickness are computed from the TB grids using the algorithm from Markus and Cavalieri [1998] and used to calculate the daily snow accumulation rates. The correlation coefficient of both datasets with *in situ* observations averages 0.8 [Markus and Cavalieri 1998]. Daily snow accumulation rates are derived from the time difference between daily estimates of snow thickness interpolated at floe positions. The temperature of the new accumulated snow layers in the coupled biological-physical sea ice model is assumed to be the same of the surface snow/ice.

Another input parameter required by the thermodynamic model is the oceanic heat flux, used to calculate the energy balance at the ice/water interface (see Chapter 4). Since direct measurements of the oceanic heat flux are spatially scarced, a climatological dataset computed from the results of the BRIOS-2 coupled sea ice-ocean model is used [Timmermann *et al.* 2001]. The datasets contains monthly means of oceanic heat flux at the ice/water interface with a spatial resolution of 1.6875° in the zonal and 0.5625° in the meridional directions. Values of \mathcal{F}_{ocean} are interpolated at ice floe positions during the ice drift.

The chlorophyll-*a* concentration in the ocean P_{ocean}^{Chl} , used to initialize the biological

quantities in newly formed ice layers (see Chapter 4), is taken from monthly means of observed surface chl-*a* concentrations distributed over the whole Shouthern Ocean and part of the SeaBASS database (SeaWiFS Bio-optical Archive and Storage System). The SeaBASS database was developed by the NASA Sea-viewing Wide Field-of-view Sensor (SeaWiFS) Project in order to provide *in situ* data for calibration/validation purposes. The database contains ca. 12.000 observations collected using a number of different instruments (e.g. profilers, buoys, optical sensors) covering all seasons and remote sensing data during the late spring and summer months. The whole database was converted in monthly means of surface chlorophyll-*a* concentration projected in a grid with spatial resolution of 5°.

The table A.2 contains the internet links for the institutions that provided the datasets used in this work. Most of these datasets are of public access (except those from the BRIOS-2 model. For details, please contact the authors in the BRIOS home page).

Table A.2: Links to the home pages of the datasets used in this work.

Dataset	Home page
NCEP/NCAR Reanalysis	http://www.cdc.noaa.gov/cdc/reanalysis
GACP Aerosol data	http://gacp.giss.nasa.gov
SeaWiFS Ozone Climatologies	http://seadas.gsfc.nasa.gov
SSM/I passive microwave data	http://www-nsidc.colorado.edu
BRIOS model	http://www.awi-bremerhaven.de/Modelling/BRIOS
SeaBASS database	http://seabass.gsfc.nasa.gov

References

- Ackley, S. F., K. R. Buck and S. Taguchi [1979] Standing crop of algae in the sea ice of the Weddell Sea region. *Deep Sea Research Part 1*, **26A**, 269–281.
- Ackley, S. F. and C. W. Sullivan [1994] Physical controls on the development and characteristics of Antarctic sea ice biological communities - a review and synthesis. *Deep Sea Research Part 1*, **41**(10), 1583–1604.
- Aksnes, D. L. and J. K. Egge [1991] A theoretical model for nutrient uptake in phytoplankton. *Marine Ecology Progress Series*, **70**(1), 65–72.
- Allan, D. J. and D. R. Ort [2001] Impacts of chilling temperatures on photosynthesis in warm-climate plants. *Trends in Plant Science*, **6**(1), 36–42.
- Angström, A. [1961] Techniques of determining the turbidity of the atmosphere. *Tellus*, **XIII**(2), 214–229.
- Aota, Y. and H. Nakajima [2000] Mathematical analysis on coexistence conditions of phytoplankton and bacteria systems with nutrient recycling. *Ecological Modelling*, **135**, 17–31.
- Arar, E. J. and G. B. Collins [1992] *In vitro* determination of chlorophyll *a* and phaeophytin *a* in marine and freshwater phytoplankton by fluorescence. *Technical Report Method 445.0*, USEPA -U.S. Environmental Protection Agency, Cincinnati, OH.
- Archer, S. D., R. J. G. Leakey, P. H. Burkill and M. A. Sleigh [1996] Microbial dynamics in coastal waters of East Antarctica: Herbivory by heterotrophic dinoflagellates. *Marine Ecology Progress Series*, **139**(1-3), 239–255.
- Arrigo, K., D. L. Worthen, P. Dixon and M. P. Lizotte [1998] Primary productivity of near surface communities within Antarctic pack ice. In: *Antarctic Sea Ice: Biological Processes, Interactions and Variability* (edited by Lizotte, M. P. and K. Arrigo), volume 73 of *Antarctic Research Series*, pp. 23–43. American Geophysical Union, Washington, D.C.
- Arrigo, K. R. [1994] Impact of ozone depletion on phytoplankton growth in the Southern Ocean: Large-scale spatial and temporal variability. *Marine Ecology Progress Series*, **114**(1-2), 1–12.
- Arrigo, K. R., G. Dieckmann, M. Gosselin, D. H. Robinson, C. H. Fritsen and C. W. Sullivan [1995] High resolution study of the platelet ice ecosystem in McMurdo Sound, Antarctica: Biomass, nutrient, and production profiles within a dense microalgal bloom. *Marine Ecology Progress Series*, **127**(1-3), 255–268.
- Arrigo, K. R., J. N. Kremer and C. W. Sullivan [1993] A simulated Antarctic fast ice ecosystem. *Journal of Geophysical Research*, **98**(C4), 6929–6946.

- Arrigo, K. R. and C. R. McClain [1994] Spring phytoplankton production in the western Ross Sea. *Science*, **266**(5183), 261–263.
- Arrigo, K. R., D. H. Robinson, D. L. Worthen, R. B. Dunbar, G. R. DiTullio, M. VanWoert and M. P. Lizotte [1999] Phytoplankton community structure and the drawdown of nutrients and CO₂ in the Southern Ocean. *Science*, **283**(5400), 365–367.
- Arrigo, K. R. and C. W. Sullivan [1992] The influence of salinity and temperature covariation on the photophysiological characteristics of Antarctic sea ice microalgae. *Journal of Phycology*, **28**(6), 746–756.
- Arrigo, K. R. and C. W. Sullivan [1994] A high resolution bio-optical model of microalgal growth: Tests using sea-ice algal community time-series data. *Limnology and Oceanography*, **39**(3), 609–631.
- Arrigo, K. R., C. W. Sullivan and J. N. Kremer [1991] A bio-optical model of Antarctic sea ice. *Journal of Geophysical Research*, **96**(C6), 10,581–592.
- Arrigo, K. R., D. L. Worthen, M. P. Lizotte, P. Dixon and G. Dieckmann [1997] Primary production in Antarctic sea ice. *Science*, **276**(5311), 394–397.
- Assur, A. [1958] Composition of sea ice and its strength. In: *Arctic Sea Ice*, number 598 in NRCP, pp. 106–138. National Academy of Sciences, National Research Council Publication, Washington, D.C.
- Astronomical Almanac [1998] The Astronomical Almanac. Edited by the Nautical Almanac Office, Royal Greenwich Observatory.
- Baretta Bekker, J. G., J. W. Baretta, A. S. Hansen and B. Riemann [1998] An improved model of carbon and nutrient dynamics in the microbial food web in marine enclosures. *Aquatic Microbial Ecology*, **14**(1), 91–108.
- Barlow, R. G., M. Gosselin, L. Legendre, J.-C. Therriault, S. Demers, R. F. C. Mantoura and C. A. Lyewellyn [1988] Photoadaptive strategies in sea-ice microalgae. *Marine Ecology Progress Series*, **45**, 145–152.
- Beckmann, A. and R. Timmermann [2001] Circumpolar Influences on the Weddell Sea: Indication of an Antarctic Circumpolar Coastal Wave. *Journal of Climate*, **14**, 3785–3792.
- Bernard, O. and J.-L. Gouzé [1995] Transient behavior of biological loop models with application to the Droop model. *Mathematical Biosciences*, **127**, 19–43.
- Bird, R. E. and C. Riordan [1986] Simple solar spectral model for direct and diffuse irradiance on horizontal and tilted planes at the Earth's surface for cloudless atmospheres. *Journal of Climate and Applied Meteorology*, **25**, 87–97.
- Bitz, C. M. [2000] Documentation of a Lagrangian sea ice thickness distribution model with energy-conserving thermodynamics. *Technical report*, University of Washington.
- Bitz, C. M. and W. H. Lipscomb [1999] An energy-conserving thermodynamic model of sea ice. *Journal of Geophysical Research*, **104**(C7), 15,669–15,677.

- Bjørnsen, P. K. and J. Kuparinen [1991] Growth and herbivory by heterotrophic dinoflagellates in the Southern Ocean, studied by microcosm experiments. *Marine Biology*, **109**, 397–405.
- Bohren, C. [1983] Colors of snow, frozen waterfalls, and icebergs. *Journal of the Optical Society of America*, **73**, 1646–1652.
- Bohren, C. F. and D. P. Gilra [1979] Extinction by a spherical particle in an absorbing medium. *Journal of Colloid and Interface Science*, **72**(2), 215–221.
- Brandt, R. E. and S. G. Warren [1993] Solar-heating rates and temperature profiles in Antarctic snow and ice. *Journal of Glaciology*, **39**(131), 99–110.
- Caron, D., J. Goldman and M. Dennett [1990] Carbon utilisation by the omnivorous flagellate *Paraphysomonas imperforata*. *Limnology and Oceanography*, **35**, 192–201.
- Clarke, D. B. and S. F. Ackley [1984] Sea ice structure and biological activity in the Antarctic Marginal Ice Zone. *Journal of Geophysical Research*, **89**(C2), 2087–2095.
- Cole, D. M. and L. H. Shapiro [1998] Observations of brine drainage networks and microstructure of first-year sea ice. *Journal of Geophysical Research*, **103**(C10), 21,739–21,750.
- Comiso, J. [1995] SSM/I Concentrations using the Bootstrap algorithm. *Technical Report RP 1380*, National Aeronautics and Space Administration, Goddard Space Flight Center, Greenbelt - MD.
- Connolly, J. P. and R. B. Coffin [1995] Model of carbon cycling in planktonic food webs. *Journal of Environmental Engineering*, **121**(10), 682–690.
- Cota, G. F., W. O. Smith Jr., D. M. Nelson, R. D. Muench and L. I. Gordon [1992] Nutrient and biogenic particulate distributions, primary productivity and nitrogen uptake in the Weddell-Scotia Sea marginal ice zone during winter. *Journal of Marine Research*, **50**, 155–181.
- Cota, G. F. and C. W. Sullivan [1990] Photoadaptation, growth and production of bottom ice algae in the Antarctic. *Journal of Phycology*, **26**, 399–411.
- Cox, G. F. N. and W. F. Weeks [1974] Salinity variations in sea ice. *Journal of Glaciology*, **13**(67), 109–120.
- Cox, G. F. N. and W. F. Weeks [1975] Brine drainage and initial salt entrapment in sodium chloride ice. *Technical Report 345*, US Army Corps of Engineers, Cold Regions Research and Engineering Laboratory.
- Cox, G. F. N. and W. F. Weeks [1983] Equations for determining the gas and brine volumes in sea-ice samples. *Journal of Glaciology*, **29**(102), 306–316.
- Cox, G. F. N. and W. F. Weeks [1986] Changes in the salinity and porosity of sea-ice samples during shipping and storage. *Journal of Glaciology*, **32**(112), 371–375.

- Cox, G. F. N. and W. F. Weeks [1988] Numerical simulations of the profile properties of undeformed first-year sea ice during the growth season. *Journal of Geophysical Research*, **93**(C10), 12,449–12,460.
- Cullen, J. J. and M. R. Lewis [1988] The kinetics of algal photoadaptation in the context of vertical mixing. *Journal of Plankton Research*, **10**(5), 1039–1063.
- Daly, K. L. [1998] Physioecology of juvenile Antarctic Krill (*Euphasia superba*) during spring in ice-covered seas. In: *Antarctic Sea Ice: Biological Processes, Interactions and Variability* (edited by Lizotte, M. P. and K. Arrigo), volume 73 of *Antarctic Research Series*, pp. 183–198. American Geophysical Union, Washington, D.C.
- Davidson, K. [1996] Modelling microbial food webs. *Marine Ecology Progress Series*, **145**(1-3), 279–296.
- Davidson, K., A. Cunningham and K. J. Flynn [1995] Predator-prey interactions between *Isochrysis galbana* and *Oxyrrhis marina*. 3. Mathematical modelling of predation and nutrient regeneration. *Journal of Plankton Research*, **17**(3), 465–492.
- Davidson, K. and W. S. C. Gurney [1999] An investigation of non-steady-state algal growth. II. Mathematical modelling of co-nutrient-limited algal growth. *Journal of Plankton Research*, **21**(5), 839–858.
- Davidson, K., G. Wood, E. H. John and K. J. Flynn [1999] An investigation of non-steady-state algal growth. I. An experimental model ecosystem. *Journal of Plankton Research*, **21**(5), 811–837.
- Dieckmann, G., M. A. Lange, S. F. Ackley and J. C. Jennings Jr. [1991a] The nutrient status in sea ice of the Weddell Sea during winter: effects of sea ice texture and algae. *Polar Biology*, **11**, 449–456.
- Dieckmann, G. S., H. Eicken, C. Haas, D. L. Garrison, M. Gleitz, M. Lange, E.-M. Nöthig, M. Spindler, C. W. Sullivan, D. N. Thomas and J. Weissenberger [1998] A compilation of data on sea ice algal standing crop from the Bellingshausen, Amundsen and Weddell seas from 1983 to 1994. In: *Antarctic Sea Ice: Biological Processes, Interactions and Variability* (edited by Lizotte, M. P. and K. Arrigo), volume 73 of *Antarctic Research Series*, pp. 85–92. American Geophysical Union, Washington, D.C.
- Dieckmann, G. S., M. Spindler, M. Lange, S. F. Ackley and H. Eicken [1991b] Antarctic sea ice: a habitat for the foraminifer *Neogloboquadrina pachyderma*. *Journal of Foraminiferal Research*, **21**(2), 182–189.
- Dijkman, N. [2001] *The regulation of photosynthesis in diatoms under dynamic irradiance*. Phd. thesis, Universität Bremen (Biologie/Chemie).
- Dower, K. M., M. I. Lucas, R. Philips, G. Dieckmann and D. H. Robinson [1996] Phytoplankton biomass, P-I relationships and primary production in the Weddell Sea, Antarctica, during the austral autumn. *Polar Biology*, **16**, 41–52.

- Drinkwater, M. and C. Haas [1994] Snow, sea-ice, and radar observations during ANT X/4: Summary data report. *Berichte aus dem Fachbereich Physik 53*, Alfred-Wegener Institute (AWI), Bremerhaven, Germany.
- Droop, M. R. [1973] Some thoughts on nutrient limitation in algae. *Journal of Phycology*, **9**, 264–272.
- Ebert, E. E. and J. A. Curry [1993] An intermediate one-dimensional thermodynamic sea ice model for investigating ice-atmosphere interactions. *Journal of Geophysical Research*, **98**(C6), 10,085–10,109.
- Ebert, E. E., J. L. Schramm and J. A. Curry [1995] Disposition of solar radiation in sea ice and the upper ocean. *Journal of Geophysical Research*, **100**(C8), 15,965–15,975.
- Eicken, H. [1992] Salinity profiles of Antarctic sea ice: field data and model results. *Journal of Geophysical Research*, **97**(C10), 15,545–15,557.
- Eicken, H. [1998] Deriving modes and rates of ice growth in the Weddell Sea from microstructural, salinity and stable-isotope data. In: *Antarctic Sea Ice: Physical processes, interactions and variability* (edited by Jeffries, M. O.), volume 74 of *Antarctic Research Series*, pp. 89–122. American Geophysical Union, Washington, D.C.
- El-Sayed, S. Z. [1967] On the productivity of the south-west Atlantic Ocean and the waters west of the Antarctic Peninsula. *Antarctic Research Series*, **11**, 15–47.
- Eppley, R. W. [1972] Temperature and phytoplankton growth in the sea. *Fishery Bulletin*, **70**(4), 1063–1085.
- Fasham, M. J. R., H. W. Ducklow and S. M. McKelvie [1990] A nitrogen-based model of plankton dynamics in the oceanic mixed layer. *Journal of Marine Research*, **48**(3), 591–639.
- Fiala, M. and L. Oriol [1990] Light-temperature interactions on the growth of Antarctic diatoms. *Polar Biology*, **10**, 629–636.
- Fichefet, T. and M. A. Morales Maqueda [1999] Modelling the influence of snow accumulation and snow-ice formation on the seasonal cycle of the Antarctic sea-ice cover. *Climate Dynamics*, **15**, 251–268.
- Flynn, K. J. [1990] Determination of nitrogen status in microalgae. *Marine Ecology Progress Series*, **61**, 291–307.
- Flynn, K. J. and K. Davidson [1993] Predator-prey interactions between *Isochrysis galbana* and *Oxyrrhis marina*. 2. Release of non-protein amines and faeces during predation of *Isochrysis*. *Journal of Plankton Research*, **15**(8), 893–905.
- Flynn, K. J., K. Davidson and J. W. Leftley [1994] Carbon-nitrogen relations at whole-cell and free-amino-acid levels during batch growth of *Isochrysis galbana* (Prymnesiophyceae) under conditions of alternating light and dark. *Marine Biology*, **118**(2), 229–237.

- Fritsen, C. H., S. F. Ackley, J. N. Kremer and C. W. Sullivan [1998] Flood-Freeze Cycles and Microalgal Dynamics in Antarctic Pack ice. In: *Antarctic Sea Ice: Biological Processes, Interactions and Variability* (edited by Lizotte, M. P. and K. Arrigo), volume 73 of *Antarctic Research Series*, pp. 1–21. American Geophysical Union, Washington, D.C.
- Fritsen, C. H., V. I. Lytle, S. F. Ackley and C. W. Sullivan [1994] Autumn bloom of Antarctic Pack-ice algae. *Science*, **266**, 782–784.
- Garrison, D. L. [1991] Antarctic Sea Ice Biota. *American Zoologist*, **31**, 17–33.
- Garrison, D. L., S. F. Ackley and K. R. Buck [1983] A physical mechanism for establishing algal populations in frazil ice. *Nature*, **306**, 363–365.
- Garrison, D. L. and K. R. Buck [1989] Protozooplankton in the Weddell Sea, Antarctica: abundance and distribution in the ice-edge zone. *Polar Biology*, **9**, 341–351.
- Garrison, D. L. and K. R. Buck [1991] Surface-layer sea ice assemblages in Antarctic pack ice during the austral spring: environmental conditions, primary production and community structure. *Marine Ecology Progress Series*, **75**, 161–172.
- Garrison, D. L., K. R. Buck and G. A. Fryxell [1987] Algal assemblages in Antarctic pack ice and in ice-edge plankton. *Journal of Phycology*, **23**, 564–572.
- Garrison, D. L. and A. R. Close [1993] Winter ecology of the sea ice biota in Weddell Sea pack ice. *Marine Ecology Progress Series*, **96**, 17–31.
- Garrison, D. L., A. R. Close and E. Reimnitz [1989] Algae concentrated by frazil ice: evidence from laboratory experiments and field measurements. *Antarctic Science*, **1**(4), 313–316.
- Garwood Jr., R. W., R. R. Harcourt and R. E. Stone [1998] Simulation of Drifters in a Turbulent Ocean. In: *Naval Research Reviews* (edited by Davidson, K. L.), volume L, pp. 9–14. Dept. of Oceanography, Naval Postgraduate School, Monterey, CA.
- Gathman, S. G. [1983] Optical properties of the marine aerosol as predicted by the Navy aerosol model. *Optical Engineering*, **22**, 57–62.
- Geider, R. J. [1993] Quantitative phytoplankton ecophysiology: implications for primary production and phytoplankton growth. *ICES Mar. Sci. Symp.*, **197**, 52–62.
- Geider, R. J., H. L. MacIntyre and T. M. Kana [1996] A dynamic model of photoadaptation in phytoplankton. *Limnology and Oceanography*, **41**(1), 1–15.
- Geider, R. J., H. L. MacIntyre and T. M. Kana [1997] Dynamic model of phytoplankton growth and acclimation: Responses of the balanced growth rate and the chlorophyll a: Carbon ratio to light, nutrient-limitation and temperature. *Marine Ecology Progress Series*, **148**(1-3), 187–200.
- Geider, R. J., H. L. MacIntyre and T. M. Kana [1998] A dynamic regulatory model of phytoplanktonic acclimation to light, nutrients, and temperature. *Limnology and Oceanography*, **43**(4), 679–694.

- Geider, R. J. and T. Platt [1986] A mechanistic model of photoadaptation in microalgae. *Marine Ecology Progress Series*, **30**(1), 85–92.
- Gleitz, M., A. Bartsch, G. Dieckmann and H. Eicken [1998] Composition and succession of sea ice diatom assemblages in the eastern and southern Weddell Sea, Antarctica. In: *Antarctic Sea Ice: Biological Processes, Interactions and Variability* (edited by Lizotte, M. P. and K. Arrigo), volume 73 of *Antarctic Research Series*, pp. 107–120. American Geophysical Union, Washington, D.C.
- Gleitz, M., H. Kukert, U. Riebesell and G. S. Dieckmann [1996] Carbon acquisition and growth of Antarctic sea ice diatoms in closed bottle incubations. *Marine Ecology Progress Series*, **135**, 169–177.
- Gleitz, M. and D. N. Thomas [1993] Variation in phytoplankton standing stock, chemical composition and physiology during sea-ice formation in the southeastern Weddell Sea, Antarctica. *Journal of Experimental Marine Biology and Ecology*, **173**, 211–230.
- Gleitz, M., M. R. v.d.Loeff, D. N. Thomas, G. S. Dieckmann and F. J. Millero [1995] Comparison of summer and winter inorganic carbon, oxygen and nutrient concentrations in Antarctic sea ice brine. *Marine Chemistry*, **51**, 81–91.
- Goldman, J. and M. Dennett [1990] Dynamics of prey selection by and omnivorous flagellate. *Marine Ecology Progress Series*, **59**, 183–194.
- Gosselin, M., M. Levasseur, P. A. Wheeler, R. A. Horner and B. C. Booth [1997] New measurements of phytoplankton and ice algal production in the Arctic Ocean. *Deep-Sea Research II*, **44**, 1623–1644.
- Gow, A. J., S. F. Ackley, W. F. Weeks and J. W. Govoni [1982] Physical and structural characteristics of Antarctic sea ice. *Annals of Glaciology*, **3**, 113–117.
- Grasshoff, K., M. Ehrhard and K. Kremmling [1983] *Methods of seawater analysis*. Verlag Chemie, Weinheim, 2nd edition.
- Gregg, W. W. and K. L. Carder [1990] A simple spectral solar irradiance model for cloudless maritime atmospheres. *Limnology and Oceanography*, **35**(8), 1657–1675.
- Grenfell, T. C. [1983] A theoretical model of the optical properties of sea ice in the visible and near infrared. *Journal of Geophysical Research*, **88**(C14), 9723–9735.
- Grossi, S. M., S. T. Kottmeier, R. L. Moe, G. T. Taylor and C. W. Sullivan [1987] Sea ice microbial communities. VI. Growth and primary production in bottom ice under graded snow cover. *Marine Ecology Progress Series*, **35**, 153–164.
- Grossmann, S. and G. S. Dieckmann [1994] Bacterial standing stock, activity, and carbon production during formation and growth of sea ice in the Weddell Sea, Antarctica. *Applied and Environmental Microbiology*, **60**(8), 2746–2753.
- Günther, S. and G. Dieckmann [1999] Seasonal development of algal biomass in snow-covered fast ice and the underlying platelet layer in the Weddell Sea, Antarctica. *Antarctic Science*, **11**(3), 305–315.

- Gutfraind, R. and S. B. Savage [1997] Marginal ice zone rheology: comparison of results from continuum-plastic models and discrete-particle simulations. *Journal of Geophysical Research*, **102**(C6).
- Herber, A., L. W. Thomason, V. F. Radionov and U. Leiterer [1993] Comparison of trends in the tropospheric and stratospheric aerosol optical depths in the Antarctic. *Journal of Geophysical Research*, **98**(D10), 18,441–18,447.
- Hibler III, W. D. and S. F. Ackley [1983] Numerical simulation of the Weddell Sea pack ice. *Journal of Geophysical Research*, **88**, 2873–2887.
- Horner, R. A., E. E. Syvertsen, T. D. P. and C. Lange [1988] Proposed terminology and reporting units for sea ice algal assemblages. *Polar Biology*, **8**, 249–253.
- Iqbal, M. [1983] *An Introduction to Solar Radiation*. Academic Press, Ontario, Canada.
- Irwin, B. D. [1990] Primary production of ice algae on a seasonally-ice-covered, continental shelf. *Polar Biology*, **10**, 247–254.
- Jacques, G. [1983] Some ecophysiological aspects of the Antarctic phytoplankton. *Polar Biology*, **2**, 27–33.
- Jeffries, M. O., W. F. Weeks, R. Shaw and K. Morris [1993] Structural characteristics of congelation and platelet ice and their role in the development of Antarctic land-fast sea ice. *Journal of Glaciology*, **39**(132), 223–238.
- JGOFS [1998] Report of the Southern Ocean Regional Synthesis Workshop. *Technical report*, Joint Global Ocean Flux Study, Bremerhaven, Germany.
- Johnsen, G. and E. N. Hegseth [1991] Photoadaptation of sea-ice microalgae in the Barents sea. *Polar Biology*, **11**, 179–184.
- Kasten, F. [1966] A new table and approximate formula for relative optical air mass. *Arch. Meteorol. Geophys. Bioklimatol.*, **B14**, 206–223.
- Kirk, J. T. O. [1981] Estimation of the scattering coefficient of natural waters using underwater irradiance measurements. *Aust. J. Mar. Freshwater Res.*, **32**, 533–539.
- Kirk, J. T. O. [1994] Characteristics of the light field in highly turbid waters: A Monte Carlo study. *Limnology and Oceanography*, **39**(3), 702–706.
- Klaas, C. [1996] *Verteilung und Einfluss von herbivoren Protozoen auf Phytoplanktonbestände und Vertikalflüsse Im Suedpolarmeer*. Phd. thesis, Universität Bremen (Biologie/Chemie).
- Kottmeier, C., S. Ackley, E. Andreas, D. Crane, H. Hoerber, J. King, J. Lauiniainen, D. Limbert, D. Martinson, R. Roth, L. Sellmann, P. Wadhams and T. Vihma [1997] Wind, temperature and ice motion statistics in the Weddell Sea (A compilation based on data from drifting buoys, vessels, and operational weather analysis). *Technical Report WMO/TD N. 797*, World Climate Research Programme, International Programme for Antarctic Buoys.

- Kottmeier, S. T. and C. W. Sullivan [1987] Late winter primary production and bacterial production in sea ice and seawater west of the Antarctic Peninsula. *Marine Ecology Progress Series*, **36**, 287–298.
- Kottmeier, S. T. and C. W. Sullivan [1990] Bacterial biomass and production in pack ice of Antarctic marginal ice edge zones. *Deep-Sea Research*, **37**(8), 1311–1330.
- Krembs, C. and A. Engel [2001] Abundance and variability of microorganisms and TEP across the ice-water interface of melting first-year sea-ice in the Laptev Sea (Arctic). *Marine Biology*, **138**, 173–185.
- Krembs, C., R. Gradinger and M. Spindler [2000] Implications of brine channel geometry and surface area for the interaction of sympagic organisms in Arctic sea ice. *Journal of Experimental Marine Biology and Ecology*, **243**(1), 55–80.
- Kristiansen, S., E. E. Syvertsen and T. Farbot [1992] Nitrogen uptake in the Weddell Sea during late winter and spring. *Polar Biology*, **12**, 245–251.
- Laevastu, T. [1960] Factors affecting the temperature of the surface layer of the sea. *Commentat. Phys. Math.*, **25**, 1–36.
- Lancelot, C., G. Billen, S. Becquevort, S. Mathot and C. Veth [1991a] Modelling carbon cycling through phytoplankton and microbes in the Scotia-Weddell Sea area during sea ice retreat. *Marine Chemistry*, **35**, 305–324.
- Lancelot, C., C. Veth and S. Mathot [1991b] Modelling ice-edge phytoplankton bloom in the Scotia-Weddell Sea sector of the Southern Ocean during spring 1988. *Journal of Marine Systems*, **2**(3-4), 333–346.
- Lange, M. A., S. F. Ackley, P. Wadhams, G. S. Dieckmann and H. Eicken [1989] Development of sea ice in the Weddell Sea, Antarctica. *Annals of Glaciology*, **12**, 92–96.
- Laurion, I., S. Demmers and A. F. Vézina [1995] The microbial food web associated with the ice algal assemblage: biomass and bacterivory of nanoflagellate protozoans in Resolute Passage (High Canadian Arctic). *Marine Ecology Progress Series*, **120**, 77–87.
- Legendre, L., S. F. Ackley, B. Dieckmann, G. S. and Gulliksen, R. Horner, T. Hoshiai, I. A. Melnikov, W. S. Reeburgh, M. Spindler and C. W. Sullivan [1992] Ecology of sea ice biota. 2. Global significance. *Polar Biology*, **12**(3-4), 429–444.
- Lemke, P. [1994] Die Expedition Antarktis X/4 mit FS Polarsternin 1992. *Berichte zur Polarforschung*, **140**.
- Lemke, P., W. B. Owens and W. D. Hibler III [1990] A coupled sea ice - mixed layer - pycnocline model for the Weddell Sea. *Journal of Geophysical Research*, **95**(C6), 9513–9525.
- Leppäranta, M. and T. Manninen [1988] The Brine and gas content of sea ice with attention to low salinities and high temperatures. *Technical Report 2*, Finnish Institute of Marine Research.

- Light, B. [1995] *A structural-optical model of cold sea ice*. Master of science thesis, University of Washington.
- Light, B., H. Eicken, G. A. Maykut and T. C. Grenfell [1998] The effect of included particles on the spectral albedo of sea ice. *Journal of Geophysical Research*, **103**(C12), 27,739–27,752.
- Liou, K.-N., K. P. Freeman and T. Sasamori [1978] Cloud and aerosol effects on the solar heating rate of the atmosphere. *Tellus*, **30**, 62–70.
- Lizotte, M. P. [2001] The contributions of sea ice algae to Antarctic marine primary production. *American Zoologist*, **41**, 57–73.
- Lizotte, M. P. and C. W. Sullivan [1991] Photosynthesis-irradiance relationships in microalgae associated with Antarctic pack ice: Evidence for in situ activity. *Marine Ecology Progress Series*, **71**(2), 175–184.
- Lizotte, M. P. and C. W. Sullivan [1992] Photosynthetic capacity in microalgae associated with Antarctic pack ice. *Polar Biology*, **12**, 497–502.
- Lytle, V. I. and S. F. Ackley [1996] Heat flux through sea ice in the western Weddell Sea: convective and conductive transfer processes. *Journal of Geophysical Research*, **101**(C4), 8853–8868.
- MacIntyre, H. L., T. M. Kana and R. J. Geider [2000] The effect of water motion on short-term rates of photosynthesis by marine phytoplankton. *Trends in Plant Science*, **5**(1), 12–17.
- Mackintosh, N. A. and H. F. P. Herdman [1940] Distribution of the pack-ice in the Southern Ocean. *Discovery Reports*, **19**, 285–296.
- Makshtas, A. P., E. L. Andreas, P. V. Svyashchennikov and V. F. Timachev [1998] Accounting for clouds in sea ice models. *CRREL Report 98-9*, US Army Corps of Engineers, Cold Regions Research and Engineering Laboratory.
- Markus, T. and D. J. Cavalieri [1998] Snow depth distributions over sea ice in the Southern Ocean from satellite passive microwave data. In: *Antarctic Sea Ice. Physical Processes, Interactions and Variability* (edited by Jeffries, M. O.), volume 74 of *Antarctic Research Series*, pp. 19–39. American Geophysical Union, Washington, D.C.
- Martinson, D. [1994] Ocean heat and sea ice thickness in the Southern Ocean. In: *Ice in the Climate System* (edited by Peltier, W.), pp. 597–610. Springer-Verlag, New York.
- Mathot, S., S. Becquevort and C. Lancelot [1991] Microbial communities from the sea ice and adjacent water column at the time of ice melting in the northwestern part of the Weddell Sea. In: *Proceedings of the Pro-Mare Symposium on Polar Marine Ecology* (edited by Sakshaug, E., C. C. E. Hopkins and N. A. Oeritsland), volume 10(1-2), pp. 267–275. Oslo Lufthavn Norway Norsk-Polarinst.

- Matsuda, O., S. Ishikawa and K. Kawaguchi [1990] Seasonal Variation of Particulate Organic Matter under the Antarctic Fast Ice and its importance to Benthic Life. In: *Antarctic Ecosystems. Ecological Change and Conservation* (edited by Kerry, K. R. and G. Hempel), pp. 143–148. Springer-Verlag, Berlin - Heidelberg.
- Maykut, G. A. and N. Untersteiner [1971] Some results from a time-dependent thermodynamic model of sea ice. *Journal of Geophysical Research*, **76**(6), 1550–1575.
- McMinn, A. and C. Ashworth [1998] The use of oxygen microelectrodes to determine the net production by an Antarctic sea ice algal community. *Antarctic Science*, **10**(1), 38–44.
- McPhee, M. G., C. Kottmeier and J. H. Morison [1999] Ocean heat flux in the central Weddell Sea during winter. *Journal of Physical Oceanography*, **29**, 1166–1179.
- Melnikov, I. [1995] An *in situ* experimental study of young sea ice formation on an Antarctic lead. *Journal of Geophysical Research*, **100**(C3), 4673–4680.
- Mengesha, S., F. Dehairs, M. Fiala, M. Elskens and L. Goeyens [1998] Seasonal variation of phytoplankton community structure and nitrogen uptake regime in the Indian Sector of the Southern Ocean. *Polar Biology*, **20**(4), 259–272.
- Mills, E. L. [1989] *Biological Oceanography. An early history, 1870-1960*. Cornell University Press.
- Mock, T. and R. Gradinger [1999] Determination of Arctic ice algal production with a new *in situ* incubation technique. *Marine Ecology Progress Series*, **177**, 15–26.
- Mock, T. and R. Gradinger [2000] Changes in photosynthetic carbon allocation in algal assemblages of Arctic sea ice with decreasing nutrient concentrations and irradiance. *Marine Ecology Progress Series*, **202**, 1–11.
- Moloney, C. L. and J. G. Field [1989] General allometric equations for rates of nutrient uptake, ingestion, and respiration in plankton organisms. *Limnology and Oceanography*, **34**(7), 1290–1299.
- Morel, A. [1978] Available, usable, and stored radiant energy in relation to marine photosynthesis. *Deep-Sea Research*, **25**, 673–688.
- Nelder, J. A. and R. Mead [1965] A simplex method for function minimization. *Computer Journal*, **7**, 308–313.
- Nelson, D. M. and L. I. Gordon [1982] Production and pelagic dissolution of biogenic silica in the Southern Ocean. *Geochimica et Cosmochimica Acta*, **46**, 491–501.
- Nelson, D. M., W. O. Smith Jr., L. I. Gordon and B. A. Huber [1987] Spring distributions of density, nutrients and phytoplankton biomass in the ice-edge zone of the Weddell-Scotia Sea. *Journal of Geophysical Research*, **92**, 7181–7190.
- Nelson, D. M., W. O. Smith Jr., R. D. Muench, L. I. Gordon, C. W. Sullivan and D. M. Husby [1989] Particulate matter and nutrient distributions in the ice-edge zone of the Weddell Sea: relationship to hydrography during late summer. *Deep-Sea Research*, **36**(2), 191–209.

- Nelson, D. M. and P. Tréguer [1992] Role of silicon as a limiting nutrient to Antarctic diatoms: evidence from kinetic studies in the Ross Sea ice-edge zone. *Marine Ecology Progress Series*, **80**, 255–264.
- Neori, A. and O. Holm Hansen [1982] Effect of temperature on rate of photosynthesis in Antarctic phytoplankton. *Polar Biology*, **1**(1), 33–38.
- Olbers, D., V. Gouretski, G. Seiss and J. Schröter [1992] *Hydrographic Atlas of the Southern Ocean*. Alfred Wegener Institute, Bremerhaven. (also available on-line at <http://www.awi-bremerhaven.de/Atlas/SO/Deckblatt.html>).
- Paasche, E. [1973] Silicon and the ecology of marine plankton diatoms. I. *Thalassiosira pseudonana* (*Cyclotella nana*) growth in a chemostat with silicate as the limiting nutrient. *Marine Biology*, **119**, 117–126.
- Palmisano, A. C., J. B. SooHoo, S. L. SooHoo, S. T. Kottmeier, L. L. Craft and C. W. Sullivan [1986] Photoadaptation in *Phaeocystis pouchetti* advected beneath annual sea ice in McMurdo Sound, Antarctica. *Journal of Plankton Research*, **8**(5), 891–906.
- Palmisano, A. C., J. B. SooHoo and C. W. Sullivan [1985] Photosynthesis-irradiance relationships in sea ice microalgae from McMurdo Sound, Antarctica. *Journal of Phycology*, **21**, 341–346.
- Paltridge, G. W. and C. M. R. Platt [1976] *Radiative Process in Meteorology and Climatology*, volume 5 of *Developments in Atmospheric Science*. Elsevier, Amsterdam, The Netherlands.
- Parkinson, C. L. and W. M. Washington [1979] A large-scale numerical model of sea ice. *Journal of Geophysical Research*, **84**(C1), 311–337.
- Pasternak, A. F. [1995] Gut contents and diel feeding rhythm in dominant copepods in the ice-covered Weddell Sea, March 1992. *Polar Biology*, **15**, 583–586.
- Perovich, D. K. [1990] Theoretical estimates of light reflection and transmission by spatially complex and temporally varying sea ice covers. *Journal of Geophysical Research*, **95**(C6), 9557–9567.
- Perovich, D. K. and A. J. Gow [1991] A statistical description of the microstructure of young sea ice. *Journal of Geophysical Research*, **C9**(96), 16,943–16,953.
- Platt, T. and A. D. Jassby [1976] The relationship between photosynthesis and light for natural assemblages of coastal marine phytoplankton. *Journal of Phycology*, **12**, 421–430.
- Press, W. H., S. A. Teukolsky, W. T. Vetterling and B. P. Flannery [1992] *Numerical Recipes in FORTRAN. The Art of Scientific Computing*. Cambridge University Press, second edition.
- Priscu, J. C., M. P. Lizotte, G. L. Cota, A. C. Palmisano and C. W. Sullivan [1991] Comparison of the irradiance response of photosynthesis and nitrogen uptake by sea ice microalgae. *Marine ecology Progress Series*, **70**, 201–210.

- Richardson, C. [1976] Phase relationships in sea ice as a function of temperature. *Journal of Glaciology*, **17**(77), 507–519.
- Riebesell, U., I. Schloss and V. Smetacek [1991] Aggregation of algae released from melting sea ice: implications for seeding and sedimentation. *Polar Biology*, **11**, 239–248.
- Rivkin, R. B. and M. Putt [1987] Photosynthesis and cell division by Antarctic microalgae: comparison of benthic, planktonic and ice algae. *Journal of Phycology*, **23**, 223–229.
- Robinson, D. H., K. R. Arrigo, R. Iturriaga and C. W. Sullivan [1995] Microalgal light-harvesting in extreme low-light environments in McMurdo Sound, Antarctica. *Journal of Phycology*, **31**, 508–520.
- Schnack-Schiel, S. B., D. Thomas, H.-U. Dahms, C. Haas and E. Mizdalski [1998] Copepods in Antarctic sea ice. In: *Antarctic Sea Ice: Biological Processes, Interactions and Variability* (edited by Lizotte, M. P. and K. Arrigo), volume 73 of *Antarctic Research Series*, pp. 173–182. American Geophysical Union, Washington, D.C.
- Schwerdtfeger, W. [1963] The thermal properties of sea ice. *Journal of Glaciology*, **4**, 789–807.
- Sherr, B., E. Sherr and P. Wheeler [1998] Seasonal production and respiration in the Central Arctic Ocean: results from the SHEBA/JOIS biology program. In: *Abstracts EOS*, volume 79(45), p. F400. AGU Fall Meeting, San Francisco, CA.
- Smith, D. C. and J. H. Morison [1993] A numerical study of haline convection beneath leads in sea ice. *Journal of Geophysical Research*, **98**(C6), 10,069–10,083.
- Smith, R. C. and K. S. Baker [1981] Optical properties of the clearest natural waters (200–800 nm). *Applied Optics*, **20**(2), 177–184.
- Smith, R. C., K. S. Baker, H. M. Dierssen, S. E. Stammerjohn and M. Vernet [2001] Variability of primary production in an Antarctic marine ecosystem as estimated using a multi-scale sampling strategy. *American Zoologist*, **41**, 40–56.
- Smith, R. E. H., W. G. Harrison, L. R. Harris and A. W. Herman [1990] Vertical fine structure of particulate matter and nutrients in sea ice of the High Arctic. *Canadian Journal of Fisheries and Aquatic Sciences*, **47**(7), 1348–1355.
- Smith Jr., W. O. and D. M. Nelson [1991] Phytoplankton growth and new production in the Weddell Sea marginal ice zone in the austral spring and autumn. *Limnology and Oceanography*, **35**(4), 809–821.
- Sommer, U. [1991] Comparative nutrient status and competitive interactions of two Antarctic diatoms (*Corethron criophilum* and *Thalassiosira antarctica*). *Journal of Plankton Research*, **13**(1), 61–75.
- Spencer, J. W. [1971] Fourier series representation of the position of the sun. *Search*, **2**(5), 172–172.
- Spindler, M. and G. S. Dieckmann [1994] Ecological Significance of the Sea Ice Biota. In: *Antarctic Science, Global Concerns* (edited by Hempel, G.), pp. 60–68. Springer-Verlag.

- Stoer, J. and R. Burlisch [1979] *Introduction to Numerical Analysis*. Springer-Verlag, New York.
- Sturm, M., K. Morris and R. A. Massom [1998] The winter snow cover of the west Antarctic pack ice: its spatial and temporal variability. In: *Antarctic Sea Ice. Physical Processes, Interactions and Variability* (edited by Jeffries, M. O.), volume 74 of *Antarctic Research Series*, pp. 1–18. American Geophysical Union, Washington, D.C.
- Sullivan, C., C. H. Fritsen and C. W. Mordy [1992] Microbial production in the Antarctic pack ice: time-series studies at the U.S.-Russian drifting ice station. *Antarctic Journal of the United States*, **Review 1992**, 113–115.
- Sullivan, C. W. [1979] Diatom mineralization of silicic acid IV. Kinetics of soluble Si pool formation in exponentially growing and synchronized *Navicula pelliculosa*. *Journal of Phycology*, **15**, 210–216.
- Sullivan, C. W., K. R. Arrigo, C. R. McClain, J. C. Comiso and J. Firestone [1993] Distributions of phytoplankton blooms in the Southern Ocean. *Science*, **262**(5141), 1832–1837.
- Suzuki, Y., S. Kudoh and M. Takahashi [1997] Photosynthetic and respiratory characteristics of an Arctic ice algal community living in low light and low temperature. *Journal of Marine Systems*, **11**, 111–121.
- Syrret, P. J., K. J. Flynn, C. J. Molloy, G. K. Dixon, A. M. Peplinska and R. C. Cresswell [1986] Effects of nitrogen deprivation on rates of uptake of nitrogenous compounds by the diatom, *Phaeodactylum tricornutum* Bohlin. *New Phytol.*, **102**, 39–44.
- Tanre, D., M. Herman, P. Y. Deschamps and A. de Lefte [1979] Atmospheric modeling for space measurements of ground reflectances, including bidirectional properties. *Applied Optics*, **18**, 3587–3594.
- Thingstad, T. F. and E. Sakshaug [1990] Control of phytoplankton growth in nutrient recycling ecosystems. Theory and terminology. *Marine Ecology Progress Series*, **63**, 261–272.
- Thomas, D. N., M. E. M. Baumann and M. Gleitz [1992] Efficiency of carbon assimilation and photoacclimation in a small unicellular *Chaetoceros* species from the Weddell Sea (Antarctica): influence of temperature and irradiance. *Journal of Experimental Marine Biology and Ecology*, **157**, 195–209.
- Tilzer, M. M., M. Elbraechter, W. W. Gieskes and B. Beese [1986] Light-temperature interactions in the control of photosynthesis in Antarctic phytoplankton. *Polar Biology*, **5**(2), 105–111.
- Tilzer, M. M., B. von Bodungen and V. Smetacek [1985] Light-dependence of phytoplankton photosynthesis in the Antarctic Ocean: implications for regulating productivity. In: *Antarctic Nutrient Cycles and Food Webs* (edited by Siegfried, W. R., P. R. Condy and R. M. Laws), pp. 60–69. Springer-Verlag, Berlin Heidelberg.
- Timmermann, R., A. Beckmann and H. H. Hellmer [2001] Simulation of ice-ocean dynamics in the Weddell Sea. Part I: Model description and validation. *Journal of Geophysical Research*. In press.

- Tréguer, P. [1994] Antarctic Science, Global Concerns. In: *The Southern Ocean: Biogeochemical Cycles and Climate Changes* (edited by Hempel, G.), pp. 110–125. Springer-Verlag.
- Wadhams, P. [2000] *Ice in the ocean*. Gordon and Breach Science Publishers.
- Warren, S. G. [1984] Optical constants of ice from the ultraviolet to the microwave. *Applied Optics*, **23**(8), 1206–1225.
- Weissenberger, J. and S. Grossmann [1998] Experimental formation of sea ice: Importance of water circulation and wave action for incorporation of phytoplankton and bacteria. *Polar Biology*, **20**(3), 178–188.
- White, W. B. and R. G. Peterson [1996] An Antarctic Circumpolar Wave in surface pressure, wind, temperature and sea ice extent. *Nature*, **380**, 699–702.
- Wiscombe, W. J. and S. G. Warren [1980] A model for the spectral albedo of snow. I: Pure Snow. *Journal of Atmospheric Sciences*, **37**, 2712–2733.
- Yen, Y.-C. [1969] Recent studies on snow properties. *Adv. Hydrosoci.*, **5**, 173–214.
- Yen, Y.-C. [1981] Review of thermal properties of snow, ice and sea ice. *CRREL Report 81-10*, US Army Corps of Engineers, Cold Regions Research and Engineering Laboratory.
- Zeebe, R. E., H. Eicken, D. H. Robinson, D. Wolf-Gladrow and G. S. Dieckmann [1996] Modeling the heating and melting of sea ice through light absorption by microalgae. *Journal of Geophysical Research*, **101**(C1), 1163–1181.
- Zwally, H. J., J. C. Comiso, C. L. Parkinson, W. J. Campbell, F. D. Carsey and P. Gloersen [1983] Antarctic Sea Ice, 1973-1976. *Report SP-459*, National Aeronautics and Space Administration.